ABSTRACT

CHANG, SUK TAI. New Electrokinetic Techniques for Material Manipulation on the Microscale. (Under the direction of Dr. Orlin D. Velev.)

We report the results of series of investigations how electrically induced forces and interfacial phenomena could be used to manipulate particles and fluids on the microscale. Particle microseparations in a droplet floating on a dielectrophoretic liquid-chip system were investigated. Particle-localized electroosmotic flow was used for designing autonomously moving microdevices and locally distributed micropumps/mixers. Microfluidics was adapted for enhancing mechanical properties of materials with embedded microchannel networks. Ionic current rectification in charged aqueous gels was used for constructing new types of "soft matter" diodes. Detailed analytical and numerical modeling was performed for each system. The results of this work can apply to new fields of microfluidics, self-propelling microdevices, and aqueous gel-based electronic components.

In the first part of this work we explored unusual phenomena of colloidal particle transport and separation inside microdroplets floating in fluorinated oil on electrically controlled chips. Microspheres suspended in a drying droplet on liquid-liquid chips were rapidly separated in the droplet's top region due to water evaporation. During the evaporation process, a surface tension gradient emerged as a result of a non-uniform temperature distribution within the droplet. This interfacial gradient generated a Marangoni flow inside the evaporating droplet. The suspended colloidal particles driven by the convective flow were collected at the top of the droplets by the hydrodynamic flux compensating for the evaporation. The flow pattern and temperature distribution within the evaporating droplet were simulated using finite element calculation. The internal flow pattern calculated by the simulation was consistent with the experiments using tracer particles. The levitated microdroplets were used as templates for colloidal assembly and containers for microbioassays based on particle agglutination inside droplets.

An alternative mechanism of self-propulsion based on electroosmotic force and the extension of this propulsion force to innovative microfluidic pumps/mixers were developed

in the second part of this study. Various types of miniature diodes floating in water acted as self-propelling particles when powered by an alternating (AC) electric field. Direct (DC) electric field induced across the diodes as a result of rectification of the external AC field led to particle-localized electroosmotic flow. The resulting reactive force pushed the diodes in the direction opposite to the electroosmotic flux. The microelements began to move parallel to the electric field in the direction of either the cathode or the anode, depending on their surface charge. In effect, the semiconductor microelements harvest electric energy from external AC field and convert it into mechanical propulsion on the microscale. The particle-localized propulsion force was used in diode-actuated electroosmotic motors and actuators. Diodes embedded in microfluidic channel walls could serve as locally distributed pumps or mixers powered by a global AC external field. The experimental results were interpreted by numerical simulations of the electrohydrodynamic flows

The viscoelastic properties of fluids inside microchannels were used in the development of novel microfluidic materials in the form of flexible sheets that can be solidified on demand to yield preprogrammed shapes. These materials were based on microfluidic channel networks in polydimethylsiloxane (PDMS) filled with photocurable polymers. When the elastic sheets with embedded microchannel networks were shaped and exposed by UV light, the photoresist inside the channels was solidified and acted as endoskeleton within the PDMS layer, acquiring the pre-arranged shape. Bending and stretching moduli of the materials with solidified endoskeleton increased drastically and after the external force was removed, the memorized shapes were recovered. The permanent preservation of the shape of solidified microfluidic sheets could be used in making instant packages and supports on demand.

Finally, unidirectional ionic current flow across a fixed junction between two aqueous agarose gel phases containing oppositely charged polyelectrolytes was discovered. The non-linear current response of the interface between the cationic and anionic gels originated directly from anisotropy in the mobile charges within the system. The current densities in the forward bias and current rectifying ratios in the gel diodes were higher or comparable to those using ionic carries and junctions built from conductive polymers. The promising

feature of this new type of rectifying junction is that it is operates on the basis of water-borne ions. The devices are extremely simple, inexpensive and possess good long-term stability in DC or AC conduction mode.

New Electrokinetic Techniques for Material Manipulation on the Microscale

by
Suk Tai Chang

A dissertation submitted to the Graduate Faculty of
North Carolina State University
in partial fulfillment of the
requirements for the Degree of
Doctor of Philosophy

Chemical Engineering

Raleigh, North Carolina

2008

APPROVED BY:

_____	_____
Peter Kilpatrick	Saad Khan
_____	_____
Glenn Walker	Orlin Velev Chair of Advisory Committee

DEDICATION

this dissertation is dedicated to

my parents

and

my wife Juna,

my son Jinho (Kevin), my daughter Eunho (Emma),

who made all of this possible,

for their endless love, encouragement, support, and sacrifices

BIOGRAPHY

Suk Tai Chang was born on August 9, 1973 in Taebaek in Gangwon province in the eastern part of South Korea. The city of Taebaek is surrounded by Taebaek Mountains and is noted for its great natural beauty and largest coal mining industry in South Korea. When his age was eleven, he and his family moved to Seoul. The city of Seoul has been Korea's capital for the last 600 years, and now, is one of the world's largest cities with over ten million populations. Suk Tai graduated from Sung-Bo High School in 1992 and went on to a degree program in Chemical Engineering at the Chung-Ang University in Seoul with full scholarship. After receiving his Bachelor Degree in 1999, he continued his studies at the Gwangju Institute of Science and Technology for his Master Degree in whole cell biosensors. After graduation in 2001, he worked at the Hyosung Co. and the Korea Institute of Science and Technology as a researcher. In 2003 Fall, he joined the Department of Chemical and Biomolecular Engineering at North Carolina State University as a PhD student. Since then, he has been pursuing his graduate research under the guidance of Dr. Orlin D. Velev.

ACKNOWLEDGEMENTS

This work would not been possible without the support and encouragement of a great many individuals. Foremost, I would like to express my gratitude to my advisor Professor Orlin Velev, who has been an exceptional mentor and given me many insightful conversations in working hours or evening, even late night. His thoughtful advices and enthusiasm for science have always inspired me with a sense of right direction during my PhD studies and originality of thought, not just “So do I” in research. I can not thank him enough for his kind guidance, his work ethic, and his remarkable patience for my thesis work. Thanks so much Dr. Velev!!!

I would like to thank my parents for their unconditional love and support. They taught me the right way to live and no rewards without hard working by their own life. I must express my gratitude to my parent-in-laws for their endless love and helps for taking care of my babies in Raleigh. I thank my brothers, sisters, nephews, and nieces for their encouragement and cheerfulness throughout this journey.

I am very grateful to Professors Peter Kilpatrick, Saad Khan, and Glenn Walker for serving on my thesis committee and Professor Michael Dickey for his approval for a substitute on the committee. I am thankful to Professor Jan Genzer for his time and helps for the letter of recommendation. Professors Gregory Parsons and Mark Luo have allowed me to access their lab equipments many times during my experiments and I thank them for their helps. I also want to acknowledge Professors Vesselin Paunov in University of Hull, UK and Dimiter Petsev in University of New Mexico for many insightful discussions for my research. I should not forget to say thank to all the staff members from our department for their kindness and helps for the five years in NC State. Specially, I am thankful to the helps received from Shirley in installing FEMLAB software for my simulations.

There are many good memories shared with my fantastic colleagues in the Velev Research Family. I want to thank Dr. Ketan Bhatt and Dr. Brian Prevo for their assistance during my first year in the lab and their concerns about my future career. Thanks to Dr. Shalini Gupta for your smile and giggling that always made me happy in the school. How

can I forget my buddy Vinayak for lots of help, talks about life, and his encouragement. I should give thanks to Dr. Olivier Cayre, French peanut boy, for his fruitful collaboration on the gel diodes research and cheers in Spanish. Special thanks are to Dr. Sejong Kim for his discussions on my graduate research. I am also thankful to Sumit for sharing the daddy's life and his correction of my thesis writing. I like to express my thanks to Hyung-Jun, Burak, Garrett, and Robert for their hard work and collaboration on the gel work and the microfluidic project. I wish to thank everybody in our group, my classmate Lindsey, Dr. Daniel Kuncicky, Liz, Jairus, Jess, Dr. Stoyan Smoukov, and Hye-Young, with whom I have shared experiences in the group. I also owe a debt to Young Kuk and Yong-Jae from the first day in US, with whom I had fun opportunity and friendship. I appreciate Jeong-Seok Na for his understanding and helps for using his lab equipments. I am tempted to express thanks to Drs. Kie Jin Park, Changwoong Chu, Jaehoon Kim, and Chang Shin Park for their assistance and cheerfulness during my graduate study.

I can not finish without saying how grateful I am with my wife, Juna. I am truly thankful to you from the bottom of my heart for your love, your patience, your sacrifices, and our two little precious, Jinho & Eunho.

Table of Contents

LIST OF TABLES

LIST OF FIGURES

Chapter 1

General Introduction of Microfluidics

1.1. Introduction

Microfluidics is the science and technology of systems for controlling and manipulating small volumes of fluids through devices with at least one dimension in the micrometer range.[1,2] A large body of research in microfluidics has been performed in the multidisciplinary research areas of physical, chemical, and biological sciences. Microfluidics offers significant advantages, including a reduction in sample and reagent consumption, short times for analysis, performance with high sensitivity, low production cost, easy automation, and fabrication of portable and disposable devices.[2-6] The primary focus of my graduate research has been to develop and implement tools and techniques for manipulating fluids and colloidal particles using evaporation and electric field induced forces that can deliver additional functionalities in microfluidic systems. This chapter overviews the field of microfluidics and provides a brief review of recent developments in new types of microfluidics applications.

1.2. Brief Historical Overview of Microfluidics

The key technologies used in the development of microfluidic devices have originated from the fields of microfabrication and microelectromechanical systems (MEMS), where the use of photolithographical processes to scale down devices to the micrometer, or even smaller, features on a single chip was revolutionized.[3,6-8] Miniaturized devices handling fluids were initiated to enhance the analytical performance and dispense small amounts of liquids in chemical and materials processes. The first successful demonstration of a miniaturized analytical system of fluid transportation through microchannels was realized in 1977 as a gas chromatograph on a single silicon wafer, where a sample injection valve, a 1.5 m long separating capillary column, and a thermal conductivity detector were all integrated.[9] Ink jet printing nozzle arrays were developed by IBM researchers in the form of truncated pyramidal holes anisotropically etched in a silicon substrate and have had enormous industrial impact.[5,10-12] The concept of micro-total chemical analysis systems (μTAS) or lab-on-a-chip devices established by Manz *et al.* in 1990 led to explosive interest and developments of microfluidic systems as new research tools for chemical and biological applications.[13] This

μTAS included a single on-chip chemical sensing system incorporating all of analytical procedures (sample pretreatment, separation, and detection) into microfluidic system. A further boost in the microfluidics research was driven by support from the US Defense Advanced Research Projects Agency (DARPA) for developing field-deployable detectors for chemical biological warfare threats and the needs of new microanalytical methods in the field of molecular biology, such as high-throughput DNA or protein analysis.[6,14-16]

Earlier work in microfluidic devices was mostly performed in silicon and glass substrates. Microfluidic components (pumps,[17,18] valves,[19,20] mixers[21]) were fabricated in these rigid materials for chip-based analysis, such as phosphate sensing[22] and fast separation of amino acids and dyes by capillary electrophoresis.[23-25] Many more materials, notably plastics, are now being used. One particular polymer that has been used extensively is poly(dimethylsiloxane), or PDMS, where the microfluidic structures are fabricated by using rapid prototyping or soft lithography.[1,6,15,26-29] This elastomeric polymer offers potential advantages over the silicon of optically transparent surface, faster fabrication time, flexibility, and permeability to gases required for experiments with living mammalian cells.[4,6,30,31]

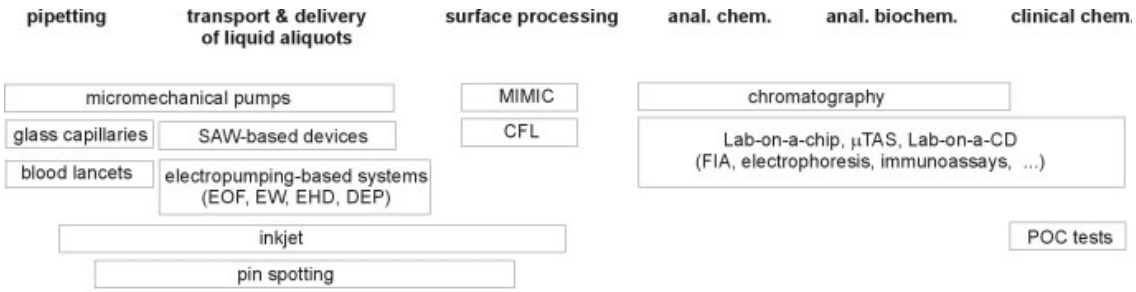

Figure 1.1. A wide range of applications in microfluidics utilizing many principles to transport and analyze small volumes of liquid.[29] SAW refers to surface acoustic wave, EOF to electroosmotic flow, EW to electrowetting, EHD to electrohydrodynamics, DEP to dielectrophoretic pumping, MIMIC to micromolding in capillaries, CFL to capillary force lithography, FIA to flow-injection assays, and POC to point-of care.

In present years, microfluidics has attracted an enormous interest by researchers from many disciplines other than analytical chemistry. Though the microfluidics technology is still

in its infancy, impressive progress has been made in the development of innovative experimental tools replacing macroscale conventional methods. Numerous applications of the microfluidics, taking advantage of various phenomena in microfluidic devices are shown in Figure 1.1.[29] Microfluidic research on the topics of micro pumps/mixers,[5,32-35] separation processes,[36] biological assays,[29,30,37,38] protein crystallization,[39] proteomic and genomic analysis,[15,40,41] clinical and forensic applications,[14,16,42,43] drug discovery,[44-46] and material synthesis[3,47-49] has been recently reported. During the design of the microfluidic devices in the above practical applications, a major challenge is the investigation of transport processes of fluids, colloidal particles, and biomolecules through microchannels. Since Manz *et al.* published their seminal work of miniaturized chemical analysis systems using electroosmotic pumping and electrophoretic separations,[25,50] electrokinetic forces have been widely used in the development of lab-on-a-chip devices. The next section includes a brief overview of the electrically induced forces for manipulating particles and microflows.

1.3. Electrokinetic Phenomena for Manipulating Microflows

New designs for driving fluid motion are needed in microfluidic devices using physical phenomena that are usually neglected in the macroscale. As the dimensions of channels decrease to microns, the importance of interfacial phenomena increases due to large surface-to-volume ratio.[1,2,4,51] Fluid manipulation in the microfluidic devices is greatly dominated by surface tension, capillary effects, electrokinetic effects, and viscous force rather than inertial force.[1,2,5] The flow in microchannels is laminar due to the low Reynolds number, making molecular diffusion essential to microfluidic mixing.[5,34,35,52] The motion of fluids and particle suspensions at this small-scale are driven by pressure gradients,[53,54] capillary pressure differences,[55-58] or surface tension gradients,[59-61] as summarized in Table 1.1.

The application of electrically induced forces to control and manipulate fluids, colloidal particles or biomolecules in lab-on-a-chip devices provides a powerful and convenient tools.[34,62-64] The use of electric fields in on-chip devices is especially effective in micron-sized systems through fabrication of small electrode structures that can generate high electrical fields at relatively small applied potentials.[63,65] Another advantage of the

microfluidic devices based on the electrokinetic phenomena is the relative simplicity of operation, with no requirement for external mechanical moving parts.[34,64,66] This advantage of electrokinetic forces allows fabrication of portable microfluidic devices.

Electrokinetic forces are acting on fluids and particles suspended in the fluids and causing their motion, when they are subjected to the electric fields. Various types of electrically induced forces under the action of direct current (DC) and alternating current (AC) fields can be used for the manipulation of the fluids or particles. Electrically charged particles or molecules in liquid media experience attraction towards the electrode of opposite charge under constant electric fields. This effect is called electrophoresis (EP) and arises from the motion of counterions surrounding the charged particle. The counterionic movement in the liquid layer adjacent to charged solid surfaces initiates electroosmotic flow (EOF) in the bulk fluid under the DC or AC electric fields. Another electrically induced effect that can be used for the manipulation of particle suspensions in microsystems is dielectrophoresis (DEP), which is based on the polarisation of dielectric particles in a non-uniform electric field. These electrically induced forces will be reviewed in more detail in the next subsections.

Table 1.1. Summary of the driving forces and external fields used to manipulate flows in microfluidic devices.[2]

Driving force	Subcategorization	Remarks
Pressure gradient ∇p		Familiar case as in pipe flow
Capillary effects	Surface tension, γ Thermal Electrical (electrocapillarity)	Capillary pressure difference
	Surface tension gradients, $\nabla\gamma$ Chemical Thermal Electrical Optical	Typically involve thin films Photoresponsive materials
Electric fields **E**	DC electro-osmosis AC electro-osmosis Dielectrophoresis	Uniform velocity field Rectified flows Response $\propto \nabla \mathbf{E}^2$
Magnetic field/ Lorentz forces	Magnetohydrodynamic stirring	
Rotation	Centrifugal forces	
Sound	Acoustic streaming	

1.3.1. Dielectrophoresis

When a polarizable particle is subjected to an inhomogeneous electric field, a dipole is induced in the particle. The interaction of the induced dipoles with the gradient of the field gives rise to attraction or repulsion of the particles from the high electric field region, depending on their polarizability compared with the surrounding medium as shown in Figure 1.2. This motion of particles suspended in a medium under the non-uniform electric field gradient is termed dielectrophoresis (DEP).[67] In AC electric field, the DEP force leads to net particle displacement due to its non-zero time average.[65,68-70] The use of AC field in DEP, in particular, allows the application of high field strengths without electroosmotic flows and electrolysis.[62,71,72]

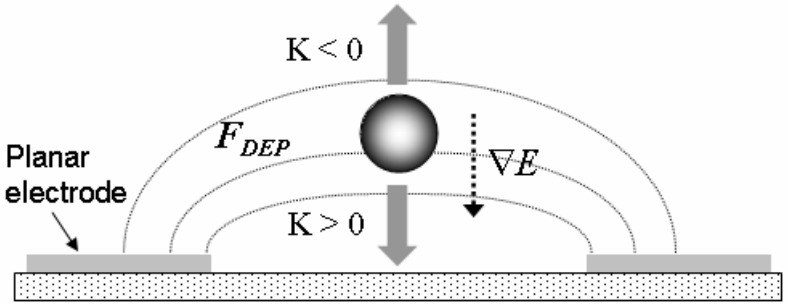

Figure 1.2. Dielectrophoretic force moves the particle along the gradient of the electric field, ∇E. The particle is either attracted to or repelled from the high field intensity region based on the sign of K.

The time averaged DEP force, F_{DEP}, is given by[63,67,72]

$$F_{DEP} = 2\pi\varepsilon_m r^3 \,\mathrm{Re}\left|K(\omega)\right|\nabla E^2 \tag{1-1}$$

where r is the radius of the particle, ε_m is the dielectric permittivity of the medium, E is the electric field intensity, and K(ω) is the Clausius-Mossotti factor, i.e., the particle's effective polarizability in media. The sign of the force on the particle depends on the real part of K(ω),

$$\mathrm{Re}\left|K(\omega)\right| = \frac{\varepsilon_p - \varepsilon_m}{\varepsilon_p + 2\varepsilon_m} + \frac{3(\varepsilon_m\sigma_p - \varepsilon_p\sigma_m)}{\tau_{MW}(\sigma_p + 2\sigma_m)^2(1+\omega^2\tau_{MW}^2)} \tag{1-2}$$

where σ_m is the conductivity of the medium, ε_p and σ_p are the dielectric permittivity and the conductivity of the particle, respectively, ω is the applied field frequency, and τ_{MW} is the

Maxwell-Wagner charge relaxation time, expressed as $\tau_{MW} = (\varepsilon_p + \varepsilon_m)/(\sigma_p + 2\sigma_m)$. Therefore, the direction in which the particle moves is not only determined by the properties of the particle and the medium but also the frequency of the applied field. For dielectric particles, the sign of the real part of K(ω) is changed at a crossover frequency of $\omega_c = (\tau_{MW})^{-1}$.[62,68,71] When $\mathrm{Re}|K(\omega)| > 0$, the particle is attracted toward the electric field maxima (positive DEP). Otherwise, the force on the particle is toward the lower field region (negative DEP). Such particle control using DEP has been used in many applications, such as assembly of microwires from metallic nanoparticle suspensions,[71,73] colloidal crystals,[74,75] and separation of dielectric particles.[76-79] A microfluidic mixer was also developed on the basis of DEP actuation, which induced chaotic trajectories of suspended particles.[80] DEP has found many useful biotechnological applications in biosensors,[81] separation and manipulation of biological particles such as yeast cells, viruses, and DNA.[82-87]

1.3.2. Electroosmosis

Electroosmosis (EOS) is the fluid motion induced by applied electric field due to the formation of electric double layer (EDL) at stagnant charged surfaces.[69,88,89] The charging of a surface in an electrolyte solution can arise from the ionization or dissociation of surface groups or from the adsorption (binding) of ions from the bulk solution onto a surface.[90] An electrostatic potential created from the surface charge attracts oppositely charged ions (counterions) from the solution and repels like-charged ions (co-ions). The charged solid surface together with the region of excess counterions near the surface forms the EDL. The surface charge is balanced by an equal amount of excess charge in the EDL. In the region of EDL, a layer of immobile counterions physically bound to the charged surface is called the Stern layer and is usually 1 ~ 2 nm thick. The electrostatic potential falls linearly across the Stern layer from the surface potential. The outer region of the Stern layer forms an atmosphere of diffuse and mobile ions in rapid thermal motion, referred to as the diffuse layer (Fig. 1.3). The ions in the diffuse layer can move in and out of the EDL to the bulk electrolyte solution. The diffuse layer spans a distance on the order of the Debye length ($1/\kappa$),

that depends solely on the properties of the electrolyte solution and not on the properties of the charged surface,[66,69,72,88,90]

$$\kappa = \left(\sum_i \frac{\rho_{\infty i} e^2 z_i^2}{\varepsilon_m \varepsilon_0 k T} \right)^{1/2} \quad [\mathrm{m}^{-1}] \tag{1-3}$$

where ρ_∞ is the concentration of ions in the bulk, e is the electronic charge, z is the ion valency, ε_0 is the dielectric permittivity of vacuum, k is the Boltzmann's constant, and T is the temperature of the system. The potential across the diffuse layer decreases exponentially.

When a constant (DC) electric field is applied parallel to the surface, the ions in the diffuse layer are attracted electrostatically towards the oppositely charged electrode. Since the counterions are predominant in the diffuse layer, a body force induced by dragging the liquid or solvent molecules around the ions in the EDL gives rise to a bulk fluid motion called electroosmotic flow (Fig. 1.4a). The velocity of the fluid is zero at the substrate surface and increases to a maximum value at a shear plane, resulting in a constant velocity through the bulk liquid phase.

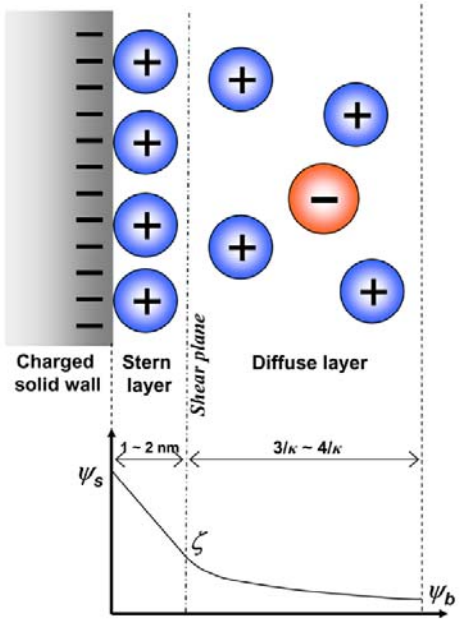

Figure 1.3. Schematic of electric double layer formation at the interface of charged surface and electrolyte solution and plot of electric potential distribution at the interface.

The flow velocity of EOF, u_{EOF} , is obtained by the balance between the electric force acting on the liquid and the frictional force (Helmholtz-Smoluchowski equation),[88,89]

$$u_{EOF} = -\frac{\varepsilon_m \zeta E}{\eta} \tag{1-4}$$

where ε_m and η are the dielectric permittivity and the dynamic viscosity of the solution, respectively, E is the electric field intensity, and ζ is the potential at the shear plane, which is defined to be the interface between a moving fluid and an immobile region, called the zeta potential. This EOF has been used to inject samples into microfluidic devices.[91-94] Valveless control of fluid flow in complex networks of intersecting capillaries had been demonstrated using EOF pumping by switching on/off different electrodes.[95,96] The magnitude and direction of the EOF in the microchannels had been controlled by changing zeta potential from the application of a perpendicular electric field through the channel wall.[92] The EOF on the surface patterned with heterogeneous charges can be used for microscale mixing.[97-99]

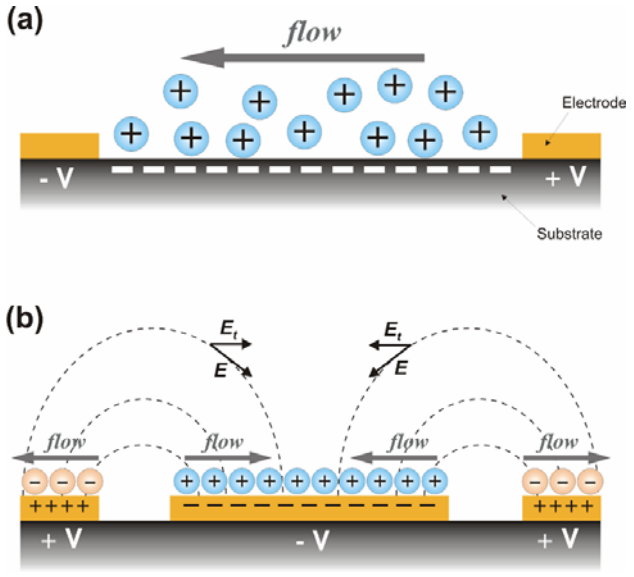

Figure 1.4. Schematics of different types of electroosmotic flow in electric field applications. (a) DC electroosmosis. Liquid flows are driven by the motion of counterions in the electric double layer near the charged wall between the energized electrodes. (b) AC electroosmosis. Interaction of the tangential field of an AC electric field gradient near the electrode edges with counterions in the electric double layer gives rise to a net fluid flows directed towards the electrodes.

Instead of the fluid response to the constant (DC) electric fields, fluid flows could be generated with microelectrodes locally integrated in microfluidic systems under the applications of AC electric field. The AC electric potential applied to the electrodes changes the native charge on the electrode surface and forms induced EDL, leading to an induced zeta potential. The ions in the induced EDL on the electrodes interact with the tangential component of the AC electric field and give rise to bulk fluid movement directed towards the electrodes. This phenomenon is called AC electroosmosis (Fig. 1.4b). In the AC electric field, the ions in the induced EDL and the tangential electric field change simultaneously with the cycles of applied AC electric field. Therefore, the direction of the net AC electroosmotic flow remains the same through the each half cycle of the AC electric field. The flow velocity of AC EOF is given by[69,100]

$$u_{AC\,EOF} = -\frac{\varepsilon_m \zeta_{ind} E_t}{\eta} \tag{1-4}$$

where ζ_{ind} is the induced zeta potential due to the applied electric field and E_t is the tangential component of the AC electric field. The AC EOF shows strong dependence on AC field frequency, which has a specific range for efficient flow velocity and otherwise tends to be zero at low and high frequencies.[101] The AC electroosmosis has been found to be a contributing force in collecting particles and cells with planar electordes.[63,65] The AC field applied to a system consisting of patterned vertical electrodes led to particles or yeast cell concentration in the center of conductive "corrals" on the silicon wafer acting as bottom electrode with the combination of DEP and AC electroosmosis.[100] AC fields were applied to dilute suspensions of latex microspheres enclosed between a patterned silicon wafer and an ITO-coated glass slide in a small chamber. The latex particles became collected in the center of the conductive "corrals" on the silicon wafer acting as bottom electrode. With optimization of the operating parameters in the AC EOF, the concentration of λ phage DNA and single strand DNA fragments as small as 20 bases had been demonstrated.[102] The AC EOF on asymmetric electrode pairs have been also applied for fluid pumping in a microfluidic channel, which have potential advantages of local fluidic control and requirement of low

driving voltage.[63,103,104] In the next section, we will describe a new type of microfluidic devices and novel applications of micro- and nanofluidic phenomena.

1.4. New Types of Microfluidic Systems and Various Applications of Microfluidics and Microflows

1.4.1. Droplet-Based Microfluidics

Since the advent of microfluidics, the motion of liquids and particles in most lab-on-a-chip devices has been conducted in continuous single flow systems. These conventional microfluidic chips could have drawbacks, including adhesion of suspended particles, cells or proteins to the walls, and undesired clogging of channels.[105,106] Multiphase flow systems in the form of droplets or channel-spanning slugs have emerged as an alternative technology in the microfluidics with potential advantages of enhancing the performance of the single phase flow systems.[2,64,106,107-109] Droplets surrounded by an immiscible fluid like oil or air in microchannels can avoid lateral dispersion (Taylor dispersion). Discrete tiny droplets enable fast thermal transfer and rapid mixing due to high surface to volume ratio, resulting in decreased reaction times. In addition, the droplet-based microfluidic platforms are well suited for high throughput screening applications, because almost identical droplets can be produced at high frequencies and multiple reactions or assays are enabled without increasing the size of devices or complexity.

Depending on the mode of droplet actuation, droplet-based microfluidic systems can be categorized into two platforms, channel-based (one-dimensional) and planar surface (two-dimensional) approaches.[64] Since droplet formation at the junction of two microchannels containing water and oil surfactant mixture was demonstrated by Thorsen *et al.* in 2001,[110] many research efforts have been focused on generation, breakup, fusion, and mixing of droplets within closed microchannels using pressure-driven flows (Fig. 1.5). In channel-based systems, droplets have been formed at T-shaped junction[110-113] and flow focusing channel structure[114-117] by high shear forces generated at the interface between dispersed phase and continuous phase. The size of resulting droplets is highly uniform and can be controlled by the flow rate of streams and the channel geometry.[107,116,117]

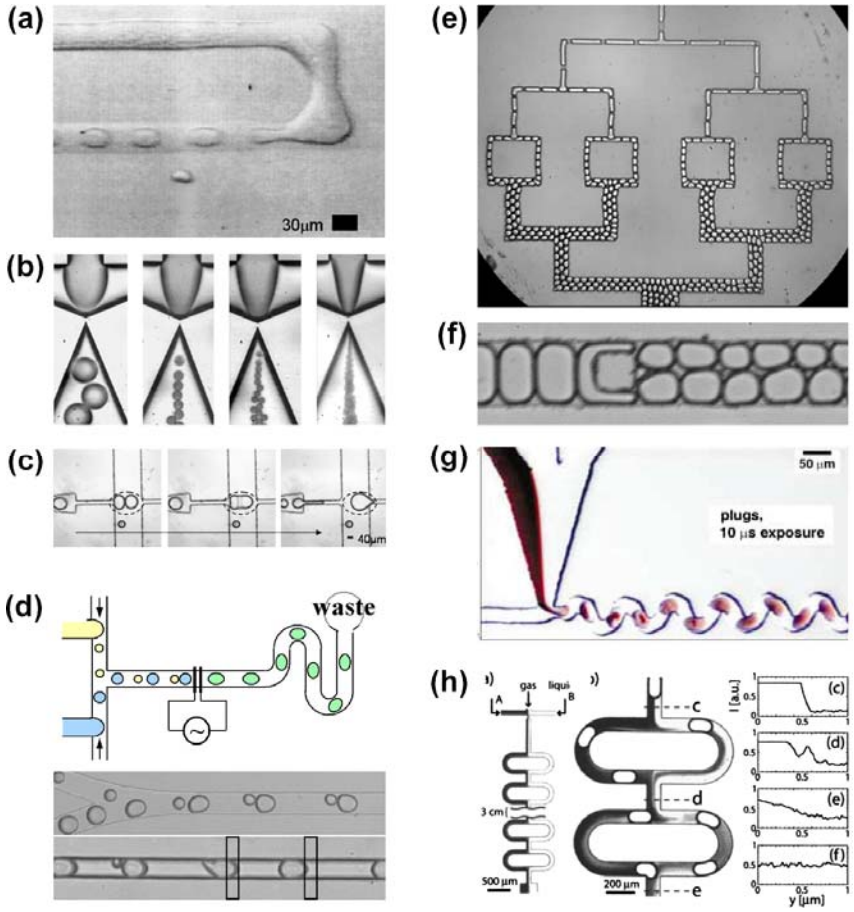

Figure 1.5. Manipulation of droplets in microfluidic channels. (a) Formation of water-in-oil droplets with T-junction[110] and (b) flow focusing design.[116] As oil flow rate increases (from left to right in (b)), droplet size is reduced with increasing frequency of formation. (c) Passive fusion of a series of three droplets in flow rectifying design[120] and (d) active fusion of water droplets with two different sizes by an electric field when they pass over the electrodes.[121] (e) Sequential breakup of droplets in a series of T-junctions and (f) fission of water-in-oil droplets caused by a square obstruction in a microchannel.[119] (g) Mixing inside liquid plugs traveling through winding channels.[118] (h) Gaseous slugs flowing through a microchannel network lead to stretching and folding of continuous phase liquids.[122]

Splitting of a single droplet into two or more droplets has been performed with T-junction and channel obstructions by varying flow rate of the continuous phase and channel resistances.[118-120] Controlled fusion and mixing of droplets are essential for reactions or assays within the droplets. Droplet fusion has been successfully achieved using expended channel configurations[118,120] and with an electric field.[121] Mixing inside the droplets has been

enhanced by internal recirculation during the transportation through winding channels[118] and gaseous slugs flowing through microchannel network also led to effective microfluidic mixing of continuous fluids.[122] Excellent reviews on more details behind these operations of droplets in the microchannels have been published in recent years.[2,109,123-125]

The droplets streaming in the microchannels can be used as reaction confinement sites for material syntheses and bioassays. Jensen *et al.* synthesized colloidal nanoparticles, *e.g.*, silica nanoparticles and CdSe quantum dots, in segmented gas-liquid flows with a narrow size distribution.[126-128] Droplets obtained in the flow focusing device or T-junction configuration have been used for continuous synthesis of various types of polymer particles by solidifying the droplets, resulting in highly monodisperse,[129] nonspherical,[130] Janus,[117,131] and mesoporous silica microparticles.[132] Weitz *et al.* showed monodisperse double or multiple emulsions using the flow focusing technique by interleaved glass capillary arrangements and demonstrated uniform microencapsulations, functional microgels, and nanoparticle colloidosomes with selective permeability.[133-136] Protein crystallization has been performed in nanoliter-size droplets transported inside glass capillaries by Ismagilov *et al*.[137,138]

In the planar surface-based systems, discrete droplets are manipulated on a two-dimensional (2D) array of electrodes configured for electrowetting on dielectric and dielectrophoresis. This type of droplet-based microfluidic device has additional advantages of more compact and simple system by eliminating external pumps and channels, independent control of many droplets, and easy automation under software-driven electronic control. Droplets controlled by using electrowetting is sandwiched between two planes.[139,140] The bottom layer contains addressable electrode array and the top one is a ground electrode. Insulating dielectric layers are covered on top of both electrodes to separate the droplets from the electrodes. The application of an electric field changes the interfacial energy between the liquid and the insulating layer. The contact angle of droplet at the energized electrode is lowered, causing the droplet to move along the activated electrodes. On-chip droplet manipulation, such as dispensing, merging, and fission of the droplets, has been demonstrated using programmable electrowetting microdevices (Fig. 1.6a and c).[140-143]

Droplet mixing on the electrowetting-based microdevice was accomplished by oscillating the droplet placing between two electrodes (Fig. 1.6b).[144,145]

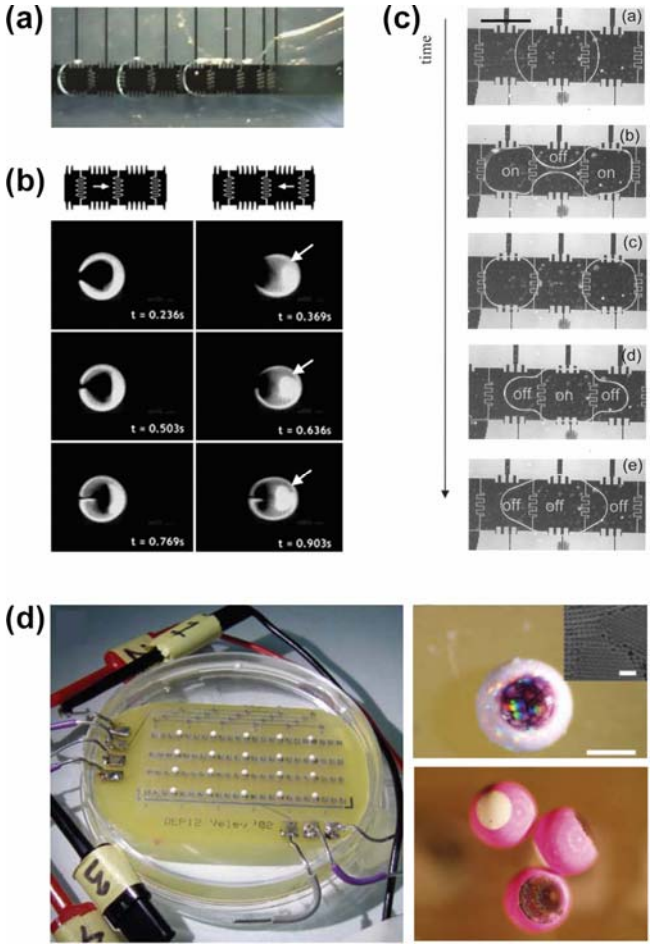

Figure 1.6. Manipulation of droplets on planar systems. (a) Dispensing of uniform microdroplets from on-chip liquid reservoir.[140] (b) Time-lapsed images of mixing in oscillating droplets on two electrodes at 8 Hz of frequency.[144] (c) Sequential images of breakup and merging of droplets through surface electrodes.[142] (d) Droplet and particle entrapment in DEP-based chip.[149] Multiple droplets of 1μL containing polystyrene microspheres are trapped by DEP above electrode matrix in a fluorinated oil layer. Anisotropic eyeball supraparticles and striped multilayer particles are synthesized in the floating aqueous droplets.

An alternative principle for on-chip droplet manipulation is based on DEP. The DEP liquid actuation can be achieved without a second electrode common in the electrowetting-

based devices. This allows completely avoiding the droplet contact with solid surfaces. The surface contamination is reduced or eliminated. Jones *et al.* demonstrated uniform aqueous droplet dispensing in an open structure consisting of parallel, coplanar electrodes coated dielectric layer.[146-148] Velev *et al.* developed a new type of DEP-based lab-on-a-chip system for manipulating freely suspended droplets without any contact with solid surface (Fig. 1.6d).[105,149] Water or hydrocarbon droplets floating on a dense fluorinated oil were transported synchronously in parallel or merged for rapid mixing by applying AC electric field through electrode arrays under the oil. Gascoyne and co workers demonstrated programmable fluidic processors based on DEP force.[150,151] Water droplets were formed at pressurized orifices near electrodes and manipulated in an immiscible, low permittivity medium on electrode arrays.

Electrophoretic separation and concentration of suspended particles in the droplets driven by the electrowetting were demonstrated by Kim *et al*.[152] Fair *et al.* performed a colorimetric enzymatic glucose assay on human physiological fluids with a fully integrated and reconfigurable electrowetting-based microdevice.[153] Each of droplets controlled by the DEP-based liquid chip system was served as a microreactor. Velev *et al.* demonstrated on-chip assembly, drying and polymerization to create binary or ternary supraparticles, polymer capsule and semiconducting microbeads, and particle agglutination immunoassay.[149, 216]

1.4.2. Autonomously Moving Microdevices

Development of nano- and microscale particles and devices capable of autonomous movement through a fluid environment is one of the challenges in nanotechnology. Such tiny machines might open a vast array of potential applications in vehicles for delivery of medicines in human body, roving sensors, material transporters in microfluidic chips, and tools for environmental monitoring for toxic organic molecules. Conventional driving forces on the macroscale range to transport and manipulate micro or sub-microscale objects, however, are mostly inefficient in the regime of low Reynolds numbers, where viscous effects and surface forces are predominant,[154-156] as described in section 1.3. The motility in this regime can not be achieved by inertial force and jet propulsion, which are usual ways for

macroscopic movements.[154,157] Another obstacle for the propulsion of microdevices in a fluid phase is numerous Brownian collisions between molecules and microscale objects.[90,158,159] Dusenbery reported that minimum size limit for useful locomotion by free-floating bacteria is about 600 nm diameter due to the Brownian collision.[160] Therefore, key to the development of self-propelling micromachines is the formulation of effective propulsion force for driving their motion in the low Reynolds number regime.

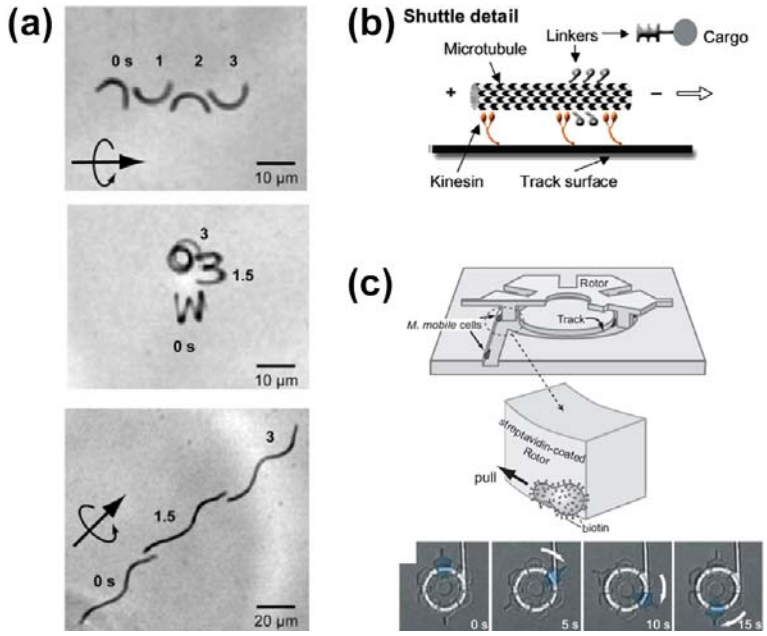

Figure 1.7. Examples of autonomously moving hybrid systems, combining synthetic components and biomolecular motors. (a) Superimposed time-lapse images showing the motion of crescent-shaped and spiral-shaped cells, swimming immediately after its release into solution.[168] (b) Schematic of surface-bound kinesin motor proteins to transport functionalized microtubule shuttle along patterned tracks.[167] (c) Schematic illustration of a microrotor (20 µm diameter) driven by the gliding bacteria that adhere to the rotor (top) and time-lapse photomicrographs of a unidirectionally rotating rotor within the track (bottom).[170]

Autonomous motion of objects on the microscale has been achieved in the form of hybrid bionanomachines (Fig. 1.7) and completely synthetic artificial micromachines in recent years (Fig. 1.8). A variety of biological motors are able to impart directed motion to microorganisms.[159,161,162] Notable examples of biomotors are kinesin and myosin proteins, which can convert chemical potential energy into propulsion force by hydrolyzing adenosine

triphosphate (ATP).[161-163] Flagella biological motors in some microorganisms, like *Escherichia coli*, provide locomotion to the bacterial cell body in the fluid environments through a 'corkscrew' motion of the flagella.[154,164,165] Montemagno *et al.* demonstrated a hybrid rotary device assembled from an enzyme ATP synthase and submicrometer-sized nickel rods.[166] Kinesin motor along photolithographically predefined tracks on a surface was used for transporting functionalized microtubules as material shuttles.[167] Filamentous cells of *E. coli* grown in microchambers patterned in agarose gel have been observed to form crescent, zigzag, sinusoidal, and spiral shapes and self-propelled in solution without releasing the defined shapes.[168] Whitesides *et al.* showed that motile unicellular algae served as a transporter of polystyrene microspheres in a microfluidic chip by phototaxis.[169] Hiratsuka *et al.* reported another hybrid micromachine of unidirectionally rotating microrotor powered by a motile bacterium adhered to the rotor.[170] The problems encountered in developing hybrid micromachines from the point of view of application are inconvenience and production of waste from chemical fuelling, limited durability and operating conditions outside the cellular environments, and difficulty of controlling their motion.

In recent years, autonomous mechanical movement of artificial molecular motors or micromachines has begun to be investigated. The self-propelling synthetic devices could provide more robust, practical applications than their natural counterparts. Asymmetrical structure in the device design, power source for the propulsion, and its transduction to the mechanical forces are essential to the developments of self-propelling artificial microdevices.[157,159,171]

A number of synthetic molecular machines have been made of light-responsable organic molecules as a linear shuttle, rotor, and molecular elevator.[172-174] Vicario *et al.* demonstrated the rotation of micrometer-sized glass rod induced by the light-driven molecular motor doping in a liquid crystal film.[175] Most intense research for the autonomously moving micromachines has been conducted by using catalytic decomposition of hydrogen peroxide ($2H_2O_2 \rightarrow O_2 + 2H_2O$), resulting in a nanobubble generation. Whitesides and co-workers reported the first demonstration of the self-propelling motion driven by the catalytic reaction at the platinum asymmetrically placed on PDMS

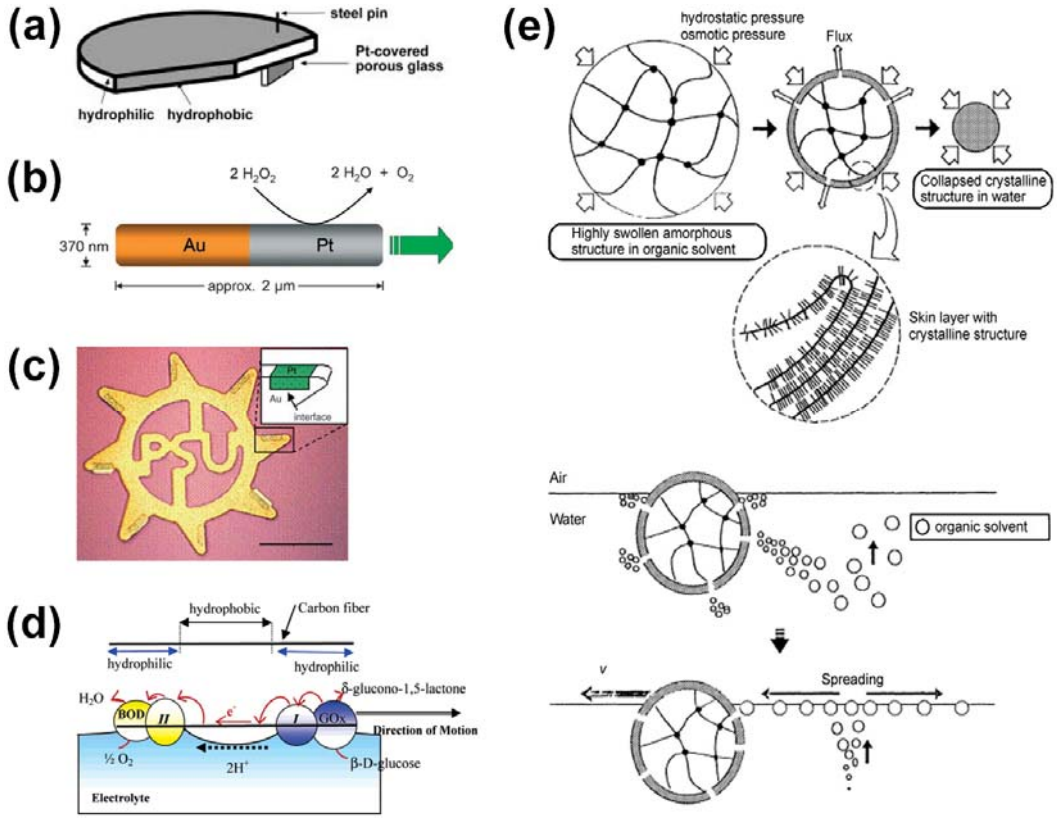

Figure 1.8. Examples of spontaneously propelling artificial nano- and micromachines. (a) Schematic of a self-propelling machine consisting of a PDMS plate (1 ~ 2 mm thick and 9 mm diameter) and a porous glass filter covered with platinum.[176] (b) Schematic of an asymmetric gold/platinum nanorod propelled predominantly along its axis in the direction of the platinum driven by the catalytic decomposition of hydrogen peroxide fuel.[159,177] (c) Photograph of a gold gear with platinum deposited in the tooth regions. The arrow in the inset indicates the region where the surface tension gradient is formed (scale bar is 50 μm).[182] (d) Schematic illustration of a self-propelled bioelectrochemical motor driven by the reaction of glucose and oxygen based on functionalized carbon fibers with two redox-coupled enzymes.[184] (e) Schematic illustrations of extraction of organic solvent from a solvent-swollen polymer gel (top) and the mechanism for its motion due to solvent spreading at the air-water interface (bottom).[188]

structures.[176] Various types of artificial nanometer-sized objects in the form of gold/platinum or nickel bimetallic nanorods, nanorotors, and microparticles with synthetic catalase have shown chemically powered translational and rotational motion in hydrogen peroxide solution.[177-183] The origin of the propulsion force in this system is still controversial, whether it is initiated by catalytically induced electrokinetic phenomenon, gas propulsion, reduction

of viscous friction, or something else entirely.[159,171] Mano and Heller described a bioelectrochemical locomotion induced by the reaction of glucose and oxygen at the floating carbon fiber functionalized with two redox-coupled enzymes.[184] Asymmetric releasing of surface active agents can impart spontaneous motion to small objects floating at the air/water interface by lowering surface free energy. Preferential dissolution of a camphor placed on water surface caused the self-motion of the camphor boat by creating a gradient in surface tension of air/water interface.[185-187] Osada *et al.* demonstrated self-propulsion of organic solvent-swollen amphiphilic polymer gels, when they were placing on the water surface.[188-191] The swelling solvents asymmetrically ejected by osmotic and hydrostatic pressures across the crystallized polymer layer reduce the surface tension locally and lead to the solvent-driven spontaneous gel motion.

1.4.3. Ionic Current Control in Micro- and Nanofluidic Systems

Ionic transport in nanoscale structures has attracted broad interest in various research fields, motivated by ionic transport through biological channels or lipid cell membranes in many physiological processes of a living organism.[192-194] Channel structures on nanoscale range have also promising potential for ultrasensitive detection of a single molecule or biomolecule. The nonlinear current resulting from the preferential direction of the ion flow has been used for signal transmission as well as signal processing, like ionic current rectification and amplification as in electronic circuits. Advantages of the electronic signal processing systems using the ionic current conduction is the capability of operation in aqueous phase and biomedical and chemical applications in molecule delivery and sensing.

Initially, current carried by ions was investigated with the aim to develop electronic devices analogues to semiconductor diodes and transistors. Lovreček *et al.* showed in 1959 ionic current rectification using an electrolytic junction, so-called electrolyte diode, which consisted of proton-rich and hydroxide-rich electrolyte solutions separated by thin bipolar membrane.[195] The flow of ions across the electrolytic junction was considered a replacement of the motion of electrons and holes in the semiconducting p-n junction. Noszticzius *et al.* and Lindner *et al.* described recently experimental research and mathematical modeling of

the electrolyte diode in the form of two acidic and basic reservoirs contented by a cylindrical hydrogel.[196-198]

Recent development of nanofabrication techniques led to the emergence of nonlinear ionic flux through nanofluidics systems with asymmetric geometrics or charge distributions on the channel walls (Fig. 1.9). This novel technique of ionic transports is capable of biomimetic ionic transport phenomena and highly sensitive detection of biomolecules. Siwy *et al.* and Gracheva *et al.* demonstrated ionic current rectifiers by controlling ion flows in the tapered, cone-shaped nanopores with excess surface charge or single-stranded DNA attached to the nanotube walls.[194,199-203] Umehara *et al.* reported that the polarity of rectified ionic current through quartz nanopiptte electrodes was controllable by changing the surface charge with a positively charged poly-L-lysine coating.[204]

As the size of channels is reduced in the range of the Debye length (1 ~ 100 nm), ionic conductance through the nanochannels is completely governed by surface charge instead of bulk ionic concentration, enabling various current-voltage characteristics analogous to those of semiconductor diodes and transistors.[205-208] The rectification of ionic transport in nanofluidic diodes was performed by introducing asymmetric surface charge distributions in the nanochannel walls, *e.g.* using diffusion-limited patterning.[209-211] Diode-like current response was also shown in silica nanochannels with homogeneous surface charge density, placed between two electrolyte solutions of different concentrations by Cheng and Guo.[207] Nanofluidic bipolar ionic transistors were demonstrated by using discontinuous surface charge patterning inside a single nanopore or nanochannel.[209,212] Majumdar and co-workers reported nanofluidic field-effect transistors by locally modifying the surface charge density using electrostatic fields with gate voltage modulation.[205,206,213-215] The regulation of proton, DNA, and protein transport by the electrostatic gating was experimentally realized in the field-effect ionic transistors.

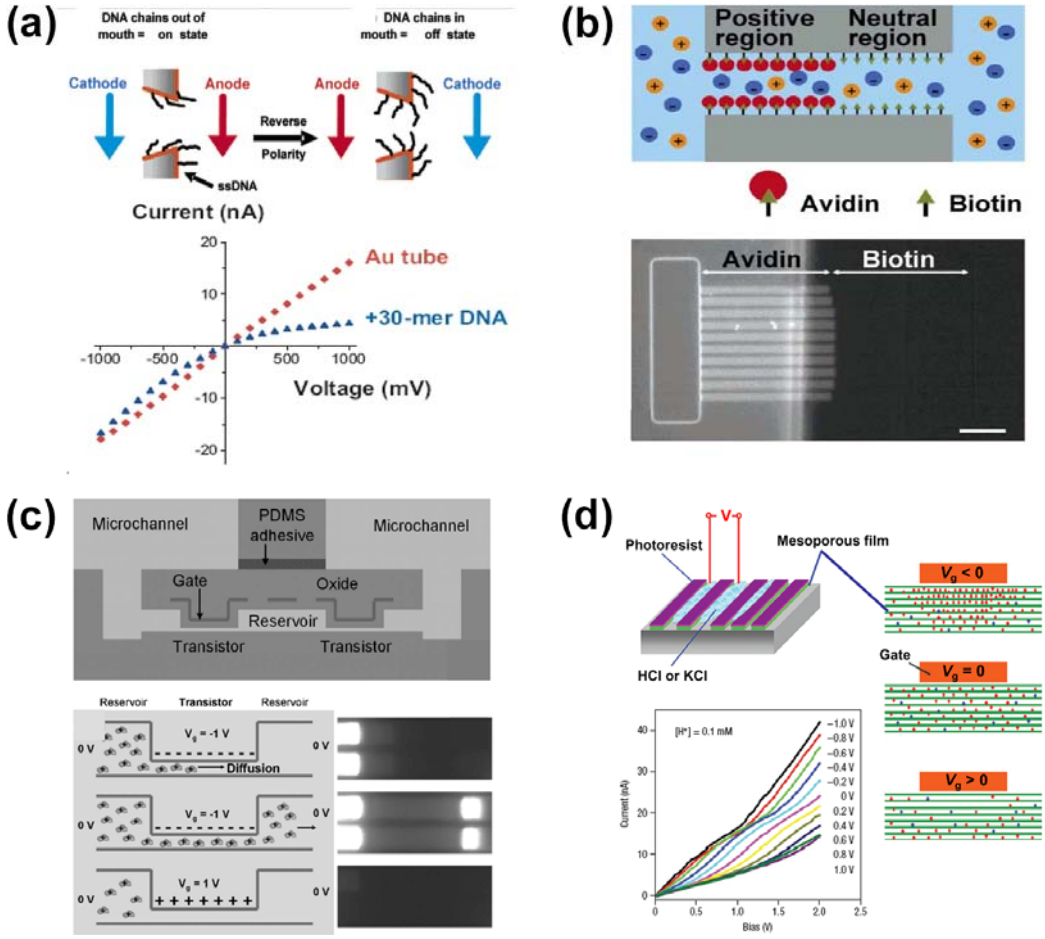

Figure 1.9. Nonlinear ionic current control in nanofluidic devices. (a) Schematics of ionic current rectifier with a conical gold-nanotube showing electrode polarity and DNA chain positions for on and off states (top). Current-Voltage (*I-V*) characteristics of the nanopore current rectifier before and after modification with thiolated single-stranded DNA (bottom).[199,202] (b) Schematic of a nanofluidics diode with discontinuous surface charge patterned by cationic protein avidin in half the nanochannel and biotin moieties in the other half (top). Fluorescent image of the fabricated nanofluidics diode by introducing fluorescently labeled avidin in half the channel wall (bottom).[210] (c) Schematic of nanofluidics field-effect transistor system connected with microfluidic channels on either side (top). Illustration in the bottom shows diffusion of the avidin attracted near the nanochannel entrance when the gate electrode is turned on (Vg = -1 V) without bias between the microchannels. But the protein was not observed in the channel or in the central reservoir with Vg = + 1 V, because positively charged avidin was repelled out of the channel. Fluorescence images are corresponding to the schematics in the left.[214] (d) Schematic diagram of the measurement of proton conductivity through aligned mesoporous silica films (top left). The gate effect of cation (red) and anion (blue) distribution within nanochannels is illustrated in the left and accordingly ionic current is modulated by this electrostatic gating, as shown in the *I-V* curves (bottom left).[215]

1.5. Layout of this Dissertation

My graduate research was focused mainly on the manipulation of fluids and particles on microscale. I used electrically induced forces to develop new tools for lab-on-a-chip devices and innovative applications for autonomously moving micromachines and electronic components. The work described in Chapter 2 is the fundamental investigation of particle transport and separation inside an evaporating microdroplet floating on a dielectrophoretic liquid chip with the help of numerical simulation. Label-free immuno-agglutination bioassay directly based on the microseparation process within the droplet is presented. Chapter 3 presents self-propelling particles based on miniature diodes driven by particle-localized electroosmotic flow powered by an external alternating electric field. Autonomous motion of the tiny electronic components with complex additional functionalities is demonstrated. Chapter 4 details the use of miniature diodes to make novel microfluidic systems. The effective microfluidic pumping and mixing were achieved by the locally distributed miniature diodes immobilized on the channel walls. In Chapter 5, new microfluidic materials containing photocurable polymers inside microchannel networks are introduced. This novel material can acquire specific shapes on demand by solidifying the photoresist in the channels, resulting in significant improvement of bending and stretching mechanical properties. Chapter 6 presents aqueous gel-based ionic current rectifiers as an alternative electronic component. A fixed junction between two agarose gels doped with oppositely charged polyelectrolytes could rectify electric current carried by the mobile counterions. Chapter 7 summarizes my graduate research and provides the outlook for extending this work.

1.6. References

[1] Whitesides, G. M. and Stroock, A. D., Flexible methods for microfluidics. *Phys. Today* (2001) 54, 42-47.

[2] Stone, H. A., Stroock, A. D. and Ajdari, A., Engineering flows in small devices: Microfluidics toward a Lab-on-a-Chip. *Annu. Rev. Fluid Mech.* (2004) 36, 381-411.

[3] Jensen, K. F., Microchemical systems: Status, challenges and opportunities. *AIChE J.* (1999) 45, 2051-2054.

[4] Stone, H. A. and Kim, S., Microfluidics: Basic issues, applications and challenges. *AIChE J.* (2001) 47, 1250-1254.

[5] Squires, T. M. and Quake, S. R., Microfluidics: Fluid physics at the nanoliter scale. *Rev. Mod. Phys.* (2005) 77, 977-1026.

[6] Whiteside, G. M., The origins and the future of microfluidics. *Nature* (2006) 442, 368-373.

[7] Verpoorte, E. and de Rooij, N. F., Microfluidics meets MEMS. *Proc. IEEE* (2003) 91, 930-953.

[8] Kamholz, A. E., Proliferation of microfluidics in literature and intellectual property. *Lab Chip* (2004) 4, 16N-20N.

[9] Terry, S. C., Jerman, J. H. and Angell, J. B., A gas chromatographic air analyzer fabricated on a silicon wafer. *IEEE Trans. Electron Devices* (1979) ED-26, 1880-1886.

[10] Bassous, E., Taub, H. H. and Kuhn, L., Ink jet printing nozzle arrays etched in silicon. *Appl. Phys. Lett.* (1977) 31, 135-137.

[11] Petersen, K. E., Fabrication of an integrated, planar silicon ink-jet structure. *IEEE Trans. Electron Devices* (1979) ED-26, 1918-1920.

[12] Gravesen, P., Branebjerg, J. and Jensen, O. S., Microfluidics - a review. *J. Micromech. Microeng.* (1993) 3, 168-182.

[13] Manz, A., Graber, N. and Widmer, H. M., Miniaturized total chemical analysis systems: A novel concept for chemical sensing. *Sens. Actuators* (1990) B1, 244-248.

[14] Yager, P., Edwards, T., Fu, E., Helton, K., Nelson, K., Tam, M. R. and Weigl, B. H., Microfluidic diagnostic technologies for global public health. *Nature* (2006) 442, 412-418.

[15] Zhang, C., Xu, J., Ma, W. and Zheng, W., PCR microfluidic devices for DNA amplification. *Biotechnol. Adv.* (2006) 24, 243-284.

[16] Tüdós, A. J., Besselink, G. A. J. and Schasfoort, R. B. M., Trends in miniaturized total analysis systems for point-of-care testing in clinical chemistry. *Lab Chip* (2001) 1, 83-95.

[17] van Lintel, H. T. G., van de Pol, F. C. M. and Bouwstra, S., A piezoelectric

micropump based on micromachining of silicon. *Sens. Actuators* (1988) 15, 153-167.

[18] Gass, V., van der Schoot, B. H., Jeanneret, S. and de Rooij, N. F., Integrated flow-regulated silicon micropump. *Sens. Actuators A* (1994) 43, 335-338.

[19] Bosch, D., Heimhofer, B., Muck, G., Seidel, H., Thumser, U. and Welser, W., A silicon microvalve with combined electromagnetic/electrostatic actuation. *Sens. Actuators A* (1993) 37-38, 684-692.

[20] Ohnstein, T., Fukiura, T., Ridley, J. and Bonne, U., Micromachined silicon microvalve. *Proc. MEMS 90, An Investigation of Micro Structures, Sensors, Actuators, Machines and Robots, New York, USA* (1990) 95-98.

[21] Schwesinger, N., Frank, T. and Wurmus, H., A modular microfluid system with an integrated micromixer. *J. Micromech. Microeng.* (1996) 6, 99-102.

[22] Verpoorte, E. M. J., van der Schoot, B. H., Jeanneret, S., Manz, A., Widmer, H. M. and de Rooij, N. F., Three-dimensional micro flow manifolds for miniaturized chemical analysis systems. *J. Micromech. Microeng.* (1994) 4, 246-256.

[23] Manz, A., Harrison, D. J., Verpoorte, E. M. J., Fettinger, J. C., Paulus, A., Lüdi, H. and Widmer, H. M., Planar chips technology for miniaturization and integration of separation techniques into monitoring systems – Capillary electrophoresis on a chip. *J. Chromatogr.* (1992) 593, 253-258.

[24] Jacobson, S. C., Hergenröder, R., Koutny, L. B. and Ramsey, J. M., High-speed separations on a microchip. *Anal. Chem.* (1994) 66, 1114-1118.

[25] Harrison, D. J., Fluri, K., Seiler, K., Fan, Z., Effenhauser, C. S., and Manz, A., Micromachining a miniaturized capillary electrophoresis-based chemical analysis system on a chip. *Science* (1993) 261, 895-897.

[26] Kim, E., Xia, Y. and Whitesides, G. M., Polymer microstructures formed by moulding in capillaries. *Nature* (1995) 376, 581-584.

[27] Duffy, D. C., McDonald, J. C., Schueller, O. J. A. and Whitesides, G. M., Rapid prototyping of microfluidic systems in poly(dimethylsiloxane). *Anal. Chem.* (1998) 70, 4974-4984.

[28] McDonald, J. C., Duffy, D. C., Anderson, J. R., Chiu, D. T., Wu, H., Schueller, O. J. A. and Whitesides, G. M., Fabrication of microfluidic systems in poly(dimethylsiloxane). *Electrophoresis* (2000) 21, 27-40.

[29] Delamarche, E., Juncker, D. and Schmid, H., Microfluidics for processing surfaces and miniaturizing biological assays. *Adv. Mater.* (2005) 17, 2911-2933.

[30] Bange, A., Halsall, B. and Heineman, W. R., Microfluidic immunosensor systems. *Biosens. Bioelectron.* (2005) 20, 2488-2503.

[31] Becker, H. and Locascio, L. E., Polymer microfluidic devices. *Talanta* (2002) 56, 267-287.

[32] Laser, D. J. and Santiago, J. G., A review of micropumps. *J. Micromech. Microeng.* (2004) 14, R35-R64.

[33] Iverson, B. D. and Garimella, S. V., Recent advances in microscale pumping technologies: a review and evaluation. *Microfluid. Nanofluid.* (2008) 5, 145-174.

[34] Chang, C-C. and Yang, R-J., Electrokinetic mixing in microfluidic systems. *Microfluid. Nanofluid.* (2007) 3, 501-525.

[35] Nguyen, N-T. and Wu, Z., Micromixers - A review. *J. Micromech. Microeng.* (2005) 15, R1-R16.

[36] Pamme, N., Continuous flow separations in microfluidic devices. *Lab Chip* (2007) 7, 1644-1659.

[37] Andersson, H. and van den Berg, A., Microfluidic devices for cellomics: A review. *Sens. Actuators B* (2003) 92, 315-325.

[38] Khandurina, J. and Guttman, A., Bioanalysis in microfluidic devices. *J. Chromatogr. A* (2002) 943, 159-183.

[39] Hansen, C. and Quake, S. R., Microfluidics in structural biology: Smaller, faster… better. *Curr. Opin. Struct. Biol.* (2003) 13, 538-544.

[40] Mouradian, S., Lab-on-a-chip: Applications in proteomics. *Curr. Opin. Chem. Biol.* (2001) 6, 51-56.

[41] Sun, Y. and Kwok, Y. C., Polymeric microfluidic system for DNA analysis. *Anal. Chim. Acta* (2006) 556, 80-96.

[42] Horsman, K. M., Bienvenue, J. M., Blasier, K. R. and Landers, J. P., Forensic DNA analysis on microfluidic devices: A review. *J. Forensic Sci.* (2007) 52, 784-799.

[43] Schulte, T. H., Bardell, R. L. and Weigl, B. H., Microfluidic technologies in clinical

diagnostics. *Clin. Chim. Acta* (2002) 321, 1-10.

[44] Dittrich, P. S. and Manz, A., Lab-on-a-chip: Microfluidics in drug discovery. *Nat. Rev. Drug Discovery* (2006) 5, 210-218.

[45] Pihl, J., Karlsson, M. and Chiu, D. T., Microfluidic technologies in drug discovery. *Drug Discovery Today* (2005) 10, 1377-1383.

[46] Kang, L., Chung, B. G., Langer, R. and Khademhosseini, A., Microfluidics for drug discovery and development: From target selection to product lifecycle management. *Drug Discovery Today* (2008) 13, 1-13.

[47] Song, Y., Hormes, J. and Kumar, C. S. S. R., Microfluidic synthesis of nanomaterials. *Small* (2008) 4, 698-711.

[48] Hung, L-H. and Lee, A. P., Microfluidic devices for the synthesis of nanoparticles and biomaterials. *J. Med. Biol. Eng.* (2007) 27, 1-6.

[49] Serra, C. A. and Chang, Z., Microfluidic-assisted synthesis of polymer particles. *Chem. Eng. Technol.* (2008) 31, 1099-1115.

[50] Manz, A., Effenhauser, C. S., Burggraf, N., Harrison, D. J., Seiler, K. and Fluri, K., Electroosmotic pumping and electrophoretic separations for miniaturized chemical analysis systems. *J. Micromech. Microeng.* (1994) 4, 257-265.

[51] Beebe, D. J., Mensing, G. A. and Walker, G. M., Physics and applications of microfluidics in biology. *Annu. Rev. Biomed. Eng.* (2002) 4, 261-286.

[52] Stroock, A. D., Dertinger, S. K. W., Ajdari, A., Mezić, I., Stone, H. A. and Whitesides, G. M., Chaotic mixer for microchannels. *Science* (2002) 295, 647-651.

[53] Burns, M. A., Johnson, B. N., Brahmasandra, S. N., Handique, K., Webster, J. R., Krishnan, M., Sammarco, T. S., Man, P. M., Jones, D., Heldsinger, D., Mastrangelo, C. H. and Burke, D. T., An intergrated nanoliter DNA analysis device. *Science* (1998) 282, 484-487.

[54] Unger, M. A., Chou, H-P., Thorson, T., Scherer, A. and Quake, S. R., Monolithic microfabricated valves and pumps by multilayer soft lithography. *Science* (2000) 288, 113-116.

[55] Sammarco, T. S. and Burns, M. A., Thermocapillary pumping of discrete drops in microfabricated analysis devices. *AIChE J.* (1999) 45, 350-366.

[56] Prins, M. W. J., Welters, W. J. J. and Weekamp, J. W., Fluid control in multichannel structures by electrocapillary pressure. *Science* (2001) 191, 277-280.

[57] Zhao, B., Moore, J. S. and Beebe, D. J., Surface-directed liquid flow inside microchannels. *Science* (2001) 291, 1023-1026.

[58] Walker, G. M. and Beebe, D. J., A passive pumping method for microfluidic devices. *Lab Chip* (2002) 2, 131-134.

[59] Kataoka, D. E. and Trolan, S. M., Patterning liquid flow on the microscopic scale. *Nature* (1999) 402, 794-797.

[60] Gallardo, B. S., Gupta, V. K., Eagerton, F. D., Jong, L. I., Craig, V. S., Shah, R. R. and Abbott, N. L., Electrochemical principles for active control of liquids on submillimeter scales. *Science* (1999) 283, 57-60.

[61] Stroock, A. D., Ismagilov, R. F., Stone, H. A. and Whitesides, G. M., Fluidic ratchet based on Marangoni-Bénard convection. *Langmuir* (2003) 19, 4358-4362.

[62] Velev, O. D., in *Colloids and Colloid Assemblies*, Caruso, F., Ed., Wiley-VCH, Weinheim, 2003.

[63] Wong, P. K., Wang, T-H., Deval, J. H. and Ho, C-M., Electrokinetics in micro devices for biotechnology applications. *IEEE/ASME Trans. Mechatron.* (2004) 9, 366-376.

[64] Haeberle, S. and Zengerle, R., Microfluidic platforms for lab-on-a-chip applications. *Lab Chip* (2007) 7, 1094-1110.

[65] Ramos, A., Morgan, H., Green, N. G. and Castellanos, A., AC electrokinetics: A review of forces in microelectrode structures. *J. Phys. D: Appl. Phys.* (1998) 31, 2338-2353.

[66] Bhatt, K. H., *On-chip manipulation and controlled assembly of colloidal particles using alternating electric fields*, Dissertation, North Carolina State University, Raleigh, USA, 2006.

[67] Pohl, H. A., The motion and precipitation of suspensoids in divergent electric fields. *J. Appl. Phys.* (1951) 22, 869-871.

[68] Jones, T. B., *Electromechanics of Particles*, Cambridge Press, Cambridge, 1995.

[69] Morgan, H. and Green, N. G., *AC Eelectrokinetics: colloids and nanoparticles*,

Research Studies Press Ltd., UK, 2003.

[70] Catellanos, A., Ramos, A., Gonzalez, A., Green, N. G. and Morgan, H., Eelectrohydrodynamics and dielectrophoresis in microsystems: scaling laws. *J. Phys. D: Appl. Phys.* (2003) 36, 2584-2597.

[71] Bhatt, K. H. and Velev, O. D., Control and modeling of the dielectrophoretic assembly of on-chip nanoparticle wires. *Langmuir* (2004) 20, 467-476.

[72] Velev, O. D. and Bhatt, K. H., On-chip micromanipulation and assembly of colloidal particles by electric fields. *Soft Matter* (2006) 2, 738-750.

[73] Hermanson, K. D., Lumsdon, S. O., Williams, J. P., Kaler, E. W. and Velev, O. D., Dielectrophoretic assembly of electrically functional microwires from nanoparticle suspensions. *Science* (2001) 294, 1082-1086.

[74] Lumsdon, S. O., Kaler, E. W., Williams, J. P. and Velev, O. D., Dielectrophoretic assembly of oriented and switchable two-dimensional photonic crystals. *Appl. Phys. Lett.* (2003) 82, 949-951.

[75] Lumsdon, S. O., Kaler, E. W. and Velev. O. D., Two-dimensional crystallization of microspheres by a coplanar AC electric field. *Langmuir* (2004) 20, 2108-2116.

[76] Dussaud, A. D., Khusid, B. and Acrivos, A., Particle segregation in suspensions subject to high-gradient ac electric fields. *J. Appl. Phys.* (2000) 88, 5463-5473.

[77] Cui, L., Holmes, D. and Morgan, H., The dielectrophoretic levitation and separation of latex beads in microchips. *Electrophoresis* (2001) 22, 3893-3901.

[78] Rodriguez, N. F. and Markx, G. H., Improved levitation and trapping of particles by negative dielectrophoresis by the addition of amphoteric molecules. *J. Phys. D: Appl. Phys.* (2004) 37, 353-361.

[79] Kumar, A., Qiu, Z. and Acrivos, A., Combined negative dielectrophoresis and phase separation in nondilute suspensions subject to a high-gradient ac electric field. *Phys. Rev. E* (2004) 69, 021402.

[80] Deval, J., Tabeling, P. and Ho, C-M., A dielectrophoretic chaotic mixer. *Proc. IEEE MEMS 2002, Micro Electro Mechanical Systems*, Las Vegas, USA (2002) 36-39.

[81] Velev, O. D. and Kaler, E. W., In situ assembly of colloidal particles into miniaturized biosensors. *Langmuir* (1999) 15, 3693-3698.

[82] Medoro, G., Manaresi, N., Leonardi, A., Altomare, L., Tartagni, M. and Guerrieri, R., A lab-on-a-chip for cell detection and manipulation. *IEEE Sensors J.* (2003) 3, 317-325.

[83] Gray, D. S., Tan, J. L., Voldman, J. and Chen, C. S., Dielectrophoretic registration of living cells to a microelectrode array. *Biosens. Bioelectron.* (2004) 19, 771-780.

[84] Li, Y. and Kaler, K. V., Dielectrophoretic fluidic cell fractionation system *Anal. Chim. Acta* (2004) 507, 151-161.

[85] Chou, C. and Zenhausern, F., Electrodeless dielectrophoresis for micro total analysis systems. *IEEE Eng. Med. Biol. Mag.* (2003) 22, 62-67.

[86] Wang, X., Huang, Y., Burt, J. P. H., Markx, G. H. and Pethig, R., Selective dielectrophoretic confinement of bioparticles in potential energy wells. *J. Phys. D; Appl. Phys.* (1993) 26, 1278-1285.

[87] Morgan, H., Hughes, M. P. and Green, N. G., Separation of submicron bioparticles by dielectrophoresis. *Biophys. J.* (1999) 77, 516-525.

[88] Hunter, R. J., *Foundations of Colloid Science*, Oxford University Press, UK, 2001.

[89] Adamson, A. W., *Physical Chemistry of Surfaces*, Wiley, New York, 1990.

[90] Israelachvili, J. N., *Intermolecular and Surface Forces*, Academic Press, San Diego, 1992.

[91] Harrison, D. J., Manz, A., Fan, Z., Lüdi, H. and Widmer, H. M., Capillary electrophoresis and sample injection systems integrated on a planar glass chip. *Anal. Chem.* (1992) 64, 1926-1932.

[92] Schasfoort, R. B. M., Schlautmann, S., Hendrikse, J. and van den Berg, A., Field-effect flow control for microfabricated fluidic networks. *Science* (1999) 286, 942-945.

[93] Chen, C. and Santiago, J. G., A planar electroosmotic micropump. *J. Microelectromech. Systs.* (2002) 11, 672-683.

[94] Gitlin, I., Stroock, A. D. and Whitesides, G. M., Pumping based on transverse electrokinetic effects. *Appl. Phys. Lett.* (2003) 83, 1486-1488.

[95] Seller, K., Fan, Z. H., Flurl, K. and Harrison, D. J., Electroosmotic pumping and Valveless control of fluid flow within a manifold of capillaries on a glass chip. *Anal.*

Chem. (1994) 66, 3485-3491.

[96] Besselink, G. A. J., Vulto, P., Lammertink, R. G. H., Schlautmann, S., van den Berg, A., Olthuis, W., Engbers, G. H. M. and Schasfoort, R. B. M., Electroosmotic guiding of sample flows in a laminar flow chamber. *Electrophoresis* (2004) 25, 3705-3711.

[97] Stroock, A .D., Weck, M., Chiu, D. T., Huck, W. T. S., Kenis, P. J. A., Ismagilov, R. F. and Whitesides, G. M., Patterning electroosmotic flow with patterned surface charge. *Phys. Rev. Lett.* (2000) 84, 3314-3317.

[98] Erickson, D. and Li, D., Influence of surface heterogeneity on electrokinetically driven microfluidic mixing. *Langmuir* (2002) 18, 1883-1892.

[99] Tian, F., Li, B. and Kwok, D. Y., Tradeoff between mixing and transport for electroosmotic flow in heterogeneous microchannels with nonuniform surface potentials. *Langmuir* (2005) 21, 1126-1131.

[100] Bhatt, K. H., Grego, S. and Velev, O. D., An AC electrokinetic technique for collection and concentration of particles and cells on patterned electrodes. *Langmuir* (2005) 21, 6603-6612.

[101] Green, N. G., Ramos, A., Gonzalez, A., Morgan, H. and Castellanos, A., Fluid flow induced by nonuniform AC electric fields in electrolytes on microelectrodes. I. Experimental measurements. *Phys. Rev. E* (2000) 61, 4011-4018.

[102] Wong, P. K., Chen, C-Y., Wang, T-H. and Ho, C-M., An AC electroosmotic processor for biomolecules. *Proc. IEEE Solid State Sens. Actuators Microsys., Boston, USA* (2003) 20-23.

[103] Ajdari, A., Pumping liquids using asymmetric electrode arrays. *Phys. Rev. E* (2000) 61, R45-R48.

[104] Mpholo, M., Smith, C. G. and Brown, A. B. D., Low voltage plug flow pumping using anisotropic electrode arrays. *Sens. Actuators B* (2003) 92, 262-268.

[105] Velev, O. D., Prevo, B. G. and Bhatt, K. H., On-chip manipulation of free droplets. *Nature* (2003) 426, 515-516.

[106] Günther, A. and Jensen, K. F., Multiphase microfluidics from flow characteristics to chemical and materials synthesis. *Lab Chip* (2006) 6, 1487-1503.

[107] Joanicot, M. and Ajdari, A., Droplet control for microfluidics. *Science* (2005) 309, 887-888.

[108] Atencia, J. and Beebe, D., Controlled microfluidic interfaces. *Nature* (2005) 437, 648-655.

[109] The, S-Y., Lin, R., Hung, L-H. and Lee, A. P., Droplet microfluidics. *Lab Chip* (2008) 8, 198-220.

[110] Thorsen, T., Roberts, R. W., Arnold, F. H. and Quake, S. R., Dynamic Pattern Formation in a Vesicle-Generating Microfluidic Device. *Phys. Rev. Lett.* (2001) 86, 4163-4166.

[111] Garstecki, P., Fuerstman, M. J., Stone, H. A. and Whitesides, G. M., Formation of droplets and bubbles in a microfluidic T-junction - scaling and mechanism of break-up. *Lab Chip* (2006) 6, 437-446.

[112] Nisisako, T., Torii, T. and Higuchi, T., Droplet formation in a microchannel network. *Lab Chip* (2002) 2, 24-26.

[113] Priest, C., Herminghaus, S. and Seemann, R., Generation of monodisperse gel emulsions in a microfluidic device. *Appl. Phys. Lett.* (2006) 88, 024106.

[114] Anna, S. L., Bontoux, N. and Stone, H. A., Formation of dispersions using ‘‘flow focusing’’ in microchannels. *Appl. Phys. Lett.* (2003) 82, 364-366.

[115] Anna, S. L. and Mayer, H. C., Microscale tipstreaming in a microfluidic flow focusing device. *Phys. Fluids* (2006) 18, 121512.

[116] Yobas, L., Martens, S., Ong, W-L. and Ranganathan, N., High-performance flow focusing geometry for spontaneous generation of monodispersed droplets. *Lab Chip* (2006) 6, 1073-1079.

[117] Nisisako, T., Torii, T., Takajashi, T. and Takizawa, Y., Synthesis of monodisperse bicolored Janus particles with electrical anisotropy using a microfluidic co-flow system. *Adv. Mater.* (2006) 18, 1152-1156.

[118] Song. H., Tice, J. D. and Ismagilov, R. F., A microfluidic system for controlling reaction networks in time. *Angew. Chem. Int. Ed.* (2003) 42, 767-772.

[119] Link, D. R., Anna, S. L., Weitz, D. A. and Stone, H. A., Geometrically mediated break up of drops in microfluidic devices. *Phys. Rev. Lett.* (2004) 92, 054503.

[120] Tan, Y-C., Fisher, J. S., Lee, A. I., Cristini, V. and Lee, A. P., Design of microfluidic channel geometries for the control of droplet volume chemical concentration and sorting. *Lab Chip* (2004) 4, 292-298.

[121] Ahn, K., Agresti, J., Chong, H., Marquez, M. and Weitz, D. A., Electrocoalescence of drops synchronized by size-dependent flow in microfluidic channels. *Appl. Phys. Lett.* (2006) 88, 264105.

[122] Garstecki, P., Fischbach, M. A. and Whitesides, G. M., Design for mixing using bubbles in branched microfluidic channels. *Appl. Phys. Lett.* (2005) 86, 244108.

[123] Cristini, V. and Tan, Y-C., Theory and numerical simulation of droplet dynamics in complex flows – a review. *Lab Chip* (2004) 4, 257-264.

[124] Bringer, M. R., Gerdts, C. J., Song, H., Tice, J. D. and Ismagilov, R. F., Microfluidic systems for chaemical kinetics that rely on chaotic mixing in droplets. *Phil. Trans. R. Soc. Lond. A* (2004) 362, 1087-1104.

[125] Christopher, G. F. and Anna, S. L., Microfluidic methods for generating continuous droplet streams. *J. Phys. D: Appl. Phys.* (2007) 40, R319-R336.

[126] Khan, S. A., Günther, A., Schmidt, M. A. and Jensen, K. F., Microfluidic synthesis of colloidal silica. *Langmuir* (2004) 20, 8604-8611.

[127] Günther, A., Khan, S. A., Thalmann, M., Trachsel, F. and Jensen, K. F., Transport and reaction in microscale segmented gas-liquid flow. *Lab Chip* (2004) 4, 278-286.

[128] Yen, B. K. H., Günther, A., Schmidt, M. A., Jensen, K. F. and Bawendi, M. G., A microfabricated gas-liquid segmented flow reactor for high temperature synthesis: The case of CdSe quantum dots. *Angew. Chem. Int. Ed.* (2005) 44, 5447-5451.

[129] Seo, M., Nie, Z., Xu, S., Mok, M., Lewis, P. C., Graham, R. and Kumacheva, E., Continuous microfluidic reactors for polymer particles. *Langmuir* (2005) 21, 11614-11622.

[130] Dendukuri, D., Tsoi, K., Hatton, T, A, and Doyle, P. S., Controlled synthesis of nonspherical microparticles using microfluidics. *Langmuir* (2005) 21, 2113-2116.

[131] Nie, Z., Li, W., Seo, M., Xu, S. and Kumacheva, E., Janus and ternary particles generated by microfluidic synthesis: Design, synthesis, and self-assembly. *J. Am. Chem. Soc.* (2006) 128, 9408-9412.

[132] Carroll, N. J., Rathod, S. B., Derbins, E., Mendez, S., Weitz, D. A. and Petsev, D. N., Droplet-based microfluidics for emulsion and solvent evaporation synthesis of monodisperse mesoporous silica microspheres. *Langmuir* (2008) 24, 658-661.

[133] Utada, A. S., Lorenceau, E., Link, D. R., Kaplan, P.D., Stone, H. A. and Weitz, D.

A., Monodisperse double emulsions generated from a microcapillary device. *Science* (2005) 308, 537-541.

[134] Kim, J-W., Utada, A. S., Fernández-Nieves, A., Hu, Z. and Weitz, D. A., Fabrication of monodisperse gel shells and functional microgels in microfluidic devices. *Angew. Chem. Int. Ed.* (2007) 46, 1819-1822.

[135] Lee, D. and Weitz, D. A., Double emulsion-templated nanoparticle colloidosomes with selective permeability. *Adv. Mater.* (2008) 20, 3498-3503.

[136] Chu, L-Y., Utada, A. S., Shah, R. K., Kim, J-W. and Weitz, D. A., Controllable monodisperse multiple emulsions. *Angew. Chem. Int. Ed.* (2007) 46, 8970-8974.

[137] Zheng, B., Roach, S. and Ismagilov, R. F., Screening of protein crystallization conditions on a microfluidic chip using nanoliter-size droplets. *J. Am. Chem. Soc.* (2003) 125, 11170-11171.

[138] Zheng, B., Tice, J. D., Roach, L. S. and Ismagilov, R. F., A droplet-based, composite PDMS/Glass capillary microfluidic system for evaluating protein crystallization conditions by microbatch and vapor-diffusion methods with on-chip X-ray diffusion. *Angew. Chem. Int. Ed.* (2004) 43, 2508-2511.

[139] Fair, R. B., Digital microfluidics:_is a true lab-on-a-chip possible ?. *Microfluid Nanofluid* (2007) 3, 245-281.

[140] Pollack, M. G., Shenderov, A. D. and Fair, R. B., Electrowetting-based actuation of droplets for integrated microfluidics. *Lab Chip* (2002) 2, 96-101.

[141] Pollack, M. G., Fair, R. B. and Shenderov, A. D., Electrowetting-based actuation of liquid droplets for microfluidic applications. *Appl. Phys. Lett.* (2000) 77, 1725-1726.

[142] Cho, S. K., Moon, H. and Kim, C-J., Creating, transporting, cutting, and merging liquid droplets by electrowetting-based actuation for digital microfluidic circuits. *J. Microelectromech. Syst.* (2003) 12, 70-80.

[143] Yi, U-C. and Kim, C-J., Characterization of electrowetting actuation on addressable single-side coplanar electrodes. *J. Micromech. Microeng.* (2006) 16, 2053-2059.

[144] Paik, P., Pamula, V. K., Pollack, M. G. and Fair, R. B., Electrowetting-based droplet mixers for microfluidic systems. *Lab Chip* (2003) 3, 28-33.

[145] Paik, P., Pamula, V. K. and Fair, R. B., Rapid droplet mixers for digital microfluidic systems. *Lab Chip* (2003) 3, 253-259.

[146] Jones, T. B., Gunji, M., Washizu, M. and Feldman, M. J., Dielectrophoretic liquid actuation and nanodroplet formation. *J. Appl. Phys.* (2001) 89, 1441-1448.

[147] Wang, K-L., Jones, T. B. and Raisanen, A., Dynamic control of DEP actuation and droplet dispensing. *J. Micromech. Microeng.* (2007) 17, 76-80.

[148] Ahmed, R. and Jones, T. B., Optimized liquid DEP droplet dispensing. *J. Micromech. Microeng.* (2007) 17, 1052-1058.

[149] Millman, J. R., Bhatt, K. H., Prevo, B. G. and Velev, O. D., Anisotropic particle synthesis in dielectrophoretically controlled microdroplet reactors. *Nat. Mater.* (2005) 4, 98-102.

[150] Schwartz, J. A., Vykoukal, J. V. and Gascoyne, P. R. C., Droplet-based chemistry on a programmable microchip. *Lab Chip* (2004) 4, 11-17.

[151] Gascoyne, P. R. C., Vykoukal, J. V., Schwartz, J. A., Anderson, T. J., Vykoukal, D. M., Current, K. W., McConaghy, C., Becker, F. F. and Andrews, C., Dielectrophoresis based programmable fluidic processors. *Lab Chip* (2004) 4, 299-309.

[152] Cho, S. K. and Kim, C-J., Particle separation and concentration control for digital microfluidic systems. *Proc. IEEE MEMS, Kyoto, Japan* (2003) 686-689.

[153] Srinivasan, V., Pamula, V. K. and Fair, R. B., An integrated digital microfluidic lab-on-a-chip for clinical diagnostics on human physiological fluids. *Lab Chip* (2004) 4, 310-315.

[154] Purcell, E. M., Life at low Reynolds number. *Am. J. Phys.* (1977) 45, 3-11.

[155] Shapere, A. and Wilczek, F., Self-propulsion at low Reynolds number. *Phys. Rev. Lett.* (1987) 58, 2051-2054.

[156] Becker, L. E., Koehler, S. A. and Stone, H. A., On self-propulsion of micro-machines at low Reynolds number: Purcell's three-link swimmer. *J. Fluid Mech.* (2003) 490, 15-35.

[157] Requicha, A. A. G., Nanorobots, NEMS, and Nanoassembly. *Proc. IEEE* (2003) 91, 1922-1933.

[158] Evans, D. F. and Wennerström, H., *The colloidal domain – Where physics, chemistry, biology, and technology meet*, Wiley-VCH, New York, 1999.

[159] Paxton, W. F., Sundararajan, S. Mallouk, T. E. and Sen, A., Chemical locomotion. *Angew. Chem. Int. Ed.* (2006) 45, 5420-5429.

[160] Dusenbery, D. B., Minimum size limit for useful locomotion by free-swimming microbes. *Proc. Natl. Acad. Sci. USA* (1997) 94, 10949-10954.

[161] Mavroidis, C., Dubey, A. and Yarmush, M. L., Molecular machines. *Annu. Rev. Biomed. Eng.* (2004) 6, 363-395.

[162] Schliwa, M. and Woehlke, G., Molecular motors. *Nature* (2003) 442, 759-765.

[163] van den Heuvel, M. G. L. and Dekker, C., Motor proteins at work for nanotechnology. *Science* (2007) 317, 333-336.

[164] Berg, H. C. and Anderson, R. A., Bacteria swim by rotating their flagellar filaments. *Nature* (1973) 245, 380-382.

[165] Blair, D. F. and Berg, H. C., Restoration of torque in defective flagellar motors. *Science* (1988) 242, 1678-1681.

[166] Soong, R. K., Bachand, G. D., Neves, H. P., Olkhovets, A. G., Craighead, H. G. and Montemagno, C. D., Powering an inorganic nanodevice with a biomolecular motor. *Science* (2000) 290, 1555-1558.

[167] Hess, H., Matzke, C. M., Doot, R. K., Clemmens, J., Bachand, G. D., Bunker, B. C. and Vogel, V., Molecular shuttles operating undercover a new photolithographic approach for the fabrication of structured surfaces supporting directed motility. *Nano Lett.* (2003) 3, 1651-1655.

[168] Takeuchi, S., DiLuzio, W. R., Weibel, D. B. and Whitesides, G. M., Controlling the shape of filamentous cells of *Escherichia coli*. *Nano Lett.* (2005) 5, 1819-1823.

[169] Weibel, D. B., Garstecki, P., Ryan, D., DiLuzio, W. R., Mayer, M., Seto, J. E. and Whitesides, G. M., Microoxen: Microorganisms to move microscale loads. *Proc. Natl. Acad. Sci. USA* (2005) 102, 11963-11967.

[170] Hiratsuka, Y., Miyata, M., Tada, T. and Uyeda, T. Q. P., Microrotary motor powered by bacteria. *Proc. Natl. Acad. Sci. USA* (2006) 103, 13618-13623.

[171] Ozin, G. A., Manners, I., Fournier-Bidoz, S. and Arsenault, A., Dream nanomachnies. *Adv. Mater.* (2005) 17, 3011-3018.

[172] Brouwer, A. M., Frochot, C., Gatti, F. G., Leigh, D. A., Mottier, L., Paolucci, F.,

Roffia, S. and Wurpel, G. W. H., Photoinduction of fast, reversible translational motion in a hydrogen-bonded molecular shuttle. *Science* (2001) 291, 2124-2128.

[173] Badjic, J. D., Balzani, V., Credi, A. Silvi, S. and Stoddart, J. F., A molecular elevator, *Science* (2004) 303, 1845-1849.

[174] Koumura, N., Zijlstra, R. W. J., van Delden, R. A., Harada, N. and Feringa, B. L., Light-driven monodirectional molecular rotor. *Nature* (1999) 401, 152-155.

[175] Vicario, J., Katsonis, N., Ramon, B. S., Bastiaansen, C. W. M., Broer, D. J. and Feringa, B. L., Nanomotor rotates microscale objects. *Nature* (2006) 440, 163.

[176] Ismagilov, R. F., Schwartz, A., Bowden, N. and Whitesides, G. M., Autonomous movement and self-assembly. *Angew. Chem. Int. Ed.* (2002) 41, 652-654.

[177] Paxton, W. F., Kistler, K. C., Olmeda, C. C., Sen, A., St. Angelo, S. K., Cao, Y., Malouk, T. E., Lammert, P. E. and Crespi, V. H., Catalytic nanomotors: autonomous movement of striped nanorods. *J. Am. Chem. Soc.* (2004) 126, 13424-13431.

[178] Dhar. P., Fischer, Th. M., Wang, Y., Mallouk, T. E., Paxton, W. F. and Sen, A., Autonomously moving nanorods at a viscous interface. *Nano Lett.* (2006) 6, 66-72.

[179] Paxton, W. F., Baker, P. T., Kline, T. R., Wang, Y., Mallouk, T. E. and Sen, A., Catalytically induced electrokinetics for motors and micropumps. *J. Am. Chem. Soc.* (2006) 128, 14881-14888.

[180] Sundarajan, S., Lammert, P. E., Zudans, A. W., Crespi, V. H. and Sen, A., Catalytic motors for transport of colloidal cargo. *Nano Lett.* (2008) 8, 1271-1276.

[181] Fournier-Bidoz, S., Arsenault, A. C., Manners, I. and Ozin, G. A., Synthetic self-propelled nanorotors. *Chem. Commun.* (2005) 441-443.

[182] Catchmark, J. M., Sundarajan, S. and Sen, A., Directed rotational motion of microscale objects using interfacial tension gradients continually generated via catalytic reactions. *Small* (2005) 1, 202-206.

[183] Vicario, J., Eelkema, R., Browne, W. R., Meetsma, A., La Crios, R. M. and Feringa, B. L., Catalytic molecular motors: fuelling autonomous movement by a surface bound synthetic manganese catalase. *Chem. Commun.* (2005) 3936-3938.

[184] Mano, N. and Heller, A., Bioelectrochemical propulsion, *J. Am. Chem. Soc.* (2005) 127, 11574-11575.

[185] Nakata, S., Iguchi, Y., Ose, S., Kuboyama, M., Ishii, T. and Yoshikawa, K., Self-rotation of a camphor scraping on water new insight into the old problem. *Langmuir* (1997) 13, 4454-4458.

[186] Nakata, S. and Hayashima, Y., Spontaneous motion of a solid is sensitive to the pH of an aqueous phase. *Langmuir* (1999) 15, 1872-1875.

[187] Kohira, M. I., Hayashima, Y., Nagayama, M. and Nakata, S., Synchronized self-motion of two camphor boats. *Langmuir* (2001) 17, 7124-7129.

[188] Gong, J. P., Matsumoto, S., Uchida, M., Isogai, N. and Osada, Y., Motion of polymer gels by spreading organic fluid on water. *J. Phys. Chem.* (1996) 100, 11092-11097.

[189] Mitsumata, T., Ikeda, K., Gong, J. P. and Ossada, Y., Solvent-driven chemical motor. *Appl. Phys. Lett.* (1998) 73, 2366-2368.

[190] Mitsumata, T., Ikeda, K., Gong, J. P. and Ossada, Y., Controlled motion of solvent-driven gel motor and its application as a generator. *Langmuir* (2000) 16, 307-312.

[191] Osada, Y. and Gong, J. P., Soft and wet materials: Polymer gels. *Adv. Mater.* (1998) 10, 827-837.

[192] Berridge, M. J., Bootman, M. D. and Lipp, P., Calcium a life and death signal. *Nature* (1998) 395, 645-648.

[193] Maier, J., Nanoionics: Ion transport and electrochemical storage in confined systems. *Nat. Mater.* (2005) 4, 805-815.

[194] Siwy, Z. S., Powell, M. R., Petrov, A., Kalman, E., Trautmann, C. and Eisenberg, R. S., Cacium induced voltage gating in single conical nanopores. *Nano Lett.* (2006) 8, 1729-1734.

[195] Lovreček, B., Despić, A. and Bockris, J. O'M., Electrolytic junctions with rectifying properties. *J. Phys. Chem.* (1959) 63, 750-751.

[196] Hegedüs, L., Wittmann, M., Kirschner, N. and Noszticzius, Z., Reaction, diffusion, electric conduction and determination of fixed ions in a hydrogel. *Progr. Colloid Polym. Sci.* (1996) 102, 101-109.

[197] Hegedüs, L., Kirschner, N., Wittmann, M. and Noszticzius, Z., Electrolyte transistors: Ionic reaction-diffusion systems with amplifying properties. *J. Phys. Chem.* (1998) 102, 6491-6497.

[198] Lindner, J., Šnita, D. and Marek, M., Modelling of ionic systems with a narrow acid–base boundary. *Phys. Chem. Chem. Phys.* (2002) 4, 1348-1354.

[199] Harrell, C. C., Kohli, P., Siwy, Z. and Martin, C. R., DNA-nanotube artificial ion channels. *J. Am. Chem. Soc.* (2004) 126, 15646-15647.

[200] Siwy, Z. and Fuliński, A., Fabrication of a synthetic nanopore ion pump. *Phys. Rev. Lett.* (2002) 89, 198103.

[201] Siwy, Z., Heins, E., Harrell, C. C., Kohli, P. and Martin, C. R., Conical-nanotube ion-current rectifiers: The role of surface charge. *J. Am. Chem. Soc.* (2004) 126, 10850-10851.

[202] Siwy, Z., Ion-current rectification in nanopores and nanotubes with broken symmetry. *Adv. Funct. Mater.* (2006) 16, 735-746.

[203] Gracheva, M. E., Vidal, J. and Leburton, J-P., p-n Semiconductor membrane for electrically tunable ion current rectification and filtering. *Nano Lett.* (2007) 7, 1717-1722.

[204] Umehara, S., Pourmand, N., Webb, C. D., Davis, R. W., Yasuda, K. and Karhanek, M., Current rectification with Poly-L-Lysine-coated quartz nanopipettes. *Nano Lett.* (2006) 6, 2486-2492.

[205] Daiguji, H., Yang, P. and Majumdar, A., Ion transport in nanofluidic channels. *Nano Lett.* (2004) 4, 137-142.

[206] Karnik, R., Fan, R., Yue, M., Li, D., Yang, P. and Majumdar, A., Electrostatic control of ions and molecules in nanofluidic transistors. *Nano Lett.* (2005) 5, 943-948.

[207] Cheng, L-J. and Guo, L. J., Rectified ion transport through concentration gradient in silica nanochannels. *Nano Lett.* (2007) 7, 3165-3171.

[208] Höltzel, A. and Tallarek, U., Ionic conductance of nanopores in microscale analysis systems: Where microfluidics meets nanofluidics. *J. Sep. Sci.* (2007) 30, 1398-1419.

[209] Daiguji, H., Oka, Y. and Shirono, K., Nanofluidic diode and bipolar transistor. *Nano Lett.* (2005) 5, 2274-2280.

[210] Karnik, R., Duan, C., Castelina, K., Daiguji, H. and Mrjumdar, A., Rectification of ionic current in a nanofluidic diode. *Nano Lett.* (2007) 7, 547-551.

[211] Vlassiouk, I. and Siwy, Z. S., Nanofluidic diode. *Nano Lett.* (2007) 7, 552-556.

[212] Kalman, E. B., Vlassiouk, I. and Siwy, Z. S., Nanofluidic bipolar transistors. *Adv. Mater.* (2008) 20, 293-297.

[213] Fan, R., Yue, M., Karnik, R., Majumdar, A. and Yang. P., Polarity switching and transient responses in single nanotube nanofluidic transistors. *Phys. Rev. Lett.* (2005) 95, 086607.

[214] Karnik, R., Castelino, K. and Majumdar, A., Field-effect control of protein transport in a nanofluidic transistor circuit. *Appl. Phys. Lett.* (2006) 88, 123114.

[215] Fan, R., Huh, S., Yan, R., Arnold, J. and Yang, P., Gated proton transport in aligned mesoporous silica films. *Nat. Mater.* (2008) 7, 303-307.

[216] Rastogi, V. and Velev, O. D., Development and evaluation of realistic microbioassays in freely suspended droplets on a chip. *Biomicrofluidics* (2007) 1, 014107.

Chapter 2

Evaporation-Induced Particle Microseparations inside Droplets Floating on a Chip*

* Partially based on Chang and Velev, *Langmuir*, 2006, **22**, 1459-1468.

2.1. Introduction

Droplet-based microfluidic systems have emerged as a promising technology for solving some of the drawbacks of microchannel-based microfluidic systems, such as channel clogging with suspended particles or biomolecules, poor mixing due to the intrinsically low Reynolds number of microfluidic flows, and the difficulty of particle separation to analyze complex and heterogeneous samples.[1-10] We developed a dielectrophoretic liquid-liquid chip system for capturing and manipulating micro-sized droplets freely suspended on the surface of a dense perfluorinated hydrocarbon oil (F-oil).[11] The droplets were transported using an alternating electric field applied by electrode arrays situated below the F-oil.

The droplets floating on these electronically controlled dielectrophoretic liquid-liquid chips can serve as "micro-reactors" for the assembly of novel supraparticles from nano- and microparticles during the process of droplet evaporation.[12] We observed that during the assembly of supraparticles inside evaporating droplets the particles contained inside were rapidly separated in the droplet's top region exposed to the ambient air, instead of collecting on the bottom due to sedimentation. This new phenomena could have importance in diverse processes for on-chip materials and particle fabrication, chemical miscrosynthesis, microbiassays and microsensing. Here, we investigate the processes taking place in single floating droplets and the mechanism of evaporation-driven vertical redistribution of the microspheres suspended inside them.

Solvent evaporation in liquid films and droplets has been used in convective assembly of micro- and nanoparticle coatings in thin evaporating film,[13-15] ring formation of suspended materials by evaporation of sessile droplets on the substrate,[16-19] assembly of colloidal particles on hydrophilic and hydrophobic surfaces,[20,21] DNA stretching,[22] and others. Ball-like supraparticles have been assembled inside evaporating spherical droplets containing microspheres.[23-25] Transport and assembly of the suspended particles driven by solvent evaporation are related to the internal hydrodynamics in drying films and droplets.[12-20,23,25] Hydrodynamic flows driven by solvent evaporation have been investigated in much experimental and theoretical detail in sessile droplets [26-28] and in spherical droplets completely exposed to ambient air.[29-31] To our knowledge, however, detailed studies of

particle transport and separations inside evaporating small droplets floating partially submerged in a denser liquid phase have not been reported. This largely results from the experimental difficulty of carrying observations inside freely floating small droplets. These investigations have now been made easier by our dielectrophoretic microfluidic chips, which allow droplet entrapment and precise positioning.

In general, as a droplet evaporates, a nonuniform temperature distribution is established by heat loss due to phase change from liquid to vapor at the evaporating surface.[28,31,32] These local thermal imbalances create a surface tension gradient at the droplet surface. The dependence of the surface tension (σ) on the temperature imbalance is commonly represented by

$$\sigma = \sigma_r - \left|\frac{d\sigma}{dT}\right|(T - T_r) \tag{2-1}$$

where σ_r is reference surface tension, T_r is reference temperature, and $|d\sigma/dT|$ is surface tension derivative with temperature. For common fluids, the value of $d\sigma/dT$ is negative, so that the surface tension increases with decreasing temperature. As a result of the surface tension gradient, the liquid interface is "pulled" toward the colder regions with higher surface tension. Viscous drag moves the fluid adjacent to the surface, and consequently, surface tension driven Marangoni flow is initiated.[31,33-37] A convective Marangoni flow will be established when the surface tension force due to the externally imposed temperature gradient overcomes the viscous resistive force in the liquid. The strength of the thermal instability, characterized by the ratio of the surface tension force to the viscous resistive force, is estimated by the dimensionless Marangoni number, *Ma*,

$$Ma = \frac{\left|\frac{d\sigma}{dT}\right| \Delta T \, R}{\eta \, \alpha} \tag{2-2}$$

The parameters in this expression are temperature difference ΔT, characteristic length (droplet radius) R, dynamic viscosity η, and thermal diffusivity α. An interfacial tension gradient resulting from a temperature gradient in a droplet will cause convective liquid flow inside a droplet if *Ma* is higher than a critical Marangoni number, Ma_c. The critical

Marangoni numbers for the emergence of fluid convection in a thin liquid film at a fixed temperature of the rigid substrate below the thin film have been reported to be $Ma_c \sim 80$.[34,35] The transition from linear flow to Marangoni convection in horizontally heated liquid layers occurs at $Ma_c \sim 20$.[35,36]

The pattern of Marangoni flows driven by thermal instabilities depends on the aspect ratio (AR) of the fluid container some walls of which may be rigid or slippery.[38,39] The convective flow patterns in a cylindrical container with small aspect ratio have reported.[40-42] At AR ~ 1 these flows are typically in the form of one transverse cell (AR in this system is the ratio of the diameter to the height of the horizontal cylinder). Various concentric cell patterns with different azimuthal and wave modes form at other small ARs due to lateral wall effects. The Marangoni flow patterns in systems where AR >> 1 are organized in large number of hexagonal cells.

An alternative driving force for the convective flow inside droplets, besides the Marangoni effect arising from surface tension, is the buoyancy effect correlated with the liquid density dependence on temperature.[33,38,43-45] The dominant source of convection within the droplet can be estimated by the ratio of the Marangoni number (Ma) to the Rayleigh number (Ra)[19,38]

$$\frac{Ma}{Ra} = \frac{\left|\frac{d\sigma}{dT}\right|}{\rho \beta g R^2} \tag{2-3}$$

where the parameters include liquid density ρ, the liquid thermal expansion coefficient β, the gravitational acceleration g, and droplet radius R. When $Ma/Ra >> 1$ the convective flow inside a droplet is dominantly driven by the surface tension gradient. In small evaporating droplets, the interfacial tension gradient is reported as dominant and the buoyancy convection has usually been neglected.[33,43]

In this report, we first describe the technique and the experimental data obtained for microseparation of particles in the top region of evaporating microdroplets floating on a liquid-liquid chip. The convective flows inside the droplets related to the particle microseparations are visualized with the use of suspended particles. Results from two

dimensional (2D) numerical simulations of the temperature evolution and internal flow profiles are correlated with the experimental results. We illustrate one potential use of the phenomena studied by developing a new microbioassay technique based on droplet microseparations.

2.2. Experimental Section

2.2.1. Materials

Aqueous surfactant-free sulfate-stabilized 4.9 μm polystyrene latex microspheres were purchased from Interfacial Dynamics Corp. (USA). Fluorescent sulfate 1 μm microspheres in water and 2 mM azide solution were purchased from Molecular Probes (USA). The microspheres were centrifuged at 1700 g for 3 min with Marathon micro A centrifuge (Fisher Scientific, USA) and washed with deionized (DI) water obtained from Millipore RiOs 16 reverse osmosis water purification systems (Bedford, USA). The collected microspheres were resuspended in DI water and sonicated (Branson Ultrasonics Corp., USA). Polymer microrods (~23.5 μm average length and 0.60 μm average diameter) were prepared in our laboratory.[46,47] An inert, high density perfluorinated oil, FC-70, was purchased from 3M Corp. (USA).

2.2.2. Experimental Setup

The dielectophoretic liquid-liquid chip was based on two-sided printed circuit board with electrode patches on one side and connecting leads on the other. The electrode arrays were connected by individual electronic switches either to the AC voltage source or to the ground. A FG-7002C Sweep/Function generator (EZ Digital Co. Ltd., Korea) was used as a source of square waves of frequency 800 Hz. The generated signal was amplified to the working voltage of 700 V using Piezo Driver/Amplifier (Model PZD 700, Trek Inc., USA). The fabricated chip board was immersed inside a small Petri dish (Millipore Co., USA) containing 4.5 mL FC-70 oil.

All experiments were performed with single floating droplets entrapped by the electric fields from the energized electrodes below. Water droplets of 750 nL containing the

microspheres were injected onto the F-oil with a ultramicropipette (Eppendorf North America Inc., USA). The set-up allowed for both top-down and side observation of the captured droplets (Fig. 2.1). To investigate the droplet from side view, the chip was placed in a rectangular chamber made from optical quality glass slides to avoid image distortion. A SZ61 0.7-4.5×zoom stereomicroscope (Olympus America Inc., USA) was set for top-down or side observation of the floating droplets by changing the microscope's configuration. Images of droplets were taken with DSC-V1 Cyber-Shot digital camera (Sony, Japan) attached to the microscope. An Olympus BX-61 optical microscope (Olympus America Inc., USA) and high resolution DP70 digital CCD camera (Olympus America Inc., USA) were used for characterizing the droplet geometry and measuring the flow velocity inside the suspended droplet with top-down view. The three-dimensional distribution of the particles in evaporating droplets containing 0.2 wt% of 1 μm fluorescent latex was characterized by confocal microscopy using the FV 300 scanner of the Olympus BX-61 system.

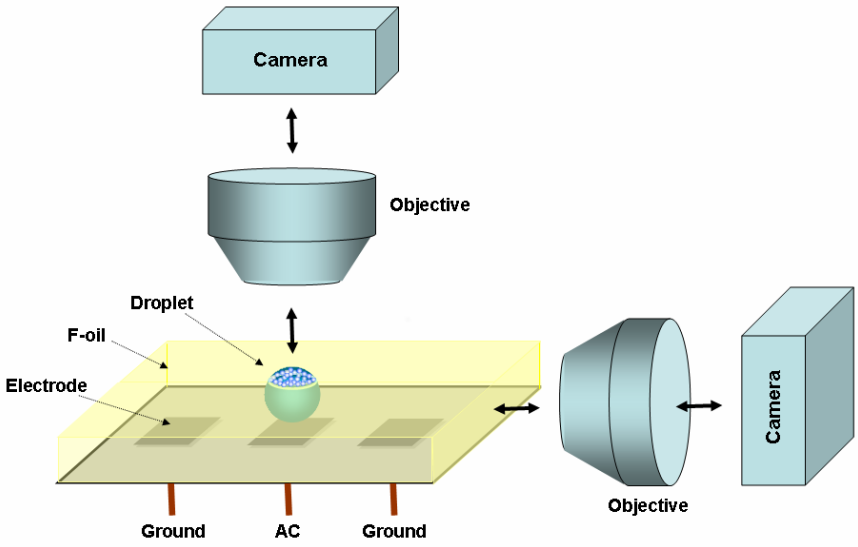

Figure 2.1. Schematic of the experimental setup. A single floating droplet is entrapped by the electric field from the energized electrode below. The particle position within the drying droplet can be monitored with top-down or side microscope equipped with digital camera. Droplet and components are not to scale.

2.2.3. Measurement of Droplet Size and Volume

The water droplet is of intermediate density between F-oil and air and assumes an equilibrium position at the oil-air interface. Most of it was immersed in the oil, while a small portion at the top was exposed to ambient air. The droplet's boundary at the three phase contact line had a smooth profile due to the equal balance between the surface tension at the water-air interface and the sum of the tensions at the other two interfaces ($\sigma_{water\text{-}air}$ = 72 mN/m, $\sigma_{water\text{-}oil}$ = 53 mN/m, $\sigma_{oil\text{-}air}$ = 19 mN/m).[23] The distortion of the droplet shape by gravity can be estimated from the Bond number, *Bo*, which is the ratio of gravitational force to surface tension force

$$Bo = \frac{\Delta\rho\, g\, R^2}{\sigma} \tag{2-4}$$

where $\Delta\rho$ is the density difference between the droplet and the surrounding liquid.[23,32,33,48] For values of $Bo \ll 1$ the effect of gravity can be neglected and the droplet is strictly spherical. 750 nL drops were micropipetted onto the chip and the droplet has initially a ~1.1 mm diameter. Using that value, we estimate a Bond number, $Bo \sim 0.05$. Thus, the droplet maintains a spherical shape unperturbed by gravity during drying; the curvature of the water-air interface is larger than the one of the water-oil interface, but its effect on the distortion of the total droplet shape was also estimated to be small.[49] The droplet diameter (D_d) and water/oil/air contact line diameter (D_c) were continuously measured by monitoring the droplet from the top side with the BX-61 microscope (Fig. 2.2).

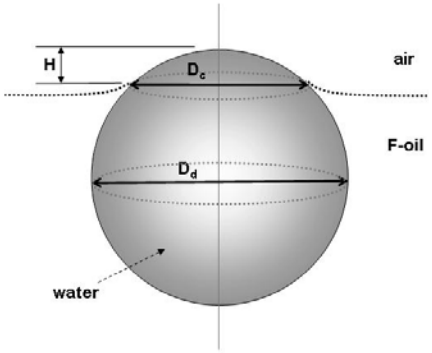

Figure 2.2. Geometry of aqueous droplet floating on F-oil. D_c = diameter of contact line. D_d = diameter of droplet. H = distance from the apex to the three-phase contact line of the droplet.

2.2.4. Measurement of Internal Flow Velocity

We used a microparticle tracer method to measure the internal flow velocity in an evaporating droplet. The velocity of 1 μm tracer particles (0.002 wt % in the water droplet) was measured at the depth of 50 μm and 100 μm from the droplet apex and at the bottom of droplet. The vertical position of the focal plane was adjusted using the scale of the motorized microscope stage. The particle velocity was calculated by measuring the time during which the particles crossed the opposing boundaries of the 112 μm×112 μm square spot imaged by the DP70-BSW software. To prevent the floating droplet from swaying due to air currents in laboratory, the chip was shielded with a transparent enclosure.

2.2.5. Numerical Simulation

The temperature distribution and convective flow profile inside evaporating droplets were simulated with 2D heat and momentum transfer calculations using the FEMLAB Multiphysics finite element method modeling package (COMSOL Inc., USA). Experimentally measured time-dependent values for the diameter (D_d) and vertical position (z) of floating droplet were used in the specification of the geometry of the system. The solution space was divided into two subdomains: evaporating droplet and surrounding F-oil. A conformal triangular mesh was generated by the software for each of the two subdomains. The stationary nonlinear solver package was then used to solve for the temperature distributions and flow profiles for all elements.

2.3. Results and Discussion

2.3.1. Effect of Water Evaporation on Vertical Separation of Microspheres

The dielectrophoretic liquid-liquid chip was open to the ambient air in these experiments to allow evaporation of water from the droplets. The evaporation takes place at the top water-air interface as the droplet floats at the F-oil surface. Sequential images from microscope focused on the top surface of an evaporating water droplet on F-oil are shown in Figure 2.3. Two concurrent effects were seen. First, the drop radius decreased with time due to evaporation. Simultaneously, the particles dispersed in the liquid became accumulated in the

top region as seen by the white-colored cap of concentrated particles growing at the droplet's top section. The continued floatation of the droplet containing microspheres resulted in the latex particles organizing in a colloidal crystal, much like in the supraparticles studied previously.[12]

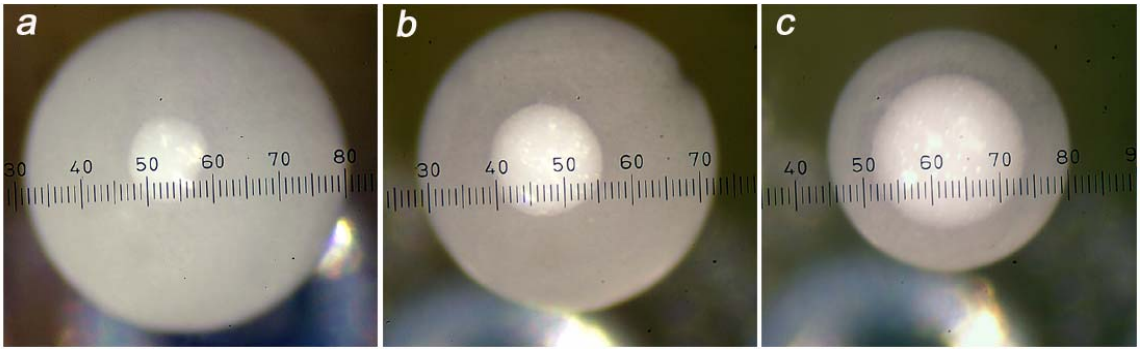

Figure 2.3. Typical micrographs of an evaporating droplet from a top-down perspective. (a) 10 min after floating on the F-oil surface, (b) 20 min, (c) 40 min. The original droplet contains 4.1 wt% of 4.9 μm polystyrene microspheres in DI water. As the water evaporates the particles are collected in the droplet top. The scale in the images is superimposed by the microscope optics (10 div. = 210 μm).

The particle collection process in the top section of evaporating droplet is remarkably rapid. Naturally, as the water evaporates leaving behind the suspended particles some microspheres will be accumulated in the droplet top. However, experimental evidence pointed out that the particles collected in the apex have been drawn out from within the whole droplet volume. The 3D reconstruction of the confocal images in an evaporating droplet containing 0.2 wt% fluorescent latex proves that the majority of the particles in this diluted system have been accumulated in the apex of the droplet, while almost no microspheres remain dispersed in the bulk.

To investigate the particle dynamics inside droplets in the absence of evaporation the liquid-liquid chip was kept in a tightly sealed chamber saturated with water vapor. During this experiment, the droplet volume did not change (data not shown), and no noticeable evaporation occurred. Sedimentation of the latex particles in the bottom region of the droplet was observed, while no particles were collected on the top section (Fig. 2.4). Thus, water

evaporation from the droplet surface is the major factor that overcomes sedimentation and makes the microspheres migrate and re-collect in the top part of the droplets.

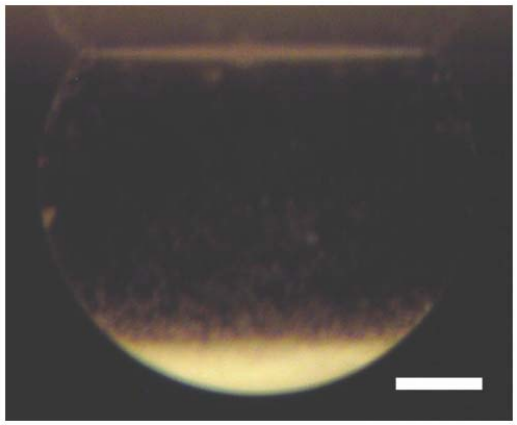

Figure 2.4. Typical image of the contents of non-evaporating water droplet from a side perspective. The droplet contains 0.41 wt% of 4.9 μm polystyrene microspheres in DI water, which have sedimented to the bottom after 45 minutes of experiment. Scale bar = 200 μm.

Finally we proved that evaporation is able to draw to the top even particles sedimented to the bottom of the droplet. In these experiments, after all suspended latex particles had sedimented to the bottom, the sealing cap was removed to allow water evaporation on the top surface of the droplet. The particles' movement was continuously observed while changing the focal plane of the microscope (Fig. 2.5). The latex microspheres that had accumulated near the bottom of the droplet in the absence of evaporation began directionally moving toward the droplet's top region along one side of the interface between the water and F-oil. After some time, latex particles began to be concentrated on the top surface of the droplet, where the water evaporation was taking place. These observations suggest that the strong particle collection process within the evaporating droplet was related to internal liquid flows, which were also caused by the water evaporation. The fluid fluxes inside the droplets were investigated in the next cycle of experiments in order to better characterize the process.

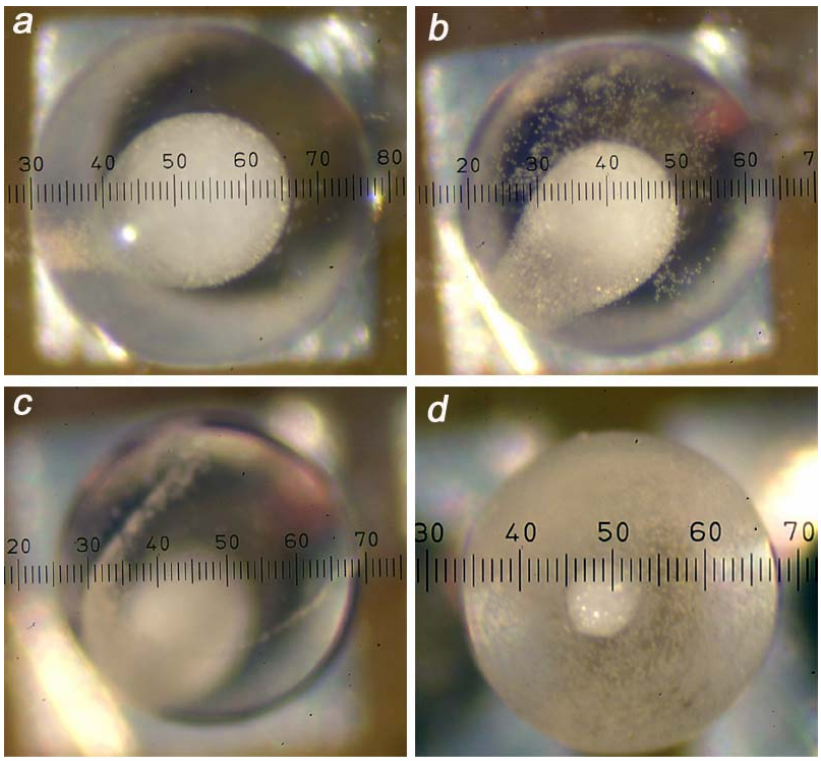

Figure 2.5. Experimental images of particle collection on the top of the droplet when the cap was opened to allow water evaporation. (a) Before the evaporation begins the particles have sedimented on the bottom (microscope focused on the bottom of droplet), (b) 15 min after evaporation the particle slug begins moving up along the droplet surface (microscope focused on the bottom of droplet), (c) 15 min after evaporation (microscope focused on the top of droplet), (d) 60 min after evaporation some particles are collected in the top section (microscope focused on the top of droplet). The original droplet contains 0.41 wt% of 4.9 μm polystyrene microspheres in DI water. The scale in the images is superimposed by the microscope optics (10 div. = 210 μm).

2.3.2. Internal Flow within an Evaporating Droplet

In the experiments described above, we recognized that the water evaporation from the floating droplet played a key role in microseparation of colloid particles into the droplet's top section. The evaporation is coupled with internal flows in the droplets. The goal of the next series of experiments was to identify the flow pattern, recognize the mechanism responsible for the emergence of the flow, and correlate the microseparation of particles to the hydrodynamic flows within the evaporating droplet.

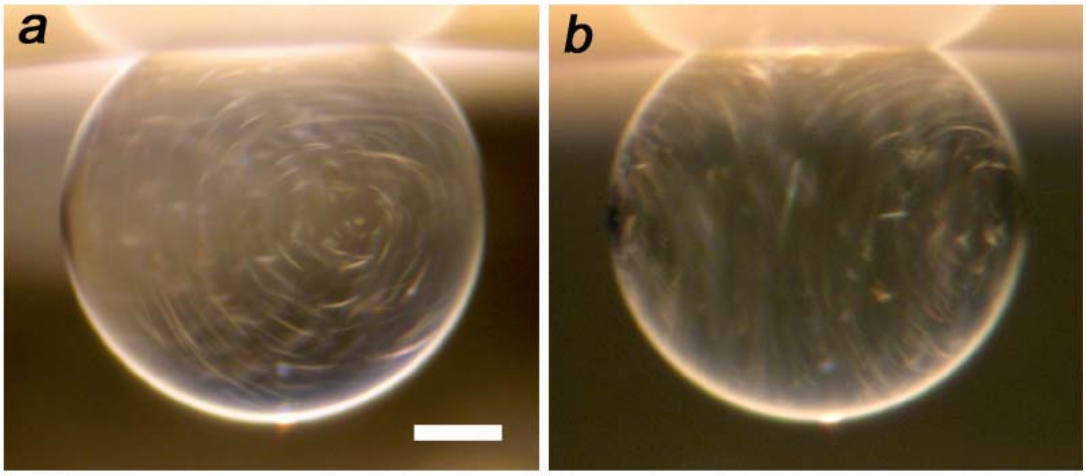

Figure 2.6. Typical experimental images of the internal flow in evaporating water droplet viewed from aside. Image in (b) is taken after 90° change in perspective from (a). The tracers are polymer microrods synthesized by a technique reported by us earlier.[46,47] Camera exposure time was 2 sec. Scale bar = 200 μm.

The internal flow profiles were visualized with rod-like microparticles as a tracer suspended within the evaporating droplet. The advantage of using microrods is that they immediately become aligned so that their long axis point in the direction of the flow.[46] A circular one-directional hydrodynamic flow was observed inside of the evaporating droplets floating on the F-oil surface (Fig. 2.6). The internal fluid circulation continued for periods of tens of minutes to a few hours, however, as the size of droplet decreased because of the water evaporation, the circular flow eventually stopped.

A cycle of experiments were performed in order to characterize in depth the evolution of the internal flow during the droplet evaporation process. 750 nL water droplets containing 1 μm polystyrene latex particles as tracers (0.002 wt%) were floated on the F-oil. The droplet volume change and the velocity of the internal flow were measured over time for two experimental conditions (1) relative humidity (RH) 55% and temperature 23°C, and (2) RH 51% and temperature 28°C. The data for the normalized volumes of the droplets, defined as ratio of the droplet volume at the specific time (V_t) to the initial droplet volume (V_0), are plotted in Figure 2.7. As expected, the droplet volume decreased more rapidly in the second

experimental cycle, due to the higher evaporation rate at lower RH and higher ambient temperature.

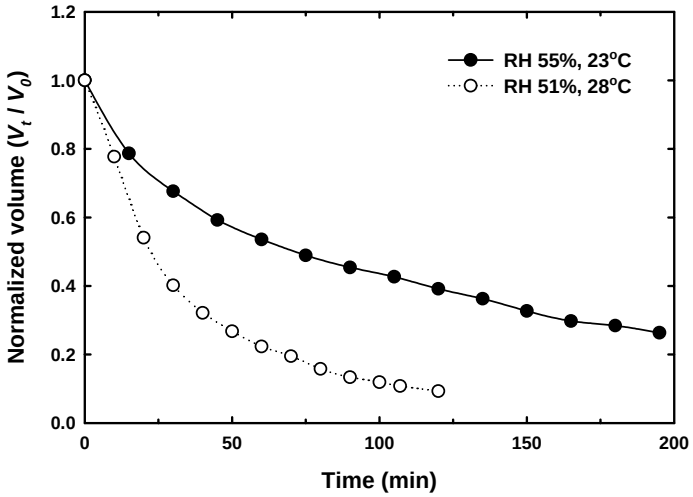

Figure 2.7. Change in the volume of 750 nL droplets with time due to evaporation. V_0 = initial droplet volume. V_t = droplet volume at the specific time.

The flow velocities inside the same droplets were measured with the help of tracer particles. Data for three vertical positions of the measurement plane were collected by adjusting the microscope focus along the center axis of the floating droplet at a distance of 50 μm ($v_{top\text{-}50}$) and 100 μm ($v_{top\text{-}100}$) from the apex of the droplet and near the droplet bottom surface (v_{bottom}). The flow directions at the bottom and at the top sections were opposite due to the circular flow within the droplet. In both experimental conditions, the flow velocity was faster at the bottom of the droplet than at the top region. Within the top region, the velocity near the air-water interface is much slower ($v_{top\text{-}50} < v_{top\text{-}100}$). As the water evaporation progressed, the liquid velocity gradually decreased and abruptly stopped at a smaller droplet size.

The data for all velocity measurements are summarized in Figure 2.8. In the same figure we also plot the time dependence of the evaporation rate ($\dot{m}$) of the droplet

$$\dot{m} = -\frac{dm}{dt} = -\rho_{water}\left(\frac{dV}{dt}\right) \tag{2-5}$$

where m is the mass of the droplet, V is the volume of the droplet, and ρ_{water} is the density of water, and t is the time. The data demonstrate good correlation between the evaporation rate and fluid velocity in the droplet, as the tracer particle velocity also was faster at the high evaporation rate. The fluid flow, however, stopped after the evaporation rate decreased to a certain point.

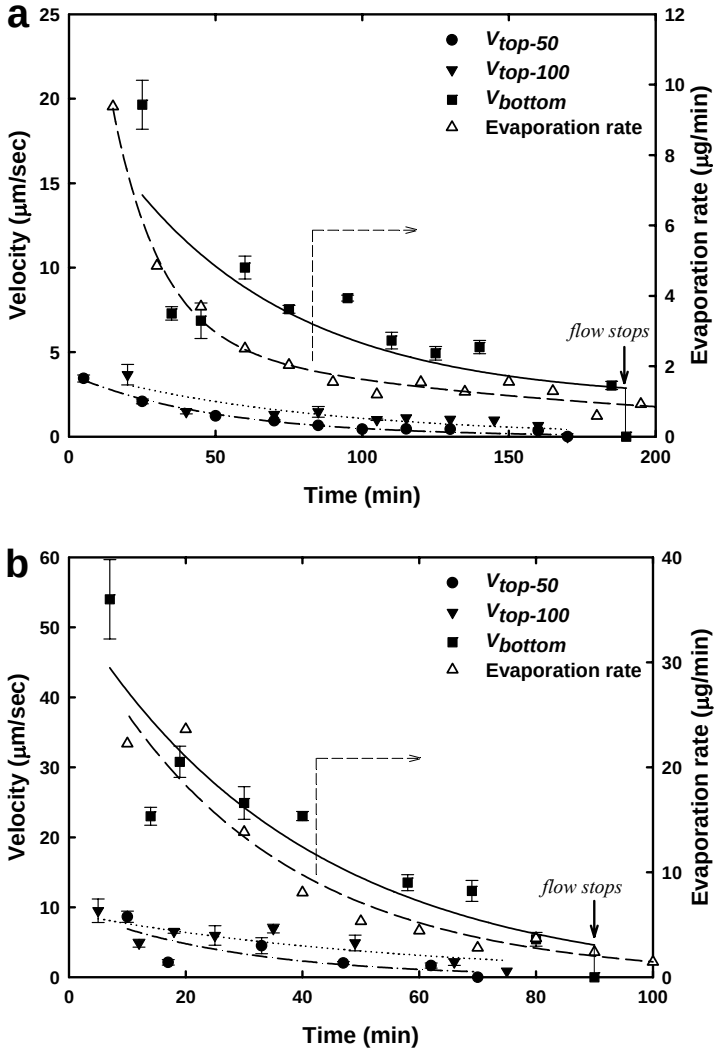

Figure 2.8. Flow velocity and evaporation rate measured with floating droplets. (a) Data at 55% relative humidity and 23°C, (b) Data at 51% relative humidity and 28°C. v_{top-50} = velocity at 50 μm down from the apex of droplet. $v_{top-100}$ = velocity at 100 μm from the apex of droplet. v_{bottom} = velocity at the bottom of droplet. The tracer particles are 0.002 wt% of 1 μm polystyrene microspheres in DI water. The data were fitted to decaying exponential functions.

The combined results of the particle collection, droplet evaporation and particle velocity measurements allow for extending a model for the processes that take place inside the droplets. The experiments point out that the evaporation process is critical both for the collection of particles and for mixing the contents of the droplets. The evaporation of the water at the cap open to the air decreases the local temperature due to the latent heat of vaporization. A temperature gradient is generated within the evaporating droplet due to heat loss at the top. Two possible effects leading to fluid circulation as a result of the vertical temperature gradient can be suggested. The first one originates from the resulting gradient of the interfacial tension. The interfacial tension gradient is engendered as a result of the surface tension dependence on temperature. The interfacial tension would be higher at the colder top surface of the droplet. The surface tension gradient "pulls" the droplet surface towards regions of higher surface tension. Consequently, convective Marangoni flow inside the droplet is created by momentum transfer into the interior of the droplet by the viscous friction.

The second possible reason for the emergence of convective flow within an evaporating droplet, described in Section 2.1, is the dependence of liquid density on the temperature. The relative importance of these two effects, Marangoni flow and density-driven (Rayleigh) flow can be estimated from the ratio of the Marangoni number to Rayleigh number (eq. 2-3). For our drying aqueous droplet, we estimate $Ma/Ra \sim 150$ (the numerical values of the parameters used and their sources are listed in the Supporting Information). As $Ma/Ra >> 1$, we assume that the Marangoni effect is the dominant origin of the convective flow inside our droplets.

The schematic of the mechanism by which the evaporation leads to the vertical microseparation of the suspended particles in our droplet is shown in Figure 2.9. The particles in the vicinity of the top air-water interface are entrained and transported to the surface by the normal flux of water compensating for the evaporation. As mentioned in the introduction, evaporation-driven particle transport and assembly have been found to be the basis of other types of colloidal assembly processes.[13-21] In addition, as a result of the evaporation process, the circular Marangoni-driven flow inside the evaporating droplet

makes possible the continuous mixing and transport of the particles into the top portion of the droplet. Once the particles from the bulk are transported near the region of the water evaporation on the top surface, the internal hydrodynamic replacement flux of water due to the evaporation sucks them into the growing particle crystal in the top. The smaller velocity of the tracer particles at the top of the droplet (Fig. 2.8) can be explained by the compensating evaporation out-flux as well as the no-slip condition at the slug of closely packed particles collected at the surface. The convection inside the evaporating droplet plays a key role in the transport of the suspended particles and thus their collection in the top portion can occur without complete evaporation of all solvent. In the next section we demonstrate that numerical simulations of the heat and momentum transfer processes inside evaporating droplets based on this model are in good agreement with the experimental evidence.

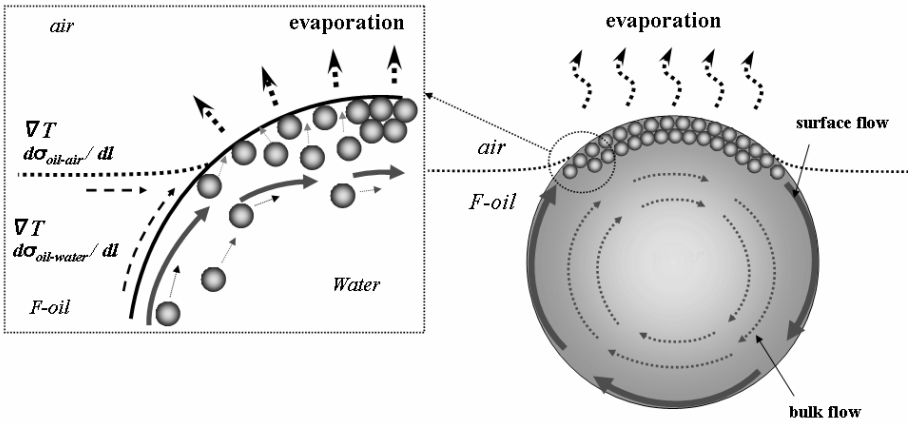

Figure 2.9. Schematics of the proposed mechanism of particle microseparations in evaporating droplets.

2.3.3. Simulation of Temperature Distribution and Flow Profile

The mechanism by which the thermal gradient inside our drying droplet leads to emergence of convective flow was studied in detail by numerical simulations. We developed a procedure for calculating the temperature distribution and the flow profile within an evaporating droplet floating on F-oil. The flow profiles and temperature distributions were calculated in the

vertical cross-section (2D geometry) of water droplet and F-oil layer in a small dish (Fig. 2.10a) by numerical solutions of the continuity, Navier-Stokes, and energy balance equations using FEMLAB software

$$\nabla \cdot \mathbf{V} = 0 \tag{2-6}$$

$$\frac{\partial \mathbf{V}}{\partial t} + \mathbf{V} \cdot \nabla \mathbf{V} + \frac{1}{\rho} \nabla P = \nu \nabla^2 \mathbf{V} \tag{2-7}$$

$$\frac{\partial T}{\partial t} + \mathbf{V} \cdot \nabla T = \alpha \nabla^2 T \tag{2-8}$$

where $\mathbf{V}$ is the velocity vector, P is the pressure, ν is the kinematic viscosity and α is the thermal diffusivity.

The evaporation of the droplet is a nonequilibrium process, since the volume and temperature of the droplet and the evaporation rate keep changing continuously. To simplify the analysis, a quasi-steady approximation was used. The characteristic time of heat diffusion in our droplet (R^2/α) is two orders of magnitude smaller than the characteristic time of droplet surface compression due to evaporation ($R/\dot{R}$, $\dot{R}$ is rate of decrease of droplet's radius). Since the thermal instabilities arise at the initial stage of evaporation, the decrease of droplet diameter can be neglected during a short interval of interest.[30] In addition, it was assumed that the physical properties of the liquid domains, except the surface tension, remain constant during this period. The values of the physical properties of water and F-oil used are listed in Table 2.1.

Table 2.1. Numerical values for the physical properties of the fluids at T=23°C.

Fluid	Density ρ (kg/m^3)	Viscosity η (kg/m s)	Thermal conductivity k (J/m s K)	Thermal diffusivity α (m^2/s)	Thermal expansion β (K^{-1})	Surface tension derivative at air/liquid interface $\lvert d\sigma/dT \rvert$ (N/m K)	Interfacial tension derivative at water/oil interface. $\lvert d\sigma/dT \rvert$ (N/m K)	Latent heat h_l (kJ/kg)
Water	1.0×10^3 (a)	0.94×10^{-3} (a)	0.604 (a)	1.449×10^{-7} (a)	0.236×10^{-3} (a)	~1.5×10^{-4} (c)	~10^{-4} (e)	2442.5 (a)
F-oil FC-70	1.94×10^3 (b)	24×10^{-3} (b)	0.697 (b)	0.342×10^{-7} (b)	0.001 (b)	~10^{-4} (d)		69 (b)

(a) Data from Ref. [54]. (b) Data from the product information data sheet of Fluorinert oil FC-70. (c) Data from Ref. [19]. (d) Data from Ref. [55]. (e) No data found in literature, assumed to be approximately the same as the corresponding number of water/air interface.

The geometry of the system specified is plotted in Figure 2.10a. The boundary conditions used in the simulation are as follows:

Top water/air interface of droplet: The particles suspended in the droplets were collected in a close-packed crystal on the water side of this surface. We also observed in the experiments that the top layer of particles was adsorbed at the interface. Thus we assume that because of the immobilization of the top surface by the closely packed particles the boundary condition can be simplified by assuming that there is no tangential fluid slip. The thermal boundary condition at this surface was a balance between conduction and the sum of natural heat convection and heat outflux due to the evaporative mass transport,

$$\mathbf{V} = 0 \tag{2-9}$$

$$-k_{water}\nabla T \cdot \mathbf{n} = h(T - T_{\infty}) + h_l J_E \tag{2-10}$$

where k_{water} denotes the thermal conductivity of water, h is the natural heat transfer coefficient, h_l is the latent heat of vaporization for water, J_E is evaporation mass flux, and **n** is unit normal vector of the surface. The evaporation mass flux was calculated from the measured evaporation rate (eq. 2-5) divided by the surface area of the top region of the droplet. ($2\pi RH$, where R is the radius of the droplet and H is the distance from the apex to the three-phase contact line of the droplet - Fig. 2.2). The natural heat transfer coefficient, h, is derived from the Nusselt number, $Nu \sim 2$, approximated for natural convection over a spherical droplet,[28,50]

$$h = \frac{2k_{air}}{D_0} \tag{2-11}$$

where k_{air} is the thermal conductivity of the surrounding air, (0.026 J m^{-1} s^{-1}K^{-1} at T = 23°C) and D_0 is the initial diameter of the droplet.

Water/F-oil interface of droplet: The viscous shear stresses balance the surface tension gradient in the tangential direction at the interface. The conductive heat balance across the water-oil interface was used as the thermal boundary condition,

$$\tau_{oil} - \tau_{water} = \nabla \sigma_{oil/water} \cdot \mathbf{t} \tag{2-12}$$

$$-k_{water}\nabla T \cdot \mathbf{n} = -k_{oil}\nabla T \cdot \mathbf{n} \tag{2-13}$$

where τ_{water} is the shear stress at the water surface, τ_{oil} is the shear stress at the oil surface, **t** is unit tangential vector of the surface, and k_{oil} is the thermal conductivity of F-oil. The interfacial tension gradient $\nabla\sigma$ is coupled to the temperature gradient by equation 2-1.

F-oil/air interface: The boundary conditions were a balance of viscous forces with surface shear forces due to the surface tension gradient and the conductive heat balance along the plane surface contacting the ambient air,

$$\tau_{oil} - \tau_{air} = \nabla\sigma_{oil/air} \cdot \mathbf{t} \tag{2-14}$$

$$-k_{oil}\nabla T \cdot \mathbf{n} = -k_{air}\nabla T \cdot \mathbf{n} \tag{2-15}$$

Surface of contact between F-oil and the vessel: The boundary conditions were a no-slip condition for the velocity, **V** = 0**,** and $T = T_{\infty}$, where T_{∞} is the uniform ambient temperature.

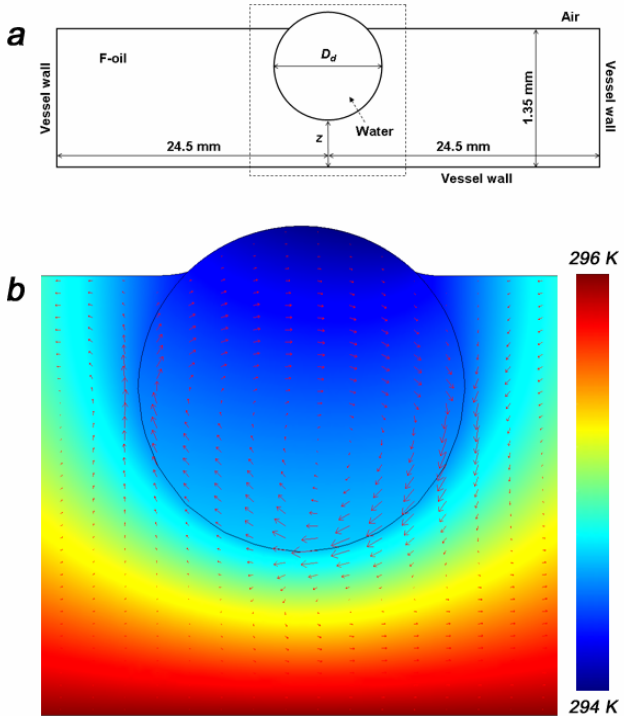

Fingure 2.10. Simulation for the temperature distribution and velocity profile in the drying droplet using FEMLAB. (a) Schematic of the geometry specified (dimensions are not to scale); (b) Computed temperature distribution and velocity profile inside the droplet after 15 min of drying for the system with relative humidity 55% and ambient temperature 23°C. The velocity vector magnitudes are represented by the lengths of the arrows. Colors show the temperature. The results confirm the emergence of circular flow inside the system.

2.3.4. Simulation Results and Correlation with Experimental Data

The computed temperature distribution and velocity field in the evaporating droplet after 15 min floating time at RH 51% and an ambient temperature of 23°C are shown in Figure 2.10b. A vertical temperature gradient is established inside the system due to water evaporation at the top droplet surface. The resulting interfacial tension gradient along the droplet surface initiates Marangoni flows both in the water and the oil and a self-sustaining convective flow within the droplet. The velocity vectors in the droplet show the presence of convective flow with a one-directional vortex, which is in a good agreement with the experimental flow profile observed in real droplets (Fig. 2.6.). The flow is centrosymmetric, interestingly, the direction of the circular flow in the numerical solutions (clockwise or anticlockwise) varies with changes in the size of the triangulation grid parameters in the FEMLAB simulator. Changing the grid size introduces small differences in the initial conditions that make the computation converge on one solution or the other. Both solutions, however, have a similar flow pattern; i.e., the change of grid size changes the direction of flow but not the flow pattern. The existence of two symmetric solutions should be expected as there is no experimental evidence or other reason for the liquid in the simulation to circulate in a preferred direction. The magnitude of the flow velocity, as determined by the length of the vectors, is higher at the bottom than at the top region of the evaporating droplet as also seen in the experimental data in Figure 2.8.

Numerical simulations matching the two experimental conditions studied were performed at increasing evaporation times to check to what extent the simulation could explain the decrease in the fluid velocity and the cessation of the flow at the latest stages of the process. These calculations were provided with experimental parameters for the decreasing droplet size and evaporation rate. The diameters (D_d) and vertical positions (z) of droplet subdomain in the FEMLAB geometry were adjusted with the experimentally measured values at the specific drying times. The values of the evaporation mass flux, J_E, in equation 2-10 were also provided by experimental data. The temperature distributions inside the drying droplets computed with FEMLAB are shown in Figure 2.11.

The simulations show how, as the evaporation progresses, the smaller droplet size and the decrease in the evaporation rate suppress the temperature gradient at both experimental conditions. The initial temperature difference in the droplet is much larger at the higher evaporation rate. However, the diameter and the temperature gradient in the droplet with the higher evaporation rate decrease much faster, in agreement with the experimental data.

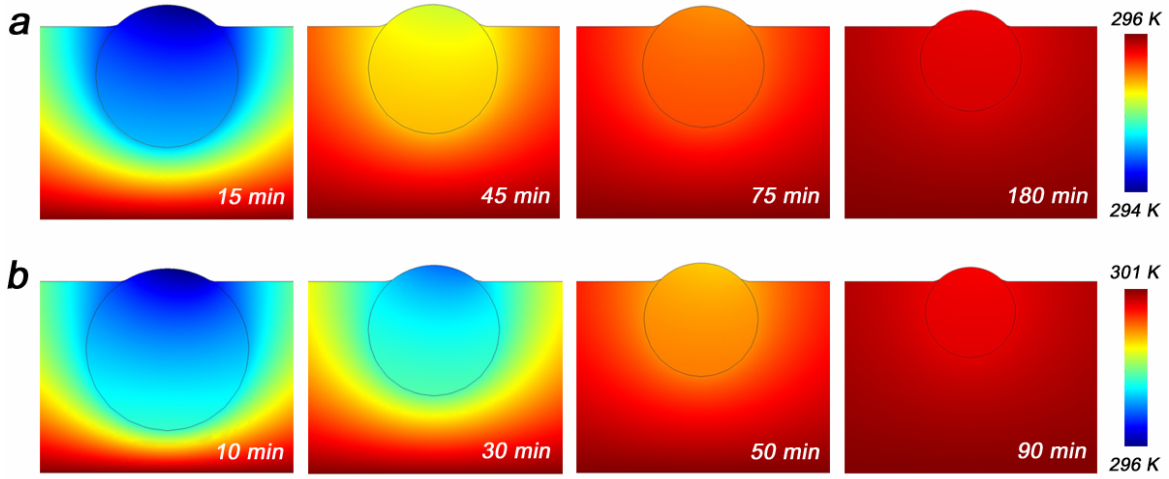

Figure 2.11. Simulation results for the temperature distribution in droplets at increasing drying times. (a) Relative humidity 55% and ambient temperature 23°C. (b) Relative humidity 51% and ambient temperature 28°C.

We now interpret the experimentally measured flow velocities in the framework of the above simulation results. The fluid inside each droplet will circulate as long as the Marangoni number, *Ma*, is above the critical Ma_c. The intensity of the circulation flow inside the droplets can be estimated by comparing their *Ma*. At RH 55% and 23°C after 15 min of drying, the temperature difference, ΔT, within the droplet is 0.61°C from the simulation and *Ma* (eq. 2-2) is calculated as 335. At RH 51% and 28°C after 10 min of drying the numerical simulation showed ΔT = 1.63°C and *Ma* = 1130. Both Marangoni numbers are larger than the critical Marangoni number, Ma_c. The evaporative mass and heat transport in the droplet lead to a convective Marangoni-driven flow. The magnitude of Marangoni flow velocity is dependent on the magnitude of the thermal differential. A higher value of *Ma* indicates that

the system has a tendency for faster flow velocity. Indeed, in the experiments we measured higher initial fluid velocity in the droplet at RH 51% and 28°C.

The convective fluid motion inside evaporating droplets stops abruptly at the moment when $Ma < Ma_c$. The moment when the circulation stopped was reached faster at RH 51% and 28°C even though the flow velocity in these droplets at the early stage of the evaporation was much higher (Fig. 2.8). This is expected, as the higher evaporation generates higher initial temperature gradient and faster circulation, however the droplet size also decreases faster, suppressing the temperature differential between top and bottom (Fig. 2.11). We estimated the critical Marangoni numbers on the basis of the calculated temperature gradient and the experimental data for size, evaporation flux and liquid velocity at which the convective flows in the droplets stopped. For both experimental conditions the critical Marangoni numbers were $Ma_c \sim 20$. These values are similar to the critical Marangoni number at which the first flow cell emerges in a liquid film with a temperature gradient along the fluid surface.[35,36] Although the geometry of our system is different we believe that that the similarity of the critical Marangoni numbers is reasonable.

The results obtained from the FEMLAB simulation confirm our hypothesis that the convective fluid motion inside the small drying droplets is driven by the temperature gradient created from water evaporation at the top surface. The restriction of this simulation to 2D systems is dictated by the limitations of the software and processing power. In effect, the simulation is valid for a liquid cylinder rather than a 3D sphere and the velocities and temperatures calculated will not be accurate for the real system. Nevertheless, we were able to establish good semi-quantitative correlation between the numerical simulation results and the experimental data. We believe that the simulation captures well the physics of the process and supports the model of circulation driven by a temperature gradient across the droplet.

The phenomenon of a convective flow generation is conceptually related to the earlier research on the fluid flow in the evaporating sessile or spherical droplet.[19,26-30] One difference between the flows that we have observed and simulated in the floating droplets and the flows reported in sessile droplets is that in our system the flow is in the form of one large flow cell,

instead of a being axisymmetric with respect to the vertical axis of the droplet. The non-axisymmetric flow pattern in our floating droplet can be explained with the dependence of interfacial-driven flow patterns on aspect ratio (AR) of the fluid container.[38,39] One-directional convective flow has been observed for systems with AR ~ 1,[40-42] which is also the case of our droplets.

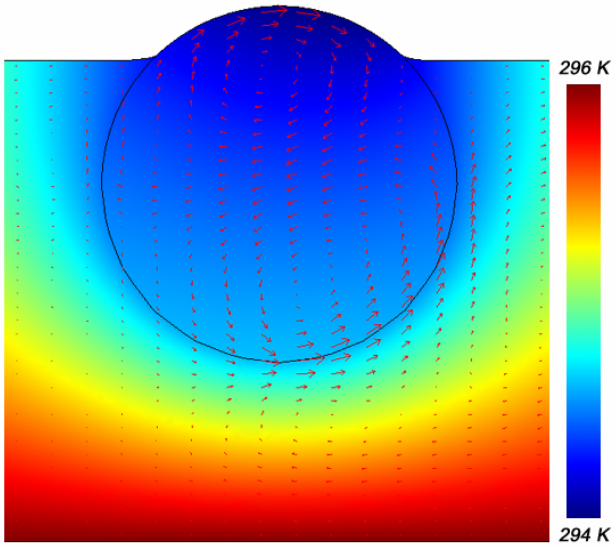

Figure 2.12. Simulation for the temperature distribution and velocity profile in an initial stage of a drying droplet with relative humidity 55% and ambient temperature 23°C. The boundary condition at water/air interface is $\tau_{water} - \tau_{air} = \nabla \sigma_{water/air} \cdot \bar{\mathbf{t}}$. Other boundary conditions are same as those described. The velocity vector magnitudes are represented by the lengths of the arrows. The liquid on the top moves in one direction, while the liquid further down moves in the opposite direction. The flows are broadly similar to the ones observed in free droplets before the surface is immobilized by the dense particle layer. After particles accumulate in the top section of the droplet they would immobilize the surface and suppress the top vortex.

We did not observe axisymmetric flows experimentally, but such flows are possible under certain conditions. For example, to understand the effect of the particle layer immobilizing the top surface, we preformed numerical simulations for a droplet with a particle-free surface with Marangoni stress boundary condition similar to eq. 2-12. The results are shown in Figure 2.12. The simulation points out to the initial formation of two vortices, which are plane-symmetric the 2D simulation, but the plane of symmetry is skewed

to one side, as the coldest point is not on top of the droplet, but to the side as warm liquid is being delivered from the other side. It is difficult to observe the top vortex experimentally, as the top part of the droplet is obscured by the meniscus, but our observations from above showed the liquid on top of the droplet indeed moves in one direction, while the liquid below moves in another direction. The situation changes significantly when the tops surface becomes immobilized by the particle layer. Lack of top surface mobility will suppress the top vortex, leaving only one large vortex in the droplet. The result is the centrosymmetric pattern observed experimentally and in the simulations reported in Figures 2.10 and 2.11. The system "self-organizes" by misbalancing the stresses and coupling them to flows, similarly to many processes driven by large gradients.

2.4. Potential Applications of Microseparations inside Evaporating Droplets

A variety of potential technological applications of the effects described here can be foreseen. The vertical distribution and microseparations of small particles suspended in the evaporating droplets can be useful in diverse droplet-based microfluidic systems. One possible application area is the on-chip synthesis of advanced particles from mixed particle suspensions. Our earlier work demonstrated how various anisotropic "supraparticles" from gold nanoparticles, silica spheres, latex particles, and polymers can be synthesized in droplets on a chip.[12] The one-directional circular flow in the evaporating droplet can be used in alternative strategies for mixing in microfluidic systems. Mixing in conventional microfluidic systems is a challenge because of the low Reynolds numbers of the liquid flow in microfluidic channels.[1,4,51] The circular flow inside our droplet, combined with the no-slip condition on the particle-blocked top surface, may prove helpful for mixing in various chemical reactions and materials synthesis processes.[52]

We demonstrate here a new microbioassay technique as an application directly based on the internal separation of particles within droplets on a chip. As a proof of that concept, evaporating droplets were used for on-chip detection of antibody-antigen binding (Fig. 2.13). The method is based on a common particle agglutination assay.[53] Two different types of 1 μL droplets were deposited on the F-oil, held by the electric field, and observed. Both droplets

contained 0.01 M phosphate buffered saline (PBS) solution with 0.2 mg/mL bovine serum albumin (BSA). The control droplet held a dispersion of a mixture of 3 wt% 1 μm latex particles coated with anti-rabbit immunoglobulin (IgG) and 0.02 wt% 40 nm gold nanoparticles coated with anti-rabbit IgG. The test droplet contained the same suspension of both types of colloids plus 10 μg/mL rabbit IgG (the antigen for the IgG on the particles). The suspensions were incubated for 15 minutes before droplets were deposited on the chip and observed during drying.

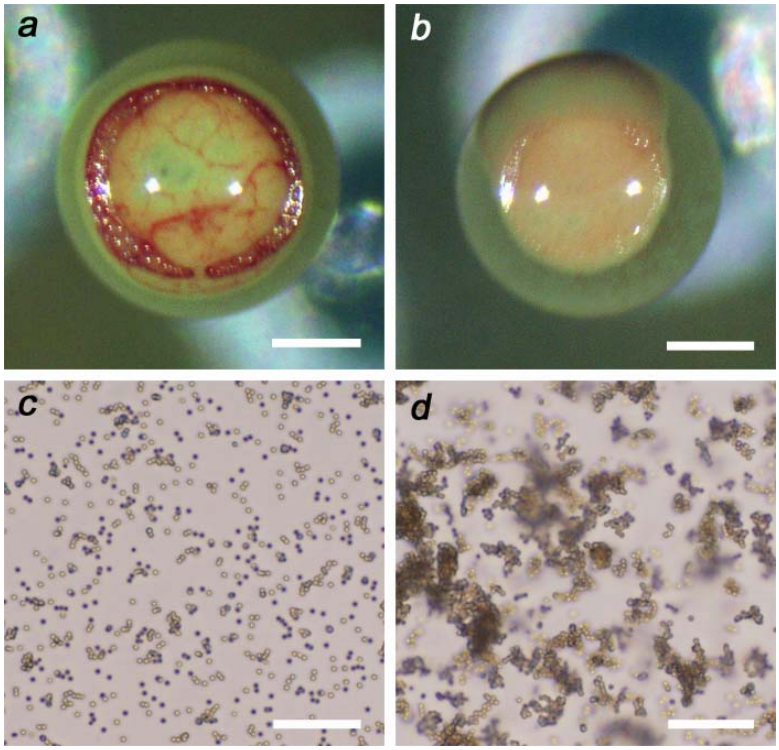

Figure 2.13. Typical experimental images of a microbioassay where the results are detected on the basis of particle separations inside evaporating droplets on a chip. Both droplets contain a binary suspension of 3 wt% 1 μm anti-rabbit IgG coated latex particles and 0.02 wt% 40 nm anti-rabbit IgG coated gold nanoparticles. (a) Negative control droplet after 30 min of drying. (b) Test droplet where 10 μg/mL of antibody (rabbit-IgG) is added after 30 min of drying. (c) Optical micrograph of same mixture as (a) illustrating that the particles remain dispersed. (d) Optical micrograph of same mixture as (b) proving that the agglutination has bound them in gold-latex clusters. Scale bars: (a) and (b) 200 μm; (c) and (d) 20 μm.

As the droplets began to dry, a dark gold nanoparticle "eyeball" spot appeared on the top surface of the negative control droplet without rabbit IgG (Fig. 2.13a). The gold nanoparticles in the droplet with rabbit IgG, however, were not visible on the surface (Fig. 2.13b). The reason is that the gold nanoparticles in the test droplet bind to the surface of the larger latex particles due to the antibody-antigen IgG interaction, forming as a result of the agglutination process large clusters seen by higher magnification microscopy (Fig. 2.13d). The gold nanoparticles in the negative control droplet on the other hand do not agglutinate and remain freely dispersed (Fig. 2.13c). The agglutinated gold nanoparticles in the test droplet can not pass through the interstices between the latex particles collected on the top section of the droplet, while the unbound free nanoparticles in the negative control droplet are dragged to the surface and form the darker ring seen in Figure 2.13a. Thus the process of microseparation inside the droplets allows direct and easy distinguishing of the aggregation state of the suspended particles affected by biomolecular binding. The droplet microseparation phenomena may thus enable the development of novel microfluidic techniques for highly sensitive, high-throughput biological microassays. A more detailed characterization of these miscrobioassays is under way and will be presented elsewhere.

2.5. Conclusions

We present a detailed investigation of vertical particle microseparations and a mechanism of flow generation within evaporating small droplets floating in denser oil. The major contribution of this work is obtaining experimental data for the transport of particles and liquid inside these freely suspended microdroplets. The data were obtained by the use of our dielectrophoretic liquid-liquid chip as an experimental tool for continuous monitoring of mass transfer in floating droplets. The phenomena observed were explained as a result of a series of processes driven by mass and heat transfer in the evaporating droplet. The internal circulation is driven by Marangoni instabilities. The FEMLAB simulation for hydrodynamic flows inside the droplet was in a good correlation with the experimental observations. These results present a beautiful illustration of a system with self-organizing dissipative structures.

The circulation helps transport the particles to the top surface, where they are captured by the evaporation outflux, and separated in a close-packed phase.

The mechanism of vertical redistribution of particles suspended in the droplet allows controlling particle separations on the microscale with a change of relative humidity, ambient temperature, and volatility of the liquid in the droplet. This microseparation technique has potential in various "microdroplet engineering" processes, as we demonstrated earlier by the directed synthesis of novel structured particles[12] and presently with the development of a new microbioassay technique using the evaporation as a means of detection. Such processes can find application in lab-on-a-chip devices for microsyntheis, microassays, manipulation and analysis of single cells and others.

2.6. Acknowledgements

We are grateful to Dr. Ketan Bhatt and Dr. Brian Prevo for performing the confocal microscopy experiments and to Dr. Rossitza Alargova for preparing the polymer microrods used as tracers. This study was supported by CAREER and NER grants from the National Science Foundation.

2.7. References

[1] Whitesides, G. M. and Stroock, A. D., Flexible methods for microfluidics. *Phys. Today* (2001) 54, 42-47.

[2] Blossey, R., Self-cleaning surfaces: virtual realities. *Nat. Mater.* (2003) 2, 301-306.

[3] Paik, P., Pamula, V. K. and Fair, R. B., Rapid droplet mixers for digital microfluidic systems. *Lab Chip* (2003) 3, 253-259.

[4] Stone, H. A., Stroock, A. D. and Ajdari, A., Engineering flows in small devices: Microfluidics toward a Lab-on-a-Chip. *Annu. Rev. Fluid Mech.* (2004) 36, 381-411.

[5] Zeng, J. and Korsmeyer, T., Principles of droplet electrohydrodynamics for lab-on-a-chip. *Lab Chip* (2004) 4, 265-277.

[6] Song, H., Tice, J. D. and Ismagilov, F., A microfluidic system for controlling reaction networks in time. *Angew. Chem. Int. Ed.* (2003) 42, 768-772.

[7] Roach, L. S., Song, H. and Ismagilov, R. F., Controlling nonspecific protein adsorption in a plug-based microfluidic system by controlling interfacial chemistry using fluorous-phase surfactants. *Anal. Chem.* (2005) 77, 785-796.

[8] Weigl, B. H. and Yager, P., Microfluidic diffusion-based separation and detection. *Science* (1999) 283, 346-347.

[9] Weigl, B. H. and Hedine, K., Lab-on-a-chip-based separation and detection technology for life science applications. *Am. Biotech. Lab.* (2002) 20, 28-30.

[10] Kutter, J. P., Current developments in electrophoretic and chromatographic separation methods on microfabricated devices. *Trends Anal. Chem.* (2000) 19, 352-363.

[11] Velev, O. D., Prevo, B. G. and Bhatt, K. H., On-chip manipulation of free droplets. *Nature* (2003) 426, 515-516.

[12] Millman, J. R., Bhatt, K. H., Prevo, B. G. and Velev, O. D., Anisotropic particle synthesis in dielectrophoretically controlled microdroplet reactors. *Nat. Mater.* (2005) 4, 98-102.

[13] Denkov, N. D., Velev, O. D., Kralchevsky, P. A., Ivanov, I. B., Yoshimura, H. and Nagayama, K., Mechanism of formation of two-dimensional crystals from latex particles on substrates. *Langmuir* (1992) 8, 3183-3190.

[14] Denkov, N. D., Velev, O. D., Kralchevsky, P. A., Ivanov, I. B., Yoshimura, H. and Nagayama, K., Two-dimensional crystallization. *Nature* (1993) 361, 26-26.

[15] Prevo, B. G. and Velev, O. D., Controlled, Rapid Deposition of Structured Coatings from Micro- and Nanoparticle Suspensions. *Langmuir* (2004) 20, 2099-2107.

[16] Deegan, R. D., Baksjin, O., Dupont, T. F., Huber, G., Nagel, S. R. and Witten, T. A., Capillary flow as the cause of ring stains from dried liquid drops. *Nature* (1997) 389, 827-829.

[17] Deegan, R. D., Pattern formation in drying drops. *Phys. Rev. E* (2000) 61, 475-485.

[18] Shmuylovich, L., Shen, A. Q. and Stone, H. A., Surface Morphology of Drying Latex Films: Multiple Ring Formation. *Langmuir* (2002) 18, 3441-3445.

[19] Maillard, M., Motte, L., Ngo, A. T. and Pileni, M. P., Rings and Hexagons Made of Nanocrystals: A Marangoni Effect. *J. Phys. Chem. B* (2000) 104, 11871-11877.

[20] Uno, K., Hayashi, K., Hayashi, T., Ito, K. and Kitano, H., Particle adsorption in evaporating droplets of polymer latex dispersions on hydrophilic and hydrophobic surfaces. *Colloid Polym. Sci.* (1998) 276, 810-815.

[21] Fan, F. and Stebe, K. J., Assembly of colloidal particles by evaporation on surfaces with patterned hydrophobicity. *Langmuir* (2004) 20, 3062-3067.

[22] Jing, J., Reed, J., Huang, J., Hu, X., Clarke, V., Edington, J., Housman, D., Anantharaman, T. S., Huff, E. J., Mishra, B., Porter, B., Shenker, A., Wolfson, E., Hiort, C., Kantor, R., Aston, C. and Schwartz, D. C., Automated high resolution optical mapping using arrayed, fluid-fixed molecules. *Proc. Natl. Acad. Sci. USA* (1998) 95, 8046-8051.

[23] Velev, O. D., Lenhoff, A. M. and Kaler, E. W., A class of microstructured particles through colloidal crystallization. *Science* (2000) 287, 2240-2243.

[24] Yi, G. R., Moon, J. H. and Yang, S. M., Ordered macroporous particles by colloidal templating. *Chem. Mater.* (2001) 13, 2613-2618.

[25] Iskandar, F., Gradon, L. and Okuyama, K., Control of the morphology of nanostructured particles prepared by the spray drying of a nanoparticle sol. *J. Colloid Inter. Sci.* (2003) 265, 296-303.

[26] Kang, K. H., Lee, S. J., Lee, C. M. and Kang, I. S., Quantitative visualization of flow inside an evaporating droplet using the ray tracing method. *Meas. Sci. Tech.* (2004) 15, 1104-1112.

[27] Hu, H. and Larson, R. G., Analysis of the effects of Marangoni stresses on the microflow in an evaporating sessile droplet. *Langmuir* (2005) 21, 3972-3980.

[28] Ruiz, O. E. and Black, W. Z., Evaporation of water droplets placed on a heated horizontal surface. *J. Heat Transfer* (2002) 124, 854-863.

[29] Savino, R., Paterna, D. and Lappa, M., Marangoni flotation of liquid droplets. *J. Fluid Mech.* (2003) 479, 307-326.

[30] Ha, V. and Lai C., Onset of Marangoni instability of a two-component evaporating droplet. *Int. J. Mass Heat Transfer* (2002) 45, 5143-5158.

[31] Hegseth, J. J., Rashidnia, N. and Chai, A., Natural convection in droplet evaporation. *Phys. Rev. E* (1996) 54, 1640-1644.

[32] Hu, H. and Larson, R. G., Evaporation of a sessile droplet on a substrate. *J. Phys.*

Chem. B (2002) 106, 1334-1344.

[33] Block, M. J., Surface tension as the cause of Benard cells and surface deformation in a liquid film. *Nature* (1956) 178, 650-651.

[34] Pearson, J. R. A., On convection cells induce by surface tension. *J. Fluid Mech.* (1958) 4, 489-500.

[35] Davis, S. H., Thermocapillary instabilities. *Ann. Rev. Fluid Mech.* (1987) 19, 403-435.

[36] Smith, M. K. and Davis, S. H., Instabilities of dynamic thermocapillary liquid layers. Part 1. Convective instabilities. *J. Fluid Mech.* (1983) 132, 119-144.

[37] Chaudhury, M. K. and Whitesides, G. M., How to make water run uphill. *Science* (1992) 256, 1539-1541.

[38] Schatz, M. F. and Neitzel, P. G., Experiments on thermocapillary instabilities. *Annu. Rev. Fluid Mech.* (2001) 33, 93-127.

[39] Rosenblat, S., Davis, S. H. and Homsy, G. M., Nonlinear Marangoni convection in bounded layers. Part 1. Circular cylindrical containers. *J. Fluid Mech.* (1982) 120, 91-122.

[40] Wagner, C. and Friedrich, R., Comments on the numerical investigation of Rayleigh and Marangoni convection in a vertical circular cylinder. *Phys. Fluids* (1994) 6, 1425-1433.

[41] Dauby, P. C., Lebon, G. and Bouhy, E., Linear Benard-Marangoni instability in rigid circular containers. *Phys. Rev. E* (1997) 56, 520-530.

[42] Ramón, M. L., Maza, D. and Mancini, H. L., Patterns in small aspect ratio Benard-Marangoni convection. *Phys. Rev. E* (1999) 60, 4193-4198.

[43] Czechowski, L. and Floryan, J. M., Marangoni instability in a finite container-transition between short and long wavelengths modes. *J. Heat Transfer* (2001) 123, 96-104.

[44] Nield, D. A., Surface tension and buoyancy effects in cellular convection. *J. Fluid Mech.* (1964) 19, 341-352.

[45] Krishnan, M., Ugaz, V. M. and Burns, M. A., PCR in a Rayleigh-Bénard convection cell. *Science* (2002) 298, 793.

[46] Alargova, R. G., Bhatt, K. H., Paunov, V. N. and Velev, O. D., Scalable synthesis of a new class of polymer microrods by a liquid-liquid dispersion technique. *Adv. Mater.* (2004) 16, 1653-1657.

[47] Alargova, R. G., Warhadpande, D. S., Paunov, V. N. and Velev, O. D., Foam superstabilization by polymer microrods. *Langmuir* (2004) 20, 10371-10374.

[48] Princen, H. M., *Surface and Colloid Science*, Matijevic, E., Ed., Wiley, New York, 1969, vol. 2, p 1-84.

[49] de Gennes, P., Brochard-Wyart, F. and Quéré, D., *Capillarity and Wetting Phenomena: Drops, Bubbles, Pearls, Waves*, Springer, New York, 2004.

[50] Yang, W., Mechanics of droplet evaporation on heated surfaces. *Lett. Heat Mass Transfer* (1978) 5, 151-166.

[51] Purcell, E. M., Life at low Reynolds number. *Am. J. Phys.* (1977) 45, 3-11.

[52] Brody, J. P., Yager, P., Goldstein, R. E. and Austin, R. H., Biotechnology at low Reynolds numbers. *Biophys. J.* (1996) 71, 3430-3441.

[53] Kasahara, Y., *Immunochemical Assays and Biosensor Technology for the 1990s*; Nakamura, R. M., Kasahara, Y. and Rechnitz, G. A., Eds., American Society for Microbiology, Washington, DC, 1992, p 127-147.

[54] Holman, J. P., *Heat Transfer*, 7th ed., McGraw-Hill Inc., UK, 1992.

[55] Savino, R., Monti, R. and Alterio, G., Drops pushing by Marangoni forces. *Phys. Fluids* (2001) 13,1513-1516.

Chapter 3

Remotely Powered Self-Propelling Particles and Micropumps Based on Miniature Diodes*

* Partially based on Chang, Paunov, Petsev and Velev, *Nature Materials*, 2007, 6, 235-240.

3.1 Introduction

Microsensors and micromachines capable of self-propulsion through fluids could revolutionize many aspects of technology, such as delivery vehicles of medicines in human body, roving sensors, and environmental monitoring for toxic organic molecules. Few principles to propel such devices and supply them with energy are known. The major obstacles include finding a source of power for motility, developing propellency principles and methods to control the direction and speed of motion. Conventional driving forces in macroscale to transport and manipulate micro or sub-microscale objects are mostly ineffective in microscale environments. Viscous effects predominate on the microscale and render most mechanical means of propulsion inefficient[1-4]. The flagellar and ciliar bacterial motors are among the few natural chemical-mechanical ways of propelling on the microscale[5-8]. Significant progress has been achieved in the synthesis of artificial molecular machines including molecular motors[9,10], shuttles[11], and "nanocars"[12]. Such molecular machines can in principle propel microdevices or act as micropumps when attached to walls[13,14], but it is hard to adapt these complex natural or artificial molecular structures to engineered devices[15]. A couple of notable studies report bimetal particles propelling via catalytic decomposition of solutions of hydrogen peroxide[16,17]. A few other papers discuss the undulatory motion of polymer gel under electric field[18,19], a swimming screw machine driven by an external magnetic field[20], a camphor boat with ester vapor as a chemical stimulus[21], biomimetic swimming robots inspired by *E. coli* motility[22], a carbon-fiber-based bioelectrochemical motor driven by oxidation of glucose[23], and 'microoxen' cells moving microscale loads[24]. Some of these particles, however, only move in special media, while others cannot be scaled to microscopic dimensions.

Here, we demonstrate how various semiconductor diodes form a new class of self-propelling "particles" and pumps in microfluidic devices. External energy is provided by a global external AC electric field. DC voltage is induced between the electrodes of each diode as a result of rectification of the AC field. The constant electric field between the electrodes leads to electroosmotic flow, which may propel the diodes or pump the adjacent liquid (Fig.

3.1). In effect, the semiconductor microelements harvest electric energy from external AC fields and convert it into mechanical propulsion on the microscale.

3.2. Experimental Section

3.2.1. Experimental Setup for Self-Propelling Diodes

The experiments except diode "gear" were carried out in a plastic Petri dish of dimensions 9 cm × 9 cm × 1.5 cm in depth. A couple of thin wire electrodes were submerged on the top and bottom of the vessel with 7 cm distance, providing uniform electric field across the liquid. The experiments of the diode "gear" were carried out in a vessel of dimensions 8 cm × 4 cm × 1 cm in depth with a 3.5 cm gap between the thin wire electrodes. The signal to the electrodes was provided by an AC generator (FG-7002C, EZ Digital Co. Ltd., Korea) and amplifier (PZD 700, Trek, Inc., Medina, NY, USA), and was monitored with oscilloscope and digital voltmeter. The smaller diodes were floated directly on the surface of water suspended by the interfacial tension, as shown in the top of Figure 3.1. Small floaters made of silicon glue were attached to the side of the larger switching diodes. The diode positions were observed with an Olympus SZ61 stereomicroscope and recorded with the attached Sony DSC-V1 digital camera.

Diode types used and their dimensions are silicon switching microdiodes for surface mounting (1.1 mm × 0.7 mm × 0.5 mm, Part no. 1N4448HWTDICT-ND, Digi-key Co.), Silicon switching diodes (3.7 mm × Ø 1.8 mm, Radioshack), surface mount light emitting diode (1.0 mm × 0.45 mm × 0.45 mm, Part no. JRC0168, IDEA, Inc.), light emitting diodes (Ø 3.0 mm, Radioshack), silicon photodiodes (2.25 mm × 2.25 mm × 2.75 mm, Part no. PDB-C144, Photonic Detectors Inc.), Zener diodes with reverse voltage 6V (1.2 mm × 0.6 mm × 0.6 mm, Part no. MAZS0620MLCT-ND, Digi-key Co.), Zener diodes with reverse voltage 12V (1.2 mm × 0.6 mm × 0.6 mm, Part no. MAZS1200MLCT-ND, Digi-key Co.).

3.2.2. Microfluidic Systems Embedded with Miniature Diodes

The microfluidic chips were fabricated from poly(dimethylsiloxane) (PDMS) using soft lithography. The rectangular channel master from SU-8 photoresist (MicroChem Co.,

Newton, MA, USA) was fabricated on a silicon wafer. Two silicon switching diodes were attached on the side wall of the master at the center of the longer channel using a 500 μm thick sticky rubber patch, as shown in the bottom of Figure 3.1. The PDMS (Sylgard 184, Dow Corining, Midland, MI, USA) was cast on the master with the attached diodes and cured at 70 °C. The PDMS replica with the embedded diodes was irreversibly sealed to a PDMS film coated on the glass slide using air-plasma cleaner (Model PDC-32G, Harrick Plasma, Ithaca, NY, USA).

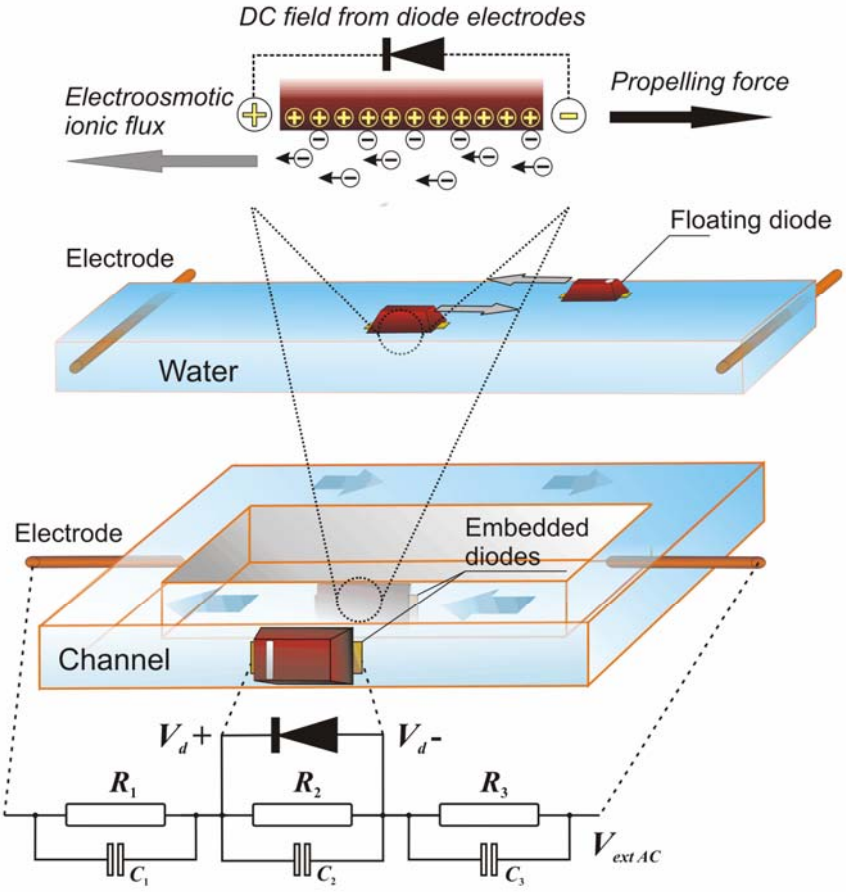

Figure 3.1. Schematics of the experiments for measuring floating diode velocity and diode pumping rate in a model microfluidic device. The origin of the localized electroosmotic flow and the equivalent electric circuit used to analyze the magnitude of the DC voltage V_d induced in the diode are shown in the top and bottom respectively.

The particles used in the microfluidic experiments included fluorescent 1 μm amidine-stabilized polystyrene latex from Interfacial Dynamics Co. (Portland, OR, USA) and fluorescent 2 μm sulfate-stabilized polystyrene latex from Molecular Probes (Eugene, OR, USA). The diode pumping was characterized with a dispersion of 0.002 wt% 2 μm fluorescent latex in deionized (DI) water at pH ~ 5.04 containing also 10^{-4} wt% Tween-20 and 10^{-5} M NaCl. The dispersions for the decoupling experiments contained 0.0002 wt% of amidine- and sulfate-stabilized latex particles each in pH ~ 7.0 DI water with 10^{-4} wt% Tween-20 and 10^{-5} M NaCl. The particle zeta-potentials at this pH measured by electrophoretic light scattering were -72.7 mV and -131 mV correspondingly. The suspensions were injected into the channel through two syringe needles inserted in the short channel sections. The external AC and DC electric fields were applied through the needles by using the generator in DC-offset mode. The motion of particles was monitored using Olympus BX-61 microscope in reflection and fluorescent mode microscopy.

3.3. Results and Discussion

3.3.1. Experimental Results and Theoretical Analysis of Diode Motility

Two types of experiments were performed in order to demonstrate how the flow of the adjacent liquid generated by the diodes can be used in microdevices. First, we studied how semiconductor diodes floating on the surface of water and aqueous solutions can self-propel directionally. The devices used included a range of regular (switching) diodes and diodes with additional functionality - light emitting diodes (LED), photodiodes and Zener diodes. Their sizes ranged from 1-millimeter microdiodes to regular diodes a few millimeters long. The diodes floated suspended by the interfacial tension on the surface of water contained in a wide Petri dish. AC fields of square wave form, frequency 10 Hz - 37 kHz and magnitude 30-150 V/cm were applied across the water by a pair of wire electrodes dipped at the sides of the container (Fig. 3.1).

The application of alternating electric fields did not lead to any perceptible liquid motion in the vessel or bubble formation at the thin wire electrodes. The field was spatially

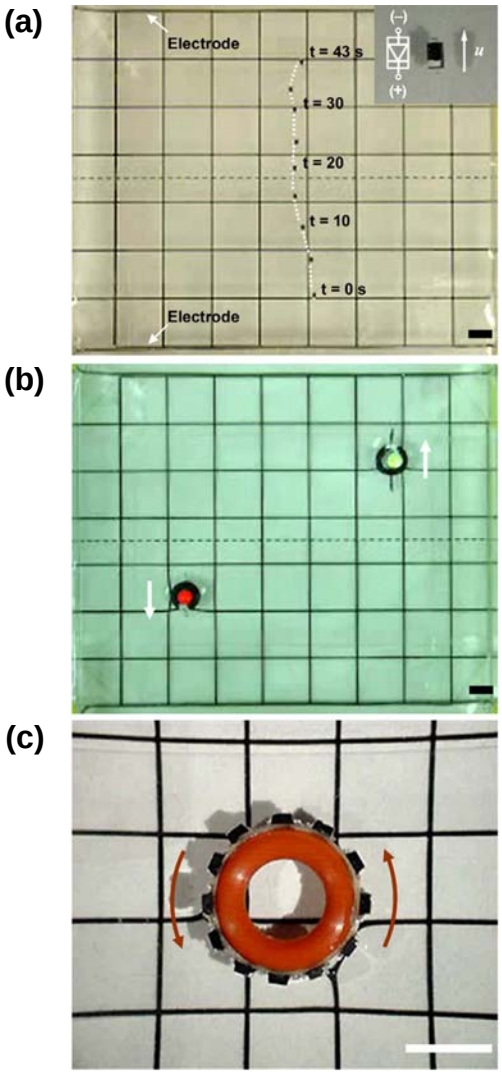

Figure 3.2. Optical micrographs of self-propelling semiconductor "particles": (a) Overlay of a series of photographs at low magnification showing the 5 cm directional "voyage" of a propelling microdiode (seen here as small black rectangle) for a total duration of 43 s. (b) Two LEDs light up and move towards the top or bottom depending on the orientation of their anodes (marked white). This experiment demonstrates the potential of diode-based devices to deliver additional functionality based on the voltage induced between their electrodes. (c) Use of diodes as propellers and actuators in MEMS - a rotor ring with diodes attached to its periphery spins around when an external field is applied. All experiments in (a), (b), (c) were performed at external voltage, E_{ext} = 120 V/cm, frequency 1 kHz, and 10^{-6} M NaCl. Scale bars = 5 mm.

uniform and there were no dielectrophoretic forces[25-27] (other than torque) acting on the particles. The diodes suspended on the liquid surface first became oriented in the direction of the field lines (perpendicular to the electrodes) when the field was turned on. The microelements then began to move parallel to the electric field, always in one direction only with regards to the orientation of their anode and cathode (Fig. 3.2a, b). Velocities as high as millimeters per second were observed. The diodes were propelled with approximately constant velocity until reaching the opposite electrode and then stopped a few millimeters in front and above the electrode where the intensity of the field decreases. If the diodes were then rotated manually in the opposite direction they moved with the same constant velocity until reaching the vicinity of the other electrode.

We proved that the diode motility results from a local electroosmotic flux powered by the external field. The specific direction of motion with regards to the diode cathode and anode points out that a DC field along the diode is responsible for its mobility. The origin of this DC field can be understood by analyzing the equivalent electric circuit of the experimental system, shown at the bottom of Figure 3.1. The electric voltage induced in the diode by the external field can be estimated from a model including resistors describing the ionic conductance through the bulk liquid and capacitors for the ionic layers. At the low frequencies used in this study the resistance is likely to be the leading contribution. The diode short-circuits the negative half-periods of the AC current. The resulting DC voltage of magnitude V_d induced in the diode can be approximated as

$$V_d = \frac{1}{2}\frac{R_2}{(R_1 + R_2 + R_3)} V_{ext} \qquad (3\text{-}1)$$

where V_{ext} is the AC peak-to-peak voltage applied to the electrodes in the dish and R_1-R_3 are defined in Figure 3.1. The coefficient of ½ accounts for the two-fold decrease of the voltage during the rectification of AC into DC. Assuming that the resistance of the liquid is linearly proportional to the distance between the electrodes, after expressing the external field

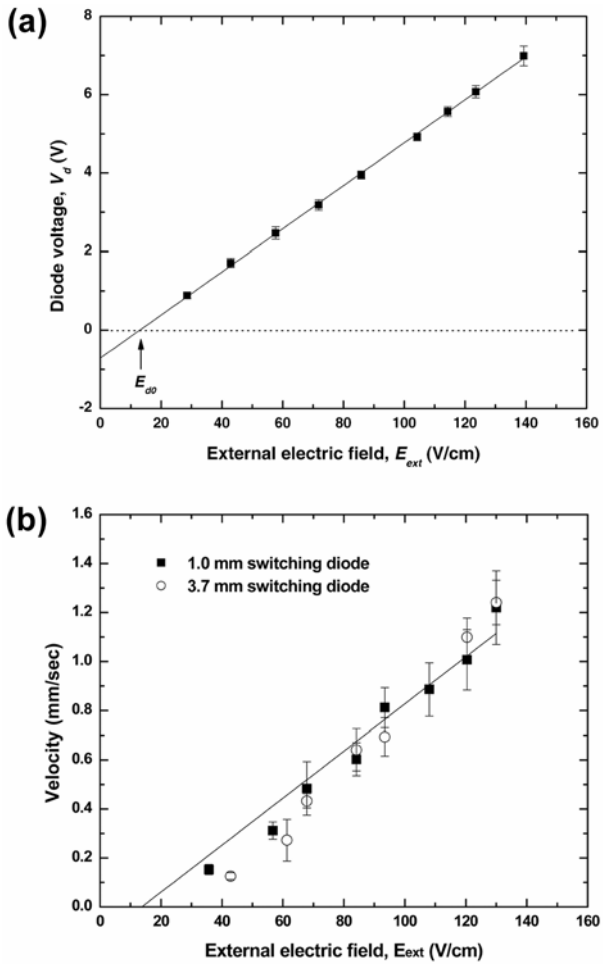

Figure 3.3. (a) Voltage generated across a fixed diode as a function of the external electric field E_{ext}. Two electrodes with 1 mm gap between them were brought in contact with the surface of the water solution of 10^{-6} M NaCl in the experimental vessel. DC voltages, V_d, induced across the diode were measured at a frequency of 1 kHz. The line is the least squares fit of the data and allows estimating the value of E_{d0}. The related value of offset voltage (≈ 0.7 V, intercept with y-axis) is in good agreement with typical specifications of silicon diodes. (b) Velocity as a function of the external AC field. The line is plotted on the basis of equation (3-4) with only one fitting parameter, β = 3.0. Note that the velocity of the diodes is similar even though there is almost 4-fold difference in their size.

intensity and substituting in equation (3-1), we arrive at the simple formula $V_d = E_{ext}\, l_d / 2$, where l_d is the length of the diode body and E_{ext} is the external AC field. Commercial semiconductor diodes have an offset voltage in the forward direction, which is an intrinsic

property of the *pn* junction[28]. In a real system this offset voltage has to be compensated for by an additional field of E_{d0}. Thus the above equation applied to real diodes reads:

$$V_d = \frac{l_d}{2}\left(E_{ext} - E_{d0}\right) \tag{3-2}$$

We measured the voltage generated across diodes dipped in the vessel as a function of the external field and distance between electrodes and found good quantitative agreement with this formula (Fig. 3.3a).

The DC field rectified between the electrodes gives rise to electroosmotic fluid flow along the plastic body of the diodes. This electroosmotic effect is analogous to the one used to pump liquids in microfluidic devices[29,30], however, it originates here at an electronic device converting locally the energy of the external field into flow. The electroosmotic flow pushes reactively the diodes in the opposite direction (see top portion of Fig. 3.1). The velocity of the electrokinetic flux u_w induced by the tangential DC field between the diode electrodes, E_w, can be estimated by the Helmholtz-Smoluchowski equation[31]

$$u_w = -\frac{\varepsilon \varepsilon_0 \zeta}{\mu} E_w \tag{3-3}$$

where ε and ε_0 are the dielectric permittivity of the media and vacuum, respectively, μ is the viscosity of the liquid phase and ζ is the potential in the plane of hydrodynamic shear[31]. The velocity, u, of a particle floating on a free liquid interface is likely to be different than that of a completely submerged particle, so we add a hydrodynamic resistance correction coefficient β in the equation: $u = -\beta u_w$. The electric field along the diode wall is $E_w = V_d / l_d$. Substituting these relations in equation (3-3), we obtain a formula estimating the diode velocity as a function of the intensity of the external AC field

$$u = \beta \frac{\varepsilon \varepsilon_0 \zeta}{2\ \mu}\left(E_{ext} - E_{d0}\right) \tag{3-4}$$

Notably, equations (3-3) and (3-4) differ not only in the coefficients, but in the type of electric field, DC in equation (3-3) and AC in equation (3-4). An intuitive way of presenting equation (3-4) is that a diode subjected to an external AC field will "short-circuit" all half-periods of the field in the direction in which the diode is conductive; the remaining "rectified" half-periods will generate electroosmotic flux, which in turn will propel the diode. This formula demonstrates that the self-propelling effect reported here does not depend on the diode size, which cancels out of the expressions. A microscopic diode-based device could move about as fast as a macrosized diode. We verified this simple model by experiments where the velocities of a 1-mm sized microdiode and a regular 3.7-mm diode were measured as a function of the applied voltage (Fig. 3.3b). The velocities of both diodes were approximately equal (the average velocity of the microdiode actually was a little higher at lower fields, possibly due to the lower hydrodynamic drag). After substituting the value of E_{d0} measured experimentally in the static diode experiments, and assuming a typical value of $\zeta = 80$ mV, we fitted these data by equation (3-4) with the only fitting parameter of $\beta = 3.0$. This is a reasonable value for the coefficient of hydrodynamic resistance β as the diode moves onto a free liquid surface and where the resistance is likely to be smaller than for a fully immersed particle. Verifying equation (3-4) for smaller diodes is presently difficult due to the lack of commercial devices of such size, however, alternative fabrication techniques[32,33] might allow in the future to test the technique with much smaller diodes and investigate the effects of Brownian motion and counterionic atmosphere in the Hükel regime[31].

3.3.2. Effect of Operating Parameters on Diode Mobility

The electroosmotic nature of the phenomena was proven by a variety of experiments. The ζ-potential of the plastic diode surface is a function of pH, electrolyte concentration, and presence of charged surface-active species. We examined the effect of varying concentrations of acids, bases, charged surfactants, and electrolytes on the diode mobility. The strongest effect is observed when pH is increased by adding NaOH or Na_2HPO_4 . The mobility of the

diode first decreases and then changes direction (i.e., instead of moving in the direction of their anode the diodes begin propelling with the cathode side in front). This can be attributed to re-charging of the diode surface at higher pH. Indeed, when these data are plotted in coordinates of velocity vs. pH (Fig. 3.4a), they overlap, indicating an isoelectric point of the diode polymer surface at pH $\approx$6.4. Negatively charged surfactant, sodium dodecyl sulphate, first suppressed the mobility of the diodes and then reversed their direction. Positively charged surfactant, cetyl trimethyl ammonium chloride, on the other hand increased the diode mobility (Fig. 3.4b). Such effects are common in electroosmosis and can be explained by change of the intrinsic charge of the surface because of surfactant adsorption[31]. These changes in diode motion direction and velocity suggests a potential for sensing functions based on surface functionality. The effect of electrolyte was also typical for electroosmotic-driven flows, as the velocity remained approximately constant at small electrolyte concentrations, while bubbling and electrochemical flows emerged at higher electrolyte concentrations. We also established that the diodes self-propel in non-aqueous media such as ethylene glycol and dimethyl sulfoxide (Fig. 3.4c).

Finally, we characterized the diode velocity in water as a function of the frequency of the external electric field (Fig. 3.4d). We found no correlation between these two parameters within the frequency range of 10 Hz to 37 kHz. This result proves that the contribution of AC electrokinetic effects is negligibly small, as AC electrokinetics[25,34-40], arising from ionic mobility in electric field gradients, is strongly dependent on the field frequency. It also points out that the diodes could be powered with fields in the radio (RF) or even microwave frequency range. Prototypes of small, inexpensive, yet complex, microcircuits powered remotely by external RF fields already exist in the form of radio frequency identification (RFID) microchips.

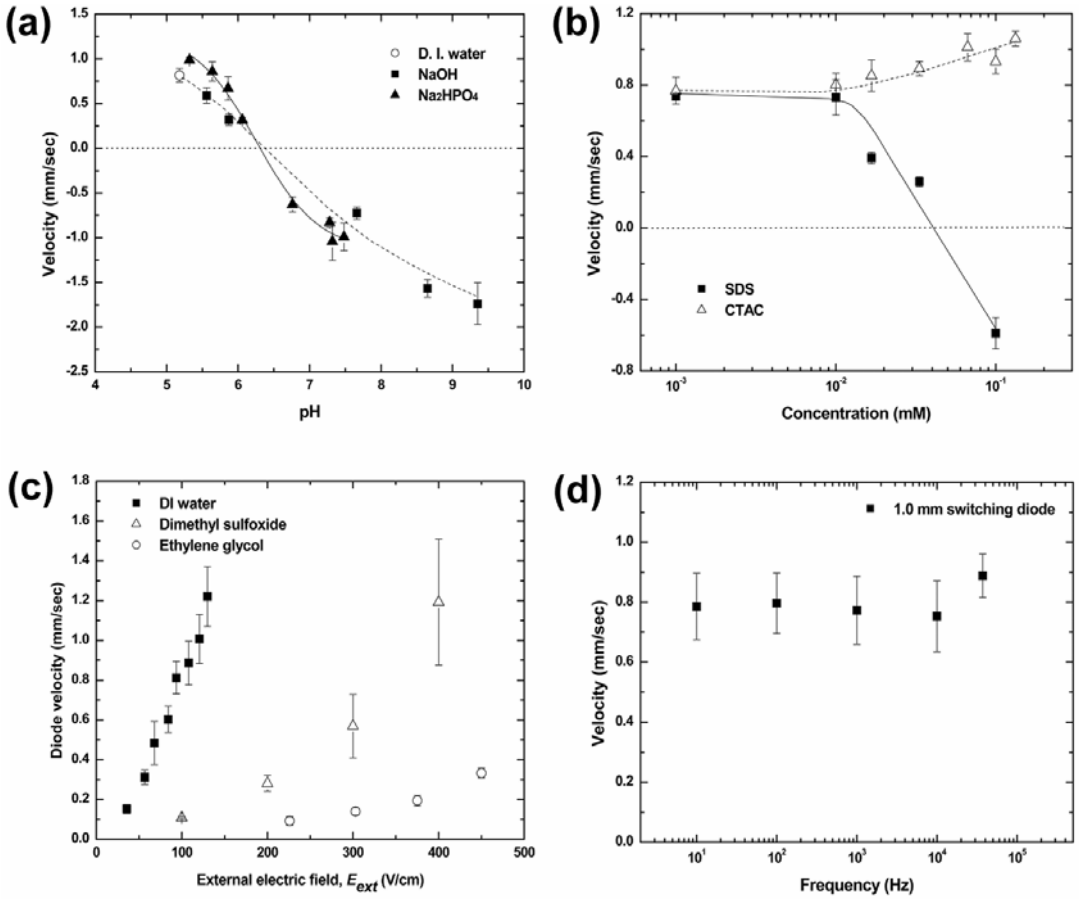

Figure 3.4. Dependence of the diode velocity on the parameters controlling the electroosmotic propellant force. (a) Diode velocity as a function of pH. The direction of the motion changes at a pH = 6.4, as the surface charge of the resin body changes sign at the isoelectric point. (b) Velocity as a function of the concentration of surfactants. Positively charged surfactant (CTAC) leads to small increase of the velocity by increasing the surface charge. Negatively charged surfactant (SDS) decreases the positive surface charge of the diode to the extent that the charge is reversed and the diode begins moving in the opposite direction. Experiments were performed at E_{ext} = 93 V/cm and 1 kHz. (c) Diodes can also propel in non-aqueous media. Diode velocity in organic solvents is lower than on water due to high viscosity and lower surface charge. Experiments were performed at frequency 1 kHz. (d) Diode velocity is not a function of the frequency of the external field up to frequencies in the RF region.

3.3.3. Autonomous Motion of Diodes with Complex Functionalities

Self-propelling diodes, powered remotely, may form the basis of a new class of microdevices of unprecedented complexity. We demonstrated rudimentary examples of a range of functionalities by using different types of commercial diodes (Table 3.1).

Table 3.1. Types of semiconductor elements used and functionality demonstrated.

Type of diode	Mobility specifics	Principle demonstrated
Regular switching	Moves with velocity $u \sim E_{ext}$	Electrohydrodynamic propulsion (Fig. 3.3b)
Light-emitting (LED)	Moves and emits light	Double functionality, propulsion and light emitting (Fig. 3.2b)
Zener	Moves at an approximately constant velocity above a certain E_{ext}	Internal electronic control of motility (Fig. 3.5a)
Photodiode	Movement stops when illuminated with strong light source	External control of motility by light (Fig. 3.5b)

The voltage rectified between the diode electrodes can also be used to power additional functions of the electronic microcircuits. For example, light emitting diodes (LEDs) suspended in the experimental vessel both propelled themselves electroosmotically and emitted light (Fig. 3.2b), demonstrating that the DC voltage rectified between the electrodes can power additional device functions. A rudimentary control of the velocity by a pre-programmed function of the semiconductor element was achieved by using Zener diodes, which stabilize the reverse voltage on their *pn* junction at a certain threshold value[28]. Indeed, the electroosmotic velocity of Zener diodes remained approximately constant above the corresponding value of the external voltage (Fig. 3.5a). Moving diodes can respond to external stimuli or signals, which was demonstrated by the use of photodiodes whose velocity could be controlled by light (Fig. 3.5b). The particle-localized electrohydrodynamic

effect described here can also be used in diode-actuated electroosmotic motors and actuators. This was illustrated by constructing "gears" powered by a ring of regular switching diodes or by LEDs converting the energy of the external field into rotational motion. (Fig. 3.2c).

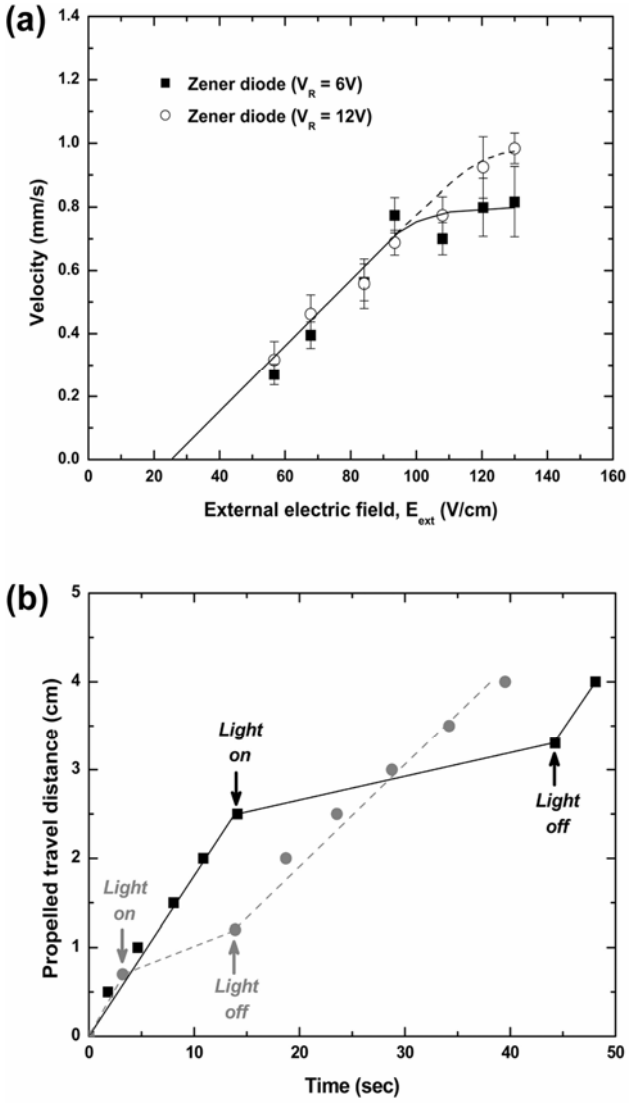

Figure 3.5. Diode propulsion with additional functionality. (a) When Zener diodes are used instead of switching diode the maximal velocity is restricted as a function of the characteristic reverse voltage of the Zener element. The curves are guides to the eye. Experiments were performed at 1 kHz with 10^{-6} M NaCl solution. (b) Positions of two photodiodes propelling across the same vessel - when either of them is illuminated with a strong beam of light it begins moving slower. Experiments were performed at E_{ext} = 100 V/cm and 1kHz with 10^{-6} M NaCl solution.

3.4. Potential Applications of Diode Propulsion Force

The electroosmotic flux of the liquid generated between the diode electrodes can also be used to pump liquids on the microscale, if the diodes are immobilized. In the second cycle of experiments we proved that the diodes can operate as distributed, locally operating, micropumps in microfluidic devices. The test microfluidic device constructed to evaluate the diode pumping action is schematically shown in the bottom half of Figure 3.1. It was based on a closed rectangular channel 600 μm wide and 570 μm high and of overall dimensions of 20 mm×5 mm. The AC field was applied to two electrodes situated symmetrically in the opposing short sections of the channel. Because of the symmetry of the channel and electrode placement, neither AC nor DC fields applied to the electrodes could engender macroscopic liquid circulation. The pumping was performed by two diodes embedded in the opposing walls of the channel and oriented in the same direction. The liquid flow was observed with the help with fluorescent tracer particles. When an AC field was applied to the electrodes, macroscopic circulation of the liquid around the channel was observed as a result of the local electroosmotic flow driven by the diodes. At the same time, intense movement of the liquid in the direction of the macroscopic flow and a backflow in the middle of the channel were observed between the diode surfaces (Fig. 3.6a). The dependence of the microscopic velocity (measured in the channel without diodes) on the AC voltage applied (Fig. 3.6c) was similar to the velocity of diode propulsion (cf. Fig. 3.6c with Fig. 3.3b). Instead of pumping the liquid, the two diodes in the channel wall could act as a microfluidic mixer when facing in opposite directions and creating a circular flow inside the channel (Fig. 3.6b). Theoretical calculations of the macroscopic flux and computer simulations of the flow pattern in between the diodes were in excellent agreement with the experimental data and are presented in Chapter 4 with details of diode mixing.

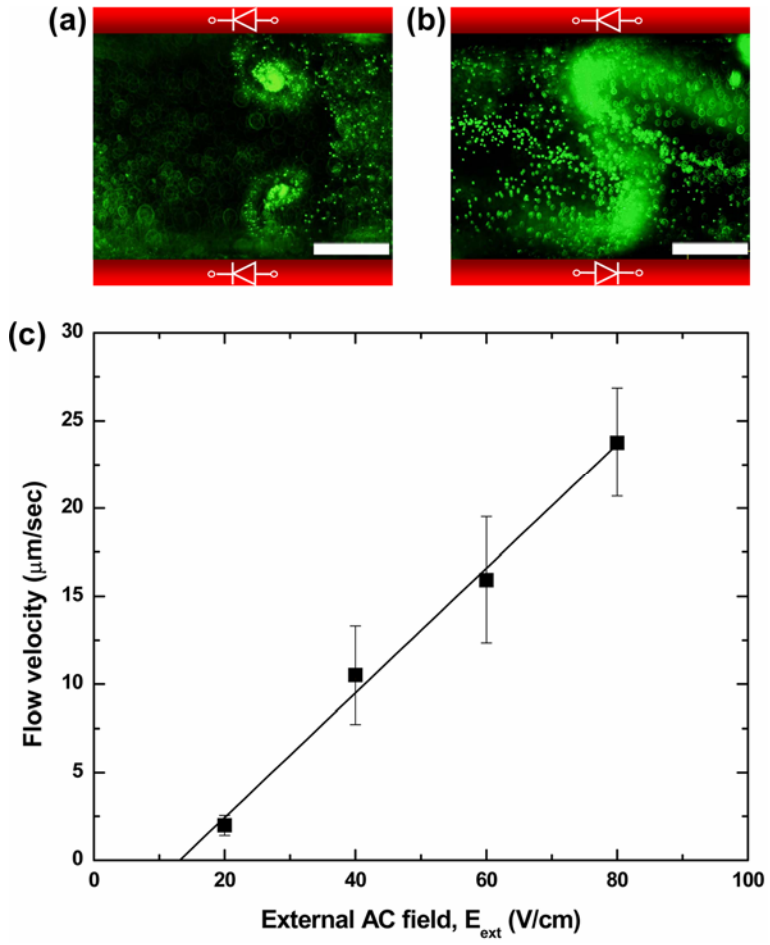

Figure 3.6. Flow of particle suspension in a microfluidic channel generated by two diodes embedded in the top and bottom sides of the channel, as observed from above. (a) Optical micrograph illustrating pumping and backflow for diodes with the same orientation. The diodes create a unidirectional flow by moving the liquid adjacent to the wall in same direction. (b) Micrograph illustrating the flow generated by two diodes with opposite orientation. The diodes create a circular flow by moving the liquid adjacent to the wall in opposite directions, which can be used for microfluidic mixing. (c) Velocity of the liquid pumped at the center of the long channel without diodes (circulating through the microfluidic loop) as a function of the external AC field. The error bars reflect the scattering in multiple experimental measurements. Scale bars = 200 μm.

A major advantage of this method is the ability to position multiple micropumps and mixers in different locations on the chip and power all of them with a global AC field (or RF waves) applied to the whole device. The AC field driven pumps open unique opportunities in

microfluidics when combined with DC electrophoresis and DC electroosmosis. One example is the ability to decouple the electrophoretic mobility of a particle or a biomolecule from the flow of the surrounding liquid. The difference in the charge and electrophoretic mobility is the major factor of separation of proteins, polynucleotides, cells and particles in microfluidic devices[41-45]. The particles are separated in external DC field. Typically, however, the surrounding liquid also moves by electroosmosis and particles with small differences in electrophoretic mobility might not be separated during the time they are transported through the channel[45]. The diode pumps, however, are actuated by AC fields, which do not affect the electrophoretic mobility of the particles outside of the diode location. The velocity of a particle, V_{particle}, will be the sum of the electrophoretic and liquid velocities

$$V_{\text{particle}} = V_{\text{eph}}(E_{\text{DC}}) + V_{\text{liquid}}(E_{\text{AC}})$$

The DC and the AC components of the field can be applied simultaneously, but controlled independently. The AC field controls the liquid flow from the diode pump, while the DC field controls the electrophoretic particle velocity. If the AC-induced liquid flow is in a direction opposite to the one of the particles, they could be moved either in the positive direction, when $|V_{\text{eph}}| < |V_{\text{liquid}}|$, or in the negative one, when $|V_{\text{eph}}| > |V_{\text{liquid}}|$. For each value of the DC component there is a value of the AC field where the electrophoretic mobility will be fully compensated by the diode-generated counterflux, so each type of particle in a mixture can be held in place by a dynamic equilibrium and separated from the others. By precisely adjusting the DC and AC components, particles with small differences in charges or size can be separated more efficiently than by electrophoresis alone. The ability to drive the diode pumps at the high frequencies and the relatively low fields used could avoid problems with fluid flows and vortices in areas of non-uniform field that may occur in pumping by conventional AC electrohydrodynamics[36-40].

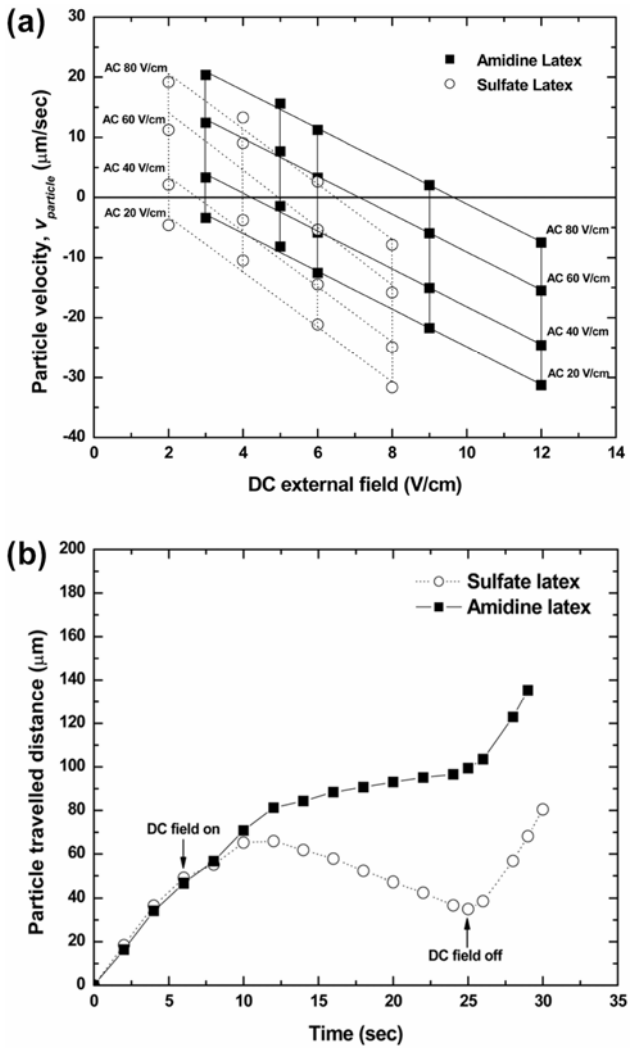

Figure 3.7. Particle separation inside diode pumping system under simultaneous application of AC and DC field. (a) Particle velocities at the center of the long channel without diodes as a function of the magnitude of the AC and DC components of the external field. The AC-driven diode pumps move the liquid in the positive direction. The increase of the DC component increases the (negative) electrophoretic velocity of the particles. At precisely adjusted values of the DC and AC fields near the position of dynamic equilibrium particles with small differences in surface charge can be separated efficiently. (b) Mobility of two particles of slightly different charge measured in terms of particle position. The particles begin moving together when the liquid is moved by AC pumping at 40 V only. The application of DC field of 4V introduces an electrophoretic component of the motion in a direction opposite to the one of the AC pumped flow. The sulfate latex particle begins moving faster than the fluid, while the amidine latex moves a slower than the surrounding fluid. The particles begin moving in opposite direction and the distance between them increases with time.

We proved the above separation concept by experiments with a mixture of two types of negatively charged particles. The velocities of each particle type in the long channel (without the diodes) as a function of the DC and AC components of the field are plotted in Figure 3.7. The principle of the technique can be illustrated by considering, e.g., the velocity of the two types of particles at DC = 6 V/cm and AC = 60 V/cm (Fig. 3.7a). The two particles move in different directions, even though they carry charges of the same sign. The trajectories of the two particles in the diode pumping system are plotted in Figure 3.7b. Such microfluidic processes conveniently controlled by two electrical parameters can lead to highly precise particle, cell and biomolecule separations and characterizations on a chip.

3.5. Conclusions

We demonstrate that semiconductor elements (diodes in this study and more complex devices in the future) may not only be used in electric circuits, but might also serve as building blocks of new classes of functional materials and devices. In future implementations the power to the propelling particles and distributed electroosmotic pumps could be provided by AC electric fields of higher frequencies potentially spanning the radio frequency and microwave regions. The DC voltage rectified across the diode electrodes can be used to power microcircuits encased in the microdevices. The electroosmotic propellency, combined with internal logic functions, may be used in dynamically reconfigurable microfluidic chips, spatially-evolving active microsensor networks, or possibly in future complex motile devices such as microbots for medical diagnostics and surgery.

3.6. Acknowledgements

This research was performed in collaboration with Prof. Vesselin Paunov (University of Hull, Hull, UK) and Prof. Dimiter Petsev (University of New Mexico, Albuquerque, USA). We acknowledge the Defense Advanced Research Projects Agency (DARPA/AFSOR) and NSF-CAREER (NCSU), NSF/NIRT and NSF/PREM DMR (UNM) and the EPSCR (UK) for support of this study. We are grateful to Yong-Jae Choi and Dr. Tzy-Jiun Mark Luo for access to the plasma cleaner for microchannel fabrication.

3.7. References

[1] Purcell, E. M., Life at low Reynolds number. *Am*. *J*. *Phys*. (1977) 45, 3-11.

[2] Brody, J. P., Yager, P., Goldstein, R. E. and Austin, R. H., Biotechnology at low Reynolds numbers. *Biophys*. *J*. (1996) 71**,** 3430-3441.

[3] Shapere, A. and Wilczek, F., Self-propulsion at low Reynolds number. *Phys*. *Rev*. *Lett*. (1987) 58**,** 2051-2054.

[4] Becker, L. E., Koehler, S. A. and Stone, H. A., On self-propulsion of micro-machines at low Reynolds number: Purcell's three-link swimmer. *J*. *Fluid Mech*. (2003) 490, 15-35.

[5] Berg, H. C. and Anderson, R. A., Bacteria swim by rotating their flagellar filaments. *Nature* (1973) 245, 380-382.

[6] Blair, D. F. and Berg, H. C., Restoration of torque in defective flagellar motors. *Science* (1988) 242, 1678-1681.

[7] Samuel, A. D. T. and Berg, H. C., Fluctuation analysis of rotational speeds of the bacterial flagellar motor. *Proc*. *Natl Acad*. *Sci*. *USA* (1995) 92, 3502-3506.

[8] Nelson, P. C., *Biological Physics: Energy*, *Information*, *Life*, Ch.5, Freeman, New York, 2004.

[9] Hernández, J. V., Kay, E. R. and Leigh, D. A., A reversible synthetic rotary molecular motor. *Science* (2004) 306, 1532-1537.

[10] Kelly, T. R., De Silva, H. and Silva, R.A., Unidirectional rotary motion in a molecular system. *Nature* (1999) 401, 150-152.

[11] Brouwer, A. M. *et al*., Photoinduction of fast, reversible translational motion in a hydrogen-bonded molecular shuttle. *Science* (2001) 291, 2124-2128.

[12] Shirai, Y., Osgood, A. J., Zhao, Y., Kelly, K. F. and Tour, J. M., Directional control in thermally driven single-molecule nanocars. *Nano Lett*. (2005) 5, 2330-2334.

[13] Vicario, J. *et al*., Nanomotor rotates microscale objects. *Nature* (2006) 440, 163.

[14] Darnton, N., Turner, L., Breuer, K. and Berg, H. C., Moving fluid with bacterial carpets. *Biophys*. *J*. (2004) 86, 1863-1870.

[15] Requicha, A. A. G., Nanorobots, NEMS, and nanoassembly. *Proc*. *IEEE* (2003) 91,

1922-1933.

[16] Ismagilov, R. F., Schwartz, A., Bowden, N. and Whitesides, G. M., Autonomous movement and self-assembly. *Angew. Chem. Int. Ed.* (2002) 41, 652-654.

[17] Paxton, W. F. *et al.*, Catalytic nanomotors: autonomous movement of striped nanorods. *J. Am. Chem. Soc.* (2004) 126, 13424-13431.

[18] Osada, Y., Okuzaki, H. and Hori, H., A polymer gel with electrically driven motility. *Nature* (1992) 355, 242-244.

[19] Osada, Y. and Gong, J. P., Soft and wet materials: polymer gels. *Adv. Mater.* (1998) 10, 827-837.

[20] Ishiyama, K., Sendoh, M., Yamazaki, A. and Arai, K. I., Swimming micro-machine driven by magnetic torque. *Sensor Actuat. A-Phys.* (2001) 91, 141-144.

[21] Nakata, S. and Matsuo, K., Characteristic self-motion of a camphor boat sensitive to ester vapor. *Langmuir* (2005) 21, 982-984.

[22] Behkam, B. and Sitti, M., *E. coli* inspired propulsion for swimming microrobots. *Proc. International Mechanical Engineering Conference and R&D Exposition*, Anaheim, USA (2004).

[23] Mano, N. and Heller. A., Bioelectrochemical propulsion. *J. Am. Chem. Soc.* (2005) 127, 11574-11575.

[24] Weibel, D. B. *et al.*, Microoxen: Microorganisms to move microscale loads. *Proc. Natl. Acad. Sci. USA* (2005) 102, 11963-11967.

[25] Morgan, H. and Green, N. G., *AC Electrokinetics: Colloids and Nanoparticles*, Research Studies Press, Hertfordshire, UK, 2002.

[26] Velev, O. D., *Colloids and Colloid Assemblies,* Caruso, F., Ed., p. 437-460, Wiley-VCH, Weinheim, 2003.

[27] Evoy, S. *et al.*, Dielectrophoretic assembly and integration of nanowire devices with functional CMOS operating circuitry. *Microelectron. Eng.* (2004) 75, 31-42.

[28] Streetman, B. G., *Solid State Electronic Devices*, Prentice Hall, New Jersey, 1990.

[29] Paul, P. H., Arnold, D. W., Neyer, D. W. and Smith, K. B., Electrokinetic pump application in micro-total analysis systems; mechanical actuation to HPLC. *Proc. the*

μ-TAS 2000, Enschede, Netherlands, 2000.

[30] Chen, L. X., Ma, J. P., Tan, F. and Guan, Y. F., Generating high-pressure sub-microliter flow rate in packed microchannel by electroosmotic force: potential application in microfluidic systems. *Sensor Actuat*. *B-Chem*. (2003) 88, 260-265.

[31] Hunter, R. J., *Foundations of Colloid Science*, Oxford Univ. Press, New York, 2001.

[32] Kovtyukhova, N. I. *et al*., Layer-by-Layer assembly of rectifying junctions in and on metal nanowires. *J*. *Phys*. *Chem*. *B* (2001) 105, 8762-8769.

[33] Kovtyukhova, N. I. and Mallouk, T. E., Nanowire p-n heterojunction diodes made by templated assembly of multilayer carbon-nanotube/polymer/semiconductor-particle shells around metal nanowires. *Adv*. *Mat*. (2005) 17, 187-192.

[34] Ramos, A., Morgan, H., Green, N. G. and Castellanos, A., AC electrokinetics: a review of forces in microelectrode structures. *J*. *Phys*. *D*: *Appl*. *Phys*. (1998) 31, 2338-2353.

[35] Bhatt, K. H., Grego, S. and Velev, O. D., An AC electrokinetic technique for collection and concentration of particles and cells on patterned electrodes. *Langmuir* (2005) 21, 6603-6612.

[36] Dukhin, S. S. and Mishchuk, N. A., Concentration polarization of a conducting particle in strong fields. *Kolloidn*. *Zh*. (1990) 52, 452-456.

[37] Ajdari, A., Pumping liquids using asymmetric electrode arrays. *Phys*. *Rev*. *E* (2000) 61, R45-R48.

[38] Bazant, M. Z. and Squires, T. M., Induced-charge electrokinetic phenomena: Theory and microfluidic applications. *Phys*. *Rev*. *Lett*. (2004) 92, 066101.

[39] Debesset, S., Hayden, C. J., Dalton, C., Eijkel, J. C. T. and Manz, A., An AC electroosmotic micropump for circular chromatographic applications. *Lab Chip* (2004) 4, 396-400.

[40] Bazant, M. Z. and Ben, Y., Theoretical prediction of fast 3D AC electroosmotic pumps. *Lab Chip* (2006) 6, 1455-1461.

[41] Greenlee, R. D. and Ivory, C. F., Protein focusing in a conductivity gradient. *Biotechnol. Prog.* (1998) 14, 300-319.

[42] Wang, Q., Lin, S. L., Warnick, K., Tolley, H. D. and Lee, M., Voltage-controlled

separation of proteins by electromobility focusing in dialysis hollow fiber. *J. Chromatogr. A* (2003) 985, 455-462.

[43] Kaniaski, D. *et al.,* Electrophoretic separations on chips with hydrodynamically closed separation systems. *Electrophoresis* (2003) 24, 2208-2227.

[44] Guttman, A., *Electrokinetic Phenomena*, Rathore, A. S. and Guttman, A., Ed., p 69-108, Marcel Dekker, New York, 2004.

[45] Heiger, D., *High performance capillary electrophoresis: An introduction*, Agilent Technologies, Germany, 2000.

Chapter 4

Remotely Powered Distributed Microfluidic Pumps and Mixers Based on Miniature Diodes*

* Partially based on Chang, Beaumont, Petsev and Velev, *Lab Chip*, 2008, 8, 117-124.

4.1 Introduction

Manipulation of fluids, colloidal particles, or biomolecules on the microscale can be performed in integrated devices for sample pre-treatment and analyte detection. Such systems integrated in a single chip are known as micro-Total Analysis Systems (μTAS) or lab-on-a-chip devices.[1-6] In comparison to conventional laboratory techniques, these miniaturized analysis systems are more flexible, allow easy automation and require significantly reduced samples sizes and analysis times. The precise control of fluid and particle transport inside the microfluidic channels is of paramount importance for the progress in their design and utilization.

Reducing the channel dimensions to the micrometer scale results in a laminar flow, characterized by low Reynolds numbers ($Re = U\,d/v$, where U is the average flow velocity, d is the characteristic width of the channel and v is the kinematic viscosity of the liquid). This means that the viscous forces dominate the fluid behaviour, while the inertial contribution is negligible.[6,7] The laminar fluid motion makes operations like fluid pumping and solute mixing very challenging. Laminar flows normally lead to low Péclet number ($Pe = U\,d/D$, where D is the molecular diffusivity), indicating that the solute transport is predominantly due to molecular diffusion.[3,6-10] Hence, new tools for microfluidic flow control, manipulation and stirring are needed.

Mechanical pumps are not the best solution to overcome the viscous resistance of fluid flow in microchannels. A large external pump defies miniaturization and low energy consumption, which are among the main advantages of microfluidic devices.[11,12] Alternatively, microfluidic flows have been driven by electroosmosis,[13-15] piezoelectrics,[11] internal pressure difference of liquid drops,[12] thermal gradients,[16,17] optically actuated pumps,[18,19] or catalytic micropumps.[20,21] Some of these micropumps, however, are difficult to fabricate because of their complex structures, whereas others are limited to a specific chemical solution. Alternate current (AC) field micropumps have been reported that create net flow over asymmetric electrode structures.[22-27] An important advantage of using AC field is the minimization of electrolysis, which may occur during DC electroosmosis.[28] AC

electrohydrodynamic pumps, however, need complicated electrode micropatterns and can only operate in a limited range of AC frequencies.

Microfluidic mixing may be accomplished by passive or active mixers. The passive mixers guide the fluid flow through specially designed channels, where it is subjected to repeated splitting and recombination,[29,30] chaotic advection in staggered herringbones[9] or three-dimensional serpentine channels,[31,32] and Dean flows in curvilinear or spiral channels.[10,33] Passive mixers, however, require complex channel geometries and more importantly can not be turned on and off on demand. In the active mixers the fluid is actuated using external energy, by miniature magnetic stirrers,[34] ultrasonic actuation,[35] electrowetting of droplets,[36,37] and electrohydrodynamic flows.[38-43] The moving components in some active mixers are difficult to fabricate and integrate into a microfluidic chip. A disadvantage of the electrohydrodynamic mixers is the difficulty of patterning complex electrode structures and heterogeneously charged surfaces inside the microchannels.

In our previous work,[44] as described in Chapter 3, we demonstrated how diodes suspended in liquid can self-propel by local electroosmotic flow. We suggested on this basis a new approach for pumping liquids and controlling flow pattern in microchannels based on miniature diodes. These diodes are powered by an external AC field that is locally rectified into a direct current (DC) field across the diode electrodes. This DC field gives rise to an electroosmotic flow in the liquid adjacent to the diode surface. The DC voltage (V_d) induced between the electrodes of the floating diode as a result of rectification of the external AC field (E_{ext}) can be evaluated as

$$V_d = \frac{l}{2}(E_{ext} - E_{d0}) \tag{4-1}$$

where l is the length of the diode body and E_{d0} is the electric field compensated by an offset voltage on the diodes. The latter is an intrinsic property of the semiconducting *pn* junctions.[45] Electroosmosis is induced by the interaction of ions in the electric double layer at the diode surface with the tangential component of the applied electric field. The electroosmotic velocity (u_{eo}) is well approximated by the Helmholtz-Smoluchowski equation, which is valid for thin double layers,[8,46]

$$u_{eo} = -\frac{\varepsilon\,\varepsilon_0\,\zeta}{\mu}E \tag{4-2}$$

where ε_0 is the dielectric constant in a vacuum, ε is the relative dielectric permittivity of the liquid, ζ is the electrokinetic zeta potential, μ is the fluid dynamic viscosity and E is the electric field. The reactive motion of the floating diode induced by the local electroosmotic flow can be evaluated by combining equations (4-1) and (4-2) with the addition of a hydrodynamic-resistance correction coefficient, β,

$$u_d = \beta\frac{\varepsilon\varepsilon_0\zeta}{\mu}\frac{V_d}{l} = \beta\frac{\varepsilon\varepsilon_0\zeta}{2\mu}(E_{ext} - E_{d0}) \tag{4-3}$$

In this Chapter, we present detailed results and discussion of the fluid pumping and flow pattern control using semiconductor diodes with externally applied AC electric field. The diodes are immobilized alongside the channel walls and depending on their mutual orientation can operate as pumps or mixers. The parameters that govern the fluid flow are identified and their effects are analyzed quantitatively and modelled numerically.

4.2. Experimental Section

4.2.1. Fabrication of Microfluidic Channels

The microfluidic channels were fabricated in poly(dimethylsiloxane) (PDMS, Sylgard 184, Dow Corning) using soft lithography.[47,48] Channel masters were created by coating SU-8 2050 photoresist (MicroChem, Inc.) on a silicon wafer to a thickness of ~200 μm using a spin-coater (Model P6700, Specialty Coating Systems, Inc.). Then, the wafer was soft-baked on a hot plate. The procedure was repeated twice on the same wafer to obtain thicknesses of ~570 μm for the rectangular loop channel and ~590 μm for the Y-shaped mixer channel. The transparency photomasks with the channel printout were brought in contact with the SU-8 photoresist followed by a UV exposure (Model B-100A, BLAK-RAY). After a post-baking, the UV exposed wafers were developed in a SU-8 developer solution (MicroChem, Inc.) and hard-baked.

Two 1-mm long silicon switching diodes (Part no. 1N4448HWTDICT-ND, Digi-key, Co.) were attached to the side wall of the channels using a 500 μm thick sticky rubber patch

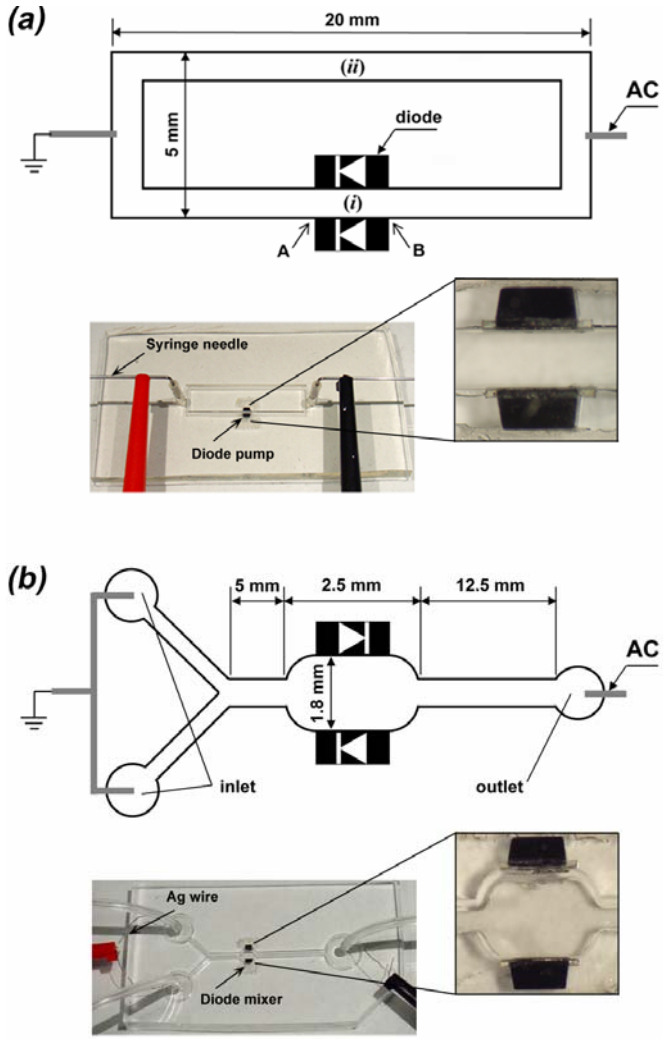

Figure 4.1. (a) Microfluidic device for diode pumping. Two 1-mm long diodes were attached on the channel wall facing in the same direction for diode pump. The electroosmotic flow driven by the diodes was monitored at point (i) between the diodes. The flow velocity of the pump was measured at the centre of the longer channel without diodes (ii), using tracing microspheres. (b) Microfluidic device for diode mixing. The two diodes were attached on the chamber wall facing in opposite directions. Milli-Q water and fluorescent dye solution were injected continuously into each inlet by a syringe pump. The mixing efficiency after applying the external AC field was monitored using confocal microscope. The microchannels and diodes in both schematics are not to scale.

(Fig. 4.1). The PDMS was then cast on the masters and cured at 70 °C. Two holes were punched at the centre of the short channel sections in the PDMS layer containing the rectangular loop channel using a 16-gauge needle to inject fluids and connect electrodes.

Similar inlet and outlet ports were also punched in the PDMS layer containing the Y-shaped channel. Finally, the polymerized PDMS replicas with the embedded diodes were irreversibly sealed to a PDMS film coated on the glass slides after pre-treatment by an air-plasma cleaner (Model PDC-32G, Harrick Plasma).

4.2.2. Microfluidic Pumping Using Diodes

Arranging two diodes in parallel orientation on both sides of the channel creates a micropump that is powered by the global AC field (Fig. 4.1a). The resultant fluid motion was monitored by tracing a particle dispersion of 0.002 wt% 2 μm fluorescent sulphate-stabilized latex (Molecular Probes) in Milli-Q water at various pH values. The solutions also contained 10^{-4} wt% Tween-20 and 10^{-5} M NaCl. The rectangular loop channel with ~300 μm channel width was used for pH 5.0 and 7.3 solutions, while the pumping experiment at pH 6.0 was performed in ~600 μm wide channel. The trace particle suspensions were injected into the chip through two syringe needles inserted in the access holes at the short channel sections. The AC electric field generated by a function generator (Model 33120A, Agilent) and amplifier (PZD 700, Trek) was applied through the syringe needles. The tracer particles motion was monitored (i) between the two diodes and (ii) at the centre of the longer channel without diodes using an Olympus BX-61 microscope in reflection and fluorescent mode (Fig. 4.1a). Time-lapse micrographs were taken using 50× objective and high resolution Olympus DP-70 digital CCD camera. Two frames of the images were superimposed in Adobe Photoshop and then the distances travelled by each tracer particle were measured from their coordinates in the image.[4] The particle velocities were then calculated by dividing the particle displacement by the time span between the two frames.

4.2.3. Microfluidic Mixing Using Diodes

The mixing chamber is created by embedding the diodes in an anti-parallel orientation in the walls of the microchannel (Fig. 4.2b). Silver wire electrodes were placed into the ports of the Y-shaped channel. Rubber tubing (Norton Co.) was inserted into the inlet and outlet ports. The efficiency of microfluidic mixing in the diode chamber was characterized with a neutral

fluorescent dye (Texas Red dye-labelled dextran conjugate) obtained from Molecular Probes. Milli-Q water and 10^{-4} M Texas Red solution, which were adjusted to pH ~ 5.4 also containing 10^{-4} wt% Tween-20 and 10^{-5} M NaCl, were flown into each of the inlet ports using a syringe pump (Model NE 1800, New Era Pump Systems, Inc.). The distribution of dye in the flows was measured by confocal microscopy using a FV 300 scanner attached to the Olympus BX-61 system.

4.3. Results and Discussion

4.3.1. Diode Pumping

Macroscopic circulation in the closed rectangular channel was not observed in the absence of diodes on the wall under AC or DC fields because of the symmetry of the channel and the electrode placement - the electroosmotic force in the upper half of the rectangular channel loop is exactly balanced by the one in the lower half (see Fig. 4.1a). The liquid in the loop channel far from the diodes, however, began circulating upon application of external AC electric fields of square wave-form, frequency 1 kHz and magnitude 20-80 V cm^{-1}. The rectified DC field in the diode section leads to electroosmotic pumping. The equivalent circuit diagram is presented in our earlier publication.[44] Intensive circulation is visible in the diode section, including the formation of two vortices between the diodes (see Fig. 3.6a in Chapter 3). These vortices are a result of the backpressure of the viscous liquid in the channel loop. As the electroosmotic force is present only at the diode surfaces, the bulk liquid between the diodes shows some degree of recirculation.

The liquid in the closed rectangular loop began circulating through the channel once the external field applied was larger than the diode offset voltage (Fig. 4.2). The direction of the macroscopic circulation was the same as the direction of the local electroosmotic flows at the diode surfaces. The formation of bubbles by electrolysis at the diode electrodes was not observed in these experimental conditions. All flows driven by the diodes had a linear dependence on the applied AC electric fields (Fig. 4.2). This flow direction depends on the pH and diode orientation. The effect of pH near the isoelectric point of the diode surface (pI ~ 6.4, as estimated in our earlier work[44]) can be attributed to the change of the sign of the

zeta potential at the diode-solution interface. The local electroosmotic motion on the diode surfaces at lower pH values (pH 5.0 and 6.0) was directed from the anode to the cathode of the diode (that is, from position B to A in Fig. 4.1a). The liquid in remaining part of the channel circulated in a clockwise direction (that is, from position A to B in Fig. 4.1a). At higher pH value (pH 7.3), however, the direction of the electroosmotic flow between two diodes reversed, and the resulting circulation changed direction, shown as the negative velocities in Figure 4.2. The maximal experimental velocity of ~ 40 μm sec^{-1} was obtained at an AC field of 80 V cm^{-1} at pH 7.3 (Fig. 4.2). The fluid velocity in the two vortices between the diodes also increased as the applied voltage increased.

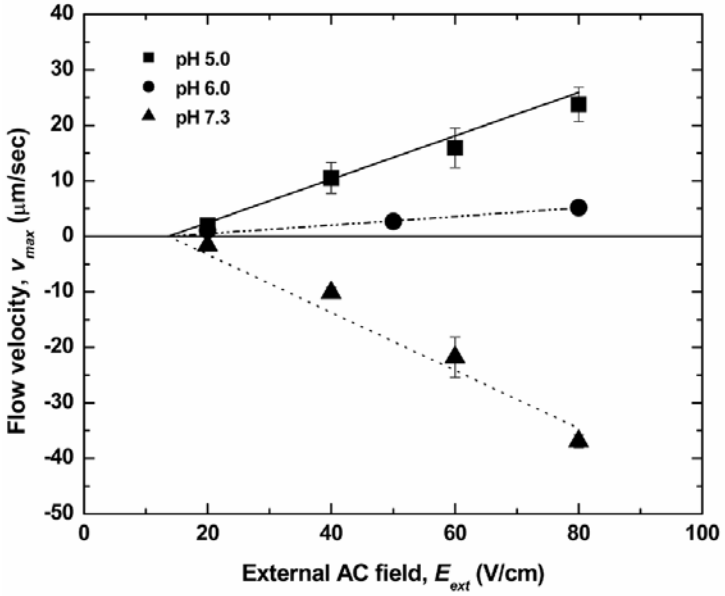

Figure 4.2. Flow velocities measured in the microfluidic loop channel at different pH values as a function of AC external field. The lines are plotted by the analytical solution from equations (4-6) and (4-7) with zeta potential as fitting parameter (ζ = +60 mV, +25 mV, -80 mV for pH = 5.0, 6.0, 7.3, respectively).

4.3.2. Theoretical Analysis of the Diode Pump

The interpretation of the data for the diode pump is based on a separate theoretical analysis of the pump region and the rest of the rectangular loop channel (see Fig. 4.1a). In the following section, we first consider the electroosmotic vortex generation between the diodes and then the resulting macroscopic circulation in the remaining channel section.

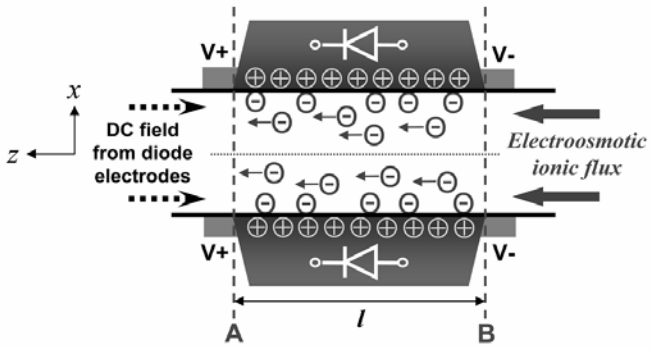

Figure 4.3. Schematic illustration of the localized electroosmotic flow for the pumping in a microchannel with a pair of diodes oriented in the same direction in low pH solutions. The charge at the diode surface results in the formation of an electric double layer. When AC field is applied, the diode shortens the field in one direction and behaves as a near dielectric object in the other.

The diode pump with electroosmotic flow between a pair of the parallel-oriented diodes in low pH solutions is sketched in Figure 4.3. The electroosmotic flow between the two diodes is opposed by the viscous resistance of the fluid in the rest of the channel, which induces a counterpressure gradient across the diodes' ends. This results in the backflow in the middle of the channel between the diodes and the complex shape of the fluid velocity profile. This flow pattern is broadly similar to the electroosmotic flow combined with pressure driven flow such as in closed tube electroosmosis.[49-51]

The counterpressure, ΔP, compensating for electroosmotic flow in a capillary is given by a balance of viscous and electrical body forces,[50]

$$\Delta P = \frac{32\,\varepsilon_0\,\varepsilon\,\zeta\,L}{d_0^{\,2}}E \tag{4-4}$$

where d_0 and L are the diameter and length of a capillary. The rectified DC field (E_d) across a diode under an external AC field was derived from equation (4-1),

$$E_d = \frac{1}{2}(E_{ext} - E_{d0}) \tag{4-5}$$

Assuming that the cross section of the channel is rectangular (the actual shape of the channel cross section is slightly trapezoidal) and after substituting equation (4-5) into equation (4-4),

we obtain a formula for the pressure difference created across the diode pump as a function of the external AC field,

$$\Delta P = P_A - P_B = \frac{16\,\varepsilon_0\,\varepsilon\,\zeta\,l}{d_h^2}(E_{ext} - E_{d0}) \tag{4-6}$$

where P_A and P_B are the average pressures acting on planes A and B in Figure 4.3, respectively, and d_h is the hydraulic diameter of the channel defined as the channel cross-sectional area divided by the wetted perimeter.[52]

The pressure drop across the diode pump creates also pressure gradients through the whole channel, which give a rise to fluid motion. The fully developed velocity profile in a microchannel with rectangular cross-section is given by[53,54]

$$\begin{aligned} v_z(x,y) &= \frac{\Delta P}{2\,\mu\,l_T}\left(b^2 - y^2 - \frac{4}{b}\sum_{n=0}^{\infty}(-1)^n\,\frac{1}{m^3}\,\frac{\cos my\cosh mx}{\cosh ma}\right) \\ m &= \frac{\pi(2n+1)}{2b} \end{aligned} \tag{4-7}$$

where ΔP is the pressure drop along the microchannel, a and b are the half of channel width and height, respectively, and l_T is the channel length, which can be considered to be the total length of the rectangular loop channel after subtracting the diode body length.

Introducing equation (4-6) into equation (4-7), we obtain a formula for the macroscopic flow profiles pumped by the diodes, which linearly depends on the external AC electric field. After substituting the physical parameters of the liquid phase, we plotted the maximum velocity $v_z(0,0)$ with one fitting parameter - the zeta potential for each experimental condition (Fig. 4.2). The fitted zeta potential values are reasonable, as typical magnitudes of ζ are on the order of 100 mV or lower. The macroscopic flow velocities measured experimentally at position (ii) in Figure 4.1a can be considered as fully developed because channel entrance effects are negligible. The theoretical calculations of the macroscopic flow induced by the diode pump are in good agreement with the experimental data (Fig. 4.2). The velocity of the liquid pumped by the diodes decreases as pH increases. Once pH exceeds the pI of the diode surface, the sign of the zeta potential reverses. The

electroosmotic pressure gradient through the channel is in the opposite direction at this higher pH, resulting in the pumping in the reverse direction.

The efficiency of the diode pump presented here does not depend on the AC frequency. This was already verified in the study of self-propelling semiconductor diode as its motility showed no correlation with the AC field frequency in the range 10 Hz ~ 40 kHz. This is a major difference with the AC electrohydrodynamic pumps, which have an optimal range of frequency (5 kHz ~ 17 kHz for the maximum flow rate).[23-27,44,55] In addition, the diode pumps operate at 20-100 times lower electric field intensities than the AC electrohydrodynamic pumps reported in the literature and do not need complex electrode micropatterns (a detailed comparison is described in Table 4.1). The integration of our diode pumps into devices with microchannels may be simple and straightforward. Single miniature diodes can be used to locally pump and control fluids at specific position in the chip, while multiple diodes in organized arrays with increased surfaces may increase the power of the AC-driven pumps.

Table 4.1. Parametric comparison - published AC electrohydrodynamic pumps and diode pumps reported in this study.

Authors / year	Channel dimension (μm)	electrode gap (μm)	Length of periodic electrode patterned (mm)	u_{max} (μm/sec)	Operating voltage (V)	Operating Frequency (kHz)	Electric field (V/cm)	Q_{max} (μL/sec)
Brown et al. (2000) [1]	H 340 (laterally open-channel)	4.5	6.5	120	1.2 Vrms	~ 0.8	2667	-
Studer et al. (2002)	W 50 × H 20	3	-	40	1.5 V	5	5000	9.6×10^{-7}
Mpholo et al. (2003) [2]	H 280 (laterally open-channel)	2	5.28	450	2.2 Vrms	14 ~ 17	11000	-
Debesset et al. (2004) [4]	W 100 × H 100 (loop-channel)	5	28.19	50	1.8 Vrms	5	3600	0.0005
Studer et al. (2004) [5]	W 100 × H 20 (loop-channel) *flow direction is dependent on the frequency.	8.7	6	500	8 Vrms	32	9195	0.001
Bazant & Ben (2006) [6] *Theoretical prediction	W 500 × H 100	5	-	190	1 Vrms	10	2000	0.009
Velev Group (2008)	W 300 × H 570	2 cm	1 mm (diode length)	40	160 Vpp	independent	80	0.003

[1] Brown, ABD; Smith, CG; Rennie, AR, *Phys. Rev. E* (2000) 63, 016305.
[2] Studer, V; Pepin, A; Chen, Y; Ajdari, A, *Microelectronic Eng.* (2002) 61-62, 915-920.
[3] Mpholo, M; Smith, CG; Brown, ABD, *Sensors Actuators B* (2003) 92, 262-268.
[4] Debesset, S; Hayden, CJ; Dalton, C; Eijkel, JCT; Manz, A, *Lab Chip* (2004) 4, 396-400.
[5] Studer, V; Pepin, A; Chen, Y; Ajdari, A, *Analyst* (2004) 129, 944-949.
[6] Bazant, MZ & Ben, Y, *Lab Chip* (2006) 6, 1455-1461.

4.3.3. Numerical Simulation of Fluid Flows in Diode Pumping

The diode-driven flow velocity distribution in two-dimensional (2D) rectangular loop channel as shown in Figure 4.1a was simulated to compare to the experimentally observed profile using the COMSOL multiphysics 3.3 package (COMSOL, Burlington, MA). We solved the continuity and Navier-Stokes equations for fluid motion in the diode pumping system,

$$\nabla \cdot \mathbf{V} = 0 \tag{4-8}$$

$$\frac{\partial \mathbf{V}}{\partial t} + \mathbf{V} \cdot \nabla \mathbf{V} + \frac{1}{\rho} \nabla P = \nu \nabla^2 \mathbf{V} \tag{4-9}$$

where **V** is the velocity vector, ρ is the density of liquid, P is the pressure, ν is the kinematic viscosity. The Debye length, used as characteristic thickness of electric double layer in the electrolyte solution, is ~ 100 nm, which is much smaller than the length scale of the microchannel. Therefore, the electric double layer thickness can be neglected in the simulation domain. The electroosmotic flow velocity in equation (4-2) was used as a liquid slip boundary condition on the diode surface for the numerical calculations,[38,39] while no-slip condition was applied at the channel walls beyond the diodes. The dielectric permittivity and hydrodynamic properties of water were ε = 80, ρ = 1000 kg m^{-3} and $\mu = 10^{-3}$ kg m^{-1} s^{-1}. The zeta potential at the diodes surfaces was +60 mV. The rest of the channel (apart from the diode region) is not subject to directional electric field and hence does not contribute to the electroosmotic driving force, although it contributes to the overall hydrodynamic resistance.

The electric field inside the channel for calculating the electroosmotic flow at the diode surfaces was simulated during the positive half-cycle of the applied AC voltage, because the diode acts as a conductor during the other cycle. The electric potential distribution in the rectangular channel domain was calculated using the Poisson equation,

$$\nabla^2 \phi = -\frac{\rho_e}{\varepsilon_0 \varepsilon} \tag{4-10}$$

where ϕ is the electric potential and ρ_e is the electric charge density. The rectified electric potentials on the diode electrodes were provided by the experimental data in our previous work.[44] We assume that the physical properties of the fluids were uniform in the whole

microchannel domain during the field application. A steady state flow is assumed in equation (4-9), which is reasonable for the low *Re* regimes that correspond to our experiment.[39,40]

The computed flow profiles between the diodes at the channel wall for ζ = +60 mV and E_{ext} = 80 V cm^{-1} are shown in Figure 4.4a. The velocity vectors near the diode surfaces are oriented in the same direction, toward the cathodes of the diodes. The flow in the middle of the channel is in the reverse direction due to the loop channel counterpressure, which is in good agreement with the experimental flow pattern. However, there is a net flow in the direction of the electroosmotic flow since the flux at the diode walls is greater than the back flux in the centre. This net flow is conserved along the loop channel due to the fluid incompressibility and is exactly equal to the bulk flow rate far from the diodes. We observed a faster rate of vortex rotation between the diodes at the larger external fields during the pumping experiments. Similarly, the velocity of the reverse electroosmotic flow between the diodes in the simulations also increases with the magnitude of external AC field (Figure 4.5a).

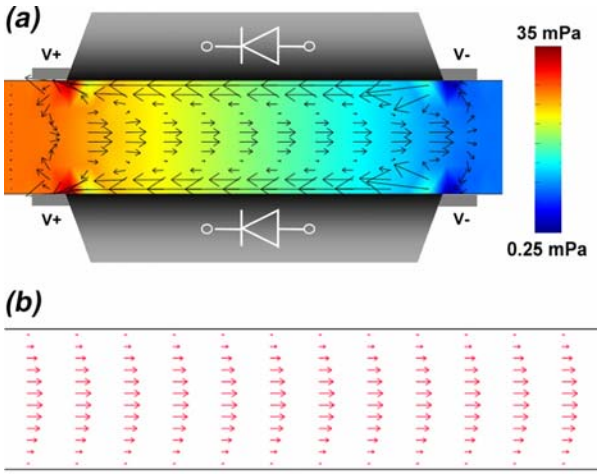

Figure 4.4. Flow simulation for the diode pump in the closed rectangular microchannels with embedded diodes using COMSOL software. (a) Computed velocity profiles between the parallel oriented diodes at the channel walls. The velocity vector magnitudes are represented by the lengths of the arrows. Colours show the pressure. (b) Computed velocity profiles for the fluid flow pumped by the diodes in the middle of longer channel without diodes. The direction of the circular flow in the rectangular loop microchannel is the same as the electroosmotic flow on the diode surfaces. The length of the arrows for the velocity magnitude in (b) is magnified for better visualization.

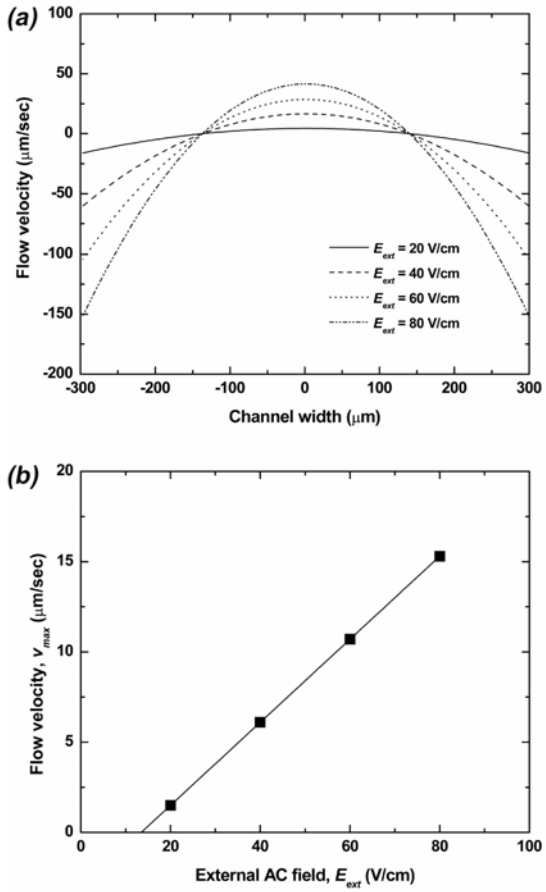

Figure 4.5. Numerical simulations for the diode pumping in the closed rectangular microchannel. (a) Velocity of the reverse electroosmotic flow between two diodes on the channel walls as a function of the channel width. As the external AC field increases, the electroosmotic flux (negative velocity) on the diode surfaces and the backflow (positive velocity) in the middle of the channel become larger, which match well the experimental observations. (b) Velocity of the flow in the centre of the channel loop without the diodes as a function of the external electric field. The simulation data verify the ability of the diodes on the microchannel to pump liquids through the channel with a linear dependence on the AC field. The simulation results show a good correlation with the experimental data and support the electroosmotic pumping mechanism.

The simulation results for the liquid motion in other channel sections confirm the presence of macroscopic circulation through the closed rectangular channel in the direction of the electroosmotic flow on the diode surfaces (Fig. 4.4b). The velocity of the circular flow pumped by the diodes is plotted as a function of the external electric field, based on the results of the numerical calculation in Figure 4.5b. The simulated velocity of the circulation

also shows a linear dependence on the external AC field, in correlation to our experimental measurements, with slightly lower values than the experimental data. This discrepancy of the velocities might come from the restriction of this simulation to 2D domains. Nevertheless, the simulation results are in a good agreement with the experimental data and support the mechanism of pumping driven by the localized electroosmotic flow engendered by the diodes.

4.3.4. Diode Mixing Experimental Results

The flow that developed down the Y-shaped channel in Figure 4.1b was laminar in the absence of AC field and only mixing by molecular diffusion across the interface could occur. When an AC electric field was applied, the two streams between the diodes formed a vortex that led to intensive mixing. The origin of the transverse flow within the diode mixing chamber is schematically shown in Figure 4.6a. The combination of pressure and

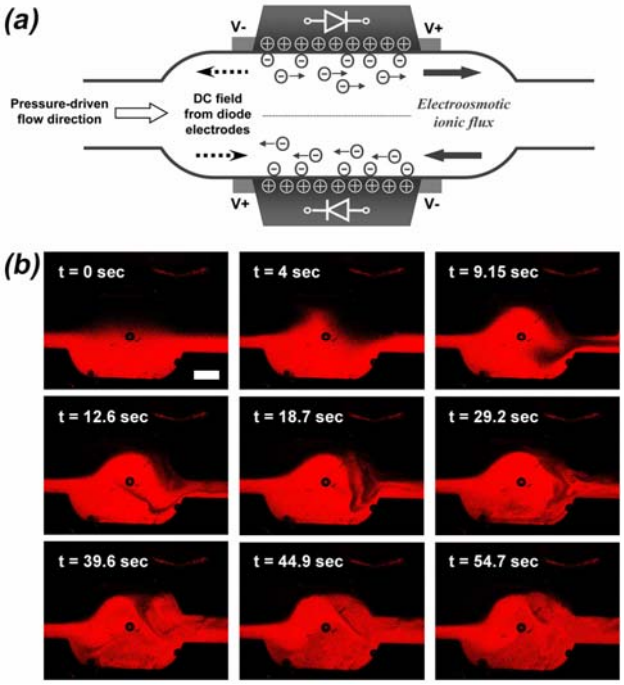

Figure 4.6. Microfluidic mixing in the channel with two oppositely oriented embedded diodes. (a) Schematic of the generation of the localized electroosmotic flow in the diode mixer. Two oppositely directed ionic fluxes on the diode surfaces create crossover flows leading to mixing inside the chamber. The diodes and channel geometry are not to scale. (b) Typical confocal micrographs of the microfluidic flows in the diode mixer, after AC external field was applied through the channel at t = 0. The AC external field applied was 133 V cm^{-1} and 1 kHz. The scale bar in (b) is equal to 500 μm.

electroosmotic flows creates a vortex inside the diode mixer, dramatically improving the mixing efficiency. The active stirring flow led to larger interfacial area between two laminar flows, which reduced the mixing time for a given fluid volume.[9,34] A series of typical confocal microscopic images of fluid motion inside the diode mixer under the AC field is presented in Figure 4.6b.

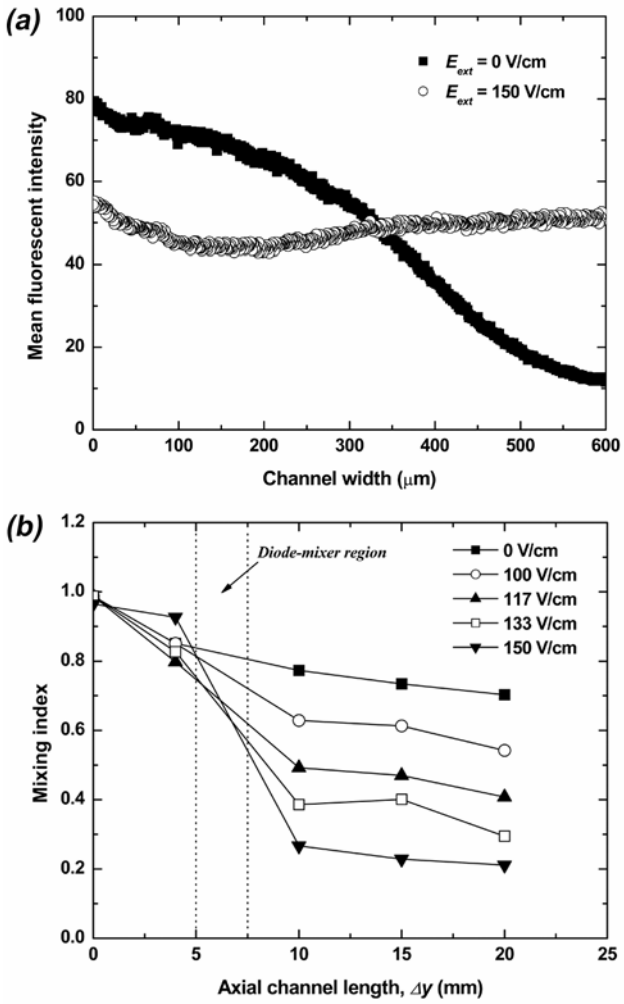

Figure 4.7. (a) Mean fluorescent intensity of the confocal images for the distribution of neutral fluorescent dye in the cross section of the channel at a distance of 2.5 mm from the diode mixer at E_{ext} = 0 V cm^{-1} and 150 V cm^{-1}. (b) Mixing index at different AC fields calculated as a standard deviation of fluorescent intensity in cross sectional confocal images as a function of the distance from the Y-shaped channel junction. All experimental conditions are the same as in Figure 4.6.

The efficiency of the diode mixer was characterized from the confocal micrographs collected in the microchannel downstream of the Y-junction. The channel cross sectional images were converted into gray scale, representing the concentration distributions of the fluorescent dye in the channel. The fluorescence intensities were analyzed using image analysis software supplied with the confocal microscope. The micrographs at a distance of 2.5 mm after the diode mixer showed that two streams in the channel were clearly separated before applying the AC external field, while the red fluorescent color was almost uniformly distributed through the channel under the AC field was turned on. The fluorescent intensity averaged across the channel width obtained from the confocal micrographs confirmed that the vortex flow induced by the diodes increased the mixing of two laminar flows, as shown in Figure 4.7a.

The degree of mixing was evaluated with a mixing index calculated as the standard deviation of the fluorescence intensity in the experimental confocal images,[34]

$$Mixing\,index = \sqrt{\frac{1}{N}\sum\left(\frac{I_k - I_0}{I_0}\right)^2} \tag{4-11}$$

where N is the total number of pixels of a scanned image, I_k is the intensity of a pixel k and I_0 is the average intensity over all pixels in the image. The mixing index is equal to 1 for an unmixed state and 0 for a fully mixed state. The mixing index in the microchannel was plotted as a function of channel length under the different magnitudes of applied AC field (Fig. 4.7b). Increasing the AC field, significantly improved the mixing efficiency within the diode mixer. The two laminar streams showed a level of ~80% mixing at 2.5 mm downstream for the diode mixer under 150 V cm^{-1} of the AC field, while the mixing in the absence of AC field was only ~20%.

The channel length necessary to obtain the same mixing index by pure diffusion only ($Pe \sim 1.2\times10^3$ for the molecular diffusivity of fluorescent dye, $D \sim 10^{-10}$ m^2 s^{-1} from the literature[34,41]), would be $\Delta y_{mix} \sim Pe\ l$ = 68 cm. The experimental data in Figure 4.7b demonstrate nearly complete mixing within 2 cm from the position of the diode mixer. The diode-driven microfluidic mixing is strongly dependent on the overall flow rate through the device. As the pressure-driven flow velocity increased, the mixing efficiency decreased (Fig.

4.8). This is not surprising because at higher flow rates the fluid spends less time in the mixing chamber. The present diode mixer is very effective for laminar flows with low Péclet number ($Pe < 2.2\times10^3$). For comparison, most passive mixers operate well at high Péclet number flows ($Pe > 10^4$).[9,10,41] The diode mixer efficiency can be improved at high flow speeds by fabricating a series of diode mixers on the channel or reducing the channel dimensions. All mixers can be conveniently and rapidly turned on and off remotely, but switching on and off the AC field.

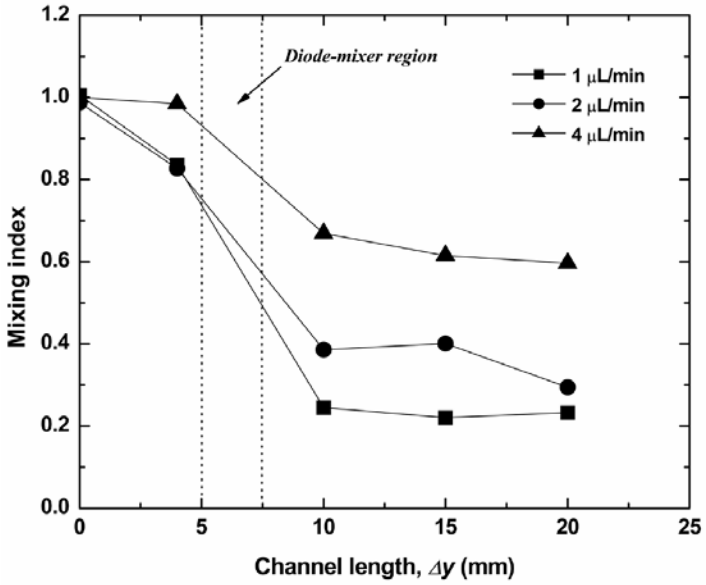

Figure 4.8. Mixing index at various pressure-driven flow rates as a function of the distance from the Y-shaped channel junction. Water and fluorescent dye solution were adjusted to ~ pH 5.4. The AC external field was 133 V cm^{-1} at 1 kHz. As the flow speed was increased, smaller mixing efficiency was observed. Mixing at high flow speeds could be performed with a series of diode mixers in the channel.

4.3.5. Numerical Simulation of Diode Mixing Process

The electroosmotic flow from diodes with opposite orientation leading to the mixing was also studied by numerical simulations using the COMSOL software. The concentration distributions of uncharged species and the flow profiles were calculated in the 2D projection of the microchannel (see Fig. 4.1b). The fluid flow was determined by solving equations (4-

8), (4-9) and (4-10) together and the obtained fluid flow field was then introduced into the convective diffusion equation,

$$\frac{\partial c}{\partial t} + \mathbf{V} \cdot \nabla c = \nabla \cdot (D \nabla c) \tag{4-12}$$

where c is the concentration and D is the diffusion coefficient.

The slip boundary condition on the diode surfaces was also used in the numerical calculations because the thickness scale of the electric double layer is negligible compared to the characteristic length of the Y-shaped channel. The same inflow velocity as the experiment (2 μL min^{-1}) was defined at the two inlets. The electric conditions in the simulations were applied in the same way as in the diode pumping simulations, except for defining the polarity of the rectified electric potential at the diode electrodes in opposite directions. The concentrations at the upper and lower inlets in the simulation domain were assigned as $c = 0$ and $c = 1$, respectively. After a conformal triangular mesh was formed by the software for the domain, the time-dependent solver mode was used.

The simulated concentration distributions and stirring flow profile within the diode mixer at an external AC field of 133 V cm^{-1} are shown in Figure 4.9. The well homogenized solutions flow downstream from the diode mixer (top image of Fig. 4.9a). At early mixing times, transverse fluid components arise at the diode mixer driven by the up-cross flow toward accelerated flow region (bottom images of Fig. 4.9a). The resulting vortex leads to mixing within the diode chamber. The velocity vectors in the diode mixer provide further details of the oppositely directed electroosmotic flows on each diode surface and the convective mass transfer across the interface of the two laminar flows in Figure 4.9b. The images and movies of the experiment and simulation for the mixing are well correlated and confirm that the miniature diodes can significantly enhance the micromixing in a simple device that operates on demand under an external AC field, without any additional moving components or complex channel structures. The mixing efficiency can be increased further by using multiple diodes generating flows with different directions, dimensions and intensities, resulting in chaotic-like flow patterns.

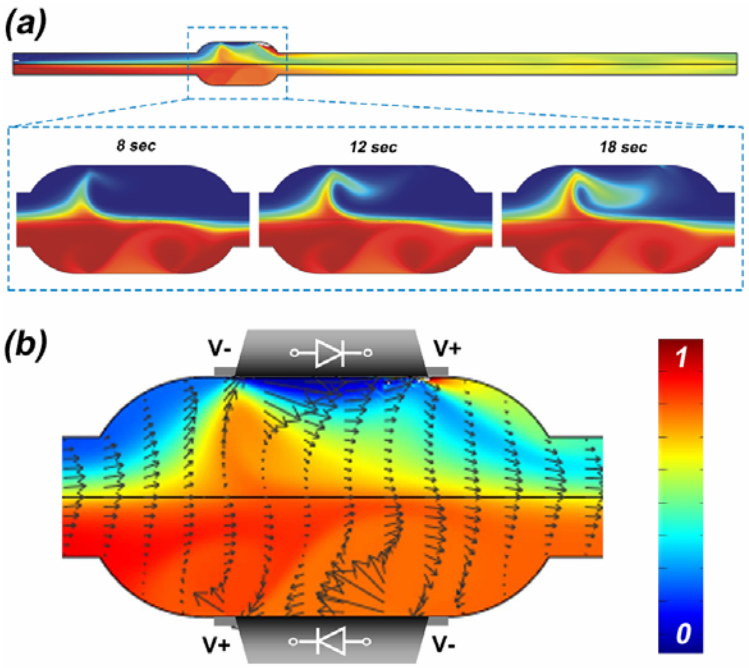

Figure 4.9. Simulations of the mixing process in a microchannel with oppositely oriented diodes. (a) Concentration distribution in the whole microchannel (top). A series of mixing images within the diode chamber after initial times (bottom). (b) Computed steady state flow profile and concentration distribution within the diode mixer at 300 sec. The magnitudes of the velocity vector are represented by the length of the arrows. Colors show the concentration distribution. The results confirm the creation of crossover flows resulting in enhancement of microfluidic mixing.

4.4. Conclusions

The new class of electrohydrodynamic techniques presented here allow manipulation of fluids on the microscale by on-chip integration of microfluidic and electronic components. The results prove that oriented diodes placed at specific locations in a microfluidic network enable facile and controllable pumping or mixing under an external AC field. The theoretical model and the numerical simulations for the electrohydrodynamic flows and material transportation in the microchannel systems were in good agreement with the experimental data. The technique and the results from the theoretical and numerical analysis can be used to design and operate new types of microfluidic chips and μTAS devices for injection, mixing and separation of colloidal particles, proteins, DNA, or cells. The miniature diodes can de used in distributed local pumps and mixers in dynamically reconfigurable chips. They can be

easily combined with detection and analysis components and simultaneously powered by a global AC electric field.

4.5. Acknowledgements

This research was performed in collaboration with Prof. Dimiter Petsev and Erin Beaumont (University of New Mexico, Albuquerque, USA). The authors acknowledge the support of this study from the Defence Advanced Research Projects Agency (DARPA/AFSOR), NSF-CAREER (CTS-0238636), NSF/NIRT (CTS-0404124 and CBET-0609087), NSF/PREM (DMR 0611616) and the Keck Foundation. We thank Yong-Jae Choi and Dr. Tzy-Jiun Mark Luo for access to the plasma cleaner for microchannel fabrication.

4.6. References

[1] Reyes, D. R., Iossifidis, D., Auroux, P-A. and Manz, A., Micro Total Analysis Systems. 1. Introduction, Theory, and Technology. *Anal*. *Chem*. (2002) 74, 2623-2636.

[2] Jakeway, S. C., de Mello, A. J. and Russell, E. L., Miniaturized total analysis systems for biological analysis. *Fresenius J*. *Anal*. *Chem*. (2000) 366, 525-539.

[3] Liu, A-L., He, F-Y., Wang, K., Zhou, T., Lu, Y. and Xia, X-H., Rapid method for design and fabrication of passive micromixers in microfluidic devices using a direct-printing process. *Lab Chip* (2005) 5, 974-978.

[4] Bhatt, K. H., Grego, S. and Velev, O. D., An AC electrokinetic technique for collection and concentration of particles and cells on patterned electrodes. *Langmuir* (2005) 21, 6603-6612.

[5] Whitesides. G. M., The origins and the future of microfluidics. *Nature* (2006) 442, 368-373.

[6] Squires, T. M. and Quake, S. R., Microfluidics: Fluid physics at the nanoliter scale. *Rev*. *Mod*. *Phys*. (2005) 77, 977-1026.

[7] Atencia, J. and Beebe, D. J., Controlled microfluidic interfaces. *Nature* (2005) 437, 648-655.

[8] Nguyen, N-T and Wereley, S. T., *Fundamentals and Applications of Microfluidics*, Artech House, Boston, 2002.

[9] Stroock, A. D., Dertinger, S. K. W., Ajdari, A., Mezić, I., Stone, H. A. and Whitesides, G. M., Chaotic mixer for microchannels. *Science* (2002) 295, 647-651.

[10] Sudarsan, A. P. and Ugaz, V. M., Multivortex micromixing. *Proc*. *Natl Acad*. *Sci*. *USA* (2006) 103, 7228-7233.

[11] Andersson, H., Wijingaart, W., Nilsson, P., Enoksson, P. and Stemme, G., A valve-less diffuser micropump for microfluidic analytical systems. *Sens*. *Actuators B* (2001) 72, 259-265.

[12] Walker, G. M. and Beebe, D. J., A passive pumping method for microfluidic devices. *Lab Chip* (2002) 2, 131-134.

[13] Duffy, D. C., Schueller, O. J. A., Brittain, S. T. and Whitesides, G. M., Rapid prototyping of microfluidic switches in poly(dimethyl siloxane) and their actuation by electroosmotic flow. *J*. *Micromech*. *Microeng*. (1999) 9, 211-217.

[14] Ross, D., Johnson, T. J. and Locascio, L. E., Imaging of electroosmotic flow in plastic microchannels. *Anal*. *Chem*. (2001) 73, 2509-2515.

[15] Chen, C-H. and Santiago, J. G., A planar electroosmotic micropump. *J*. *Microelectromech*. *Syst*. (2002) 11, 672-683.

[16] Burns, M. A., Mastrangelo, C. H., Sammorco, T. S., Man, F. P., Webster, J. R., Johnson, B. N., Foerster, B., Jones, D., Fields, Y., Kaiser, A. R. and Burke, D. T., Microfabricated structures for integrated DNA analysis. *Proc*. *Natl*. *Acad. Sci*. *USA* (1996) 93, 5556-5561.

[17] Kataoka, D. E. and Troian, S. M., Patterning liquid flow on the microscopic scale. *Nature* (1999) 402, 794-797.

[18] Terray, A., Oakey, J. and Marr, D. W. M., Microfluidic control using colloidal devices. *Science* (2002) 296, 1841-1844.

[19] Leach, J., Mushfique, H., Leonardo, R., Padgett. M. and Cooper, J., An optically driven pump for microfluidics. *Lab Chip* (2006) 6, 735-739.

[20] Kline, T. R., Paxton, W. F., Wang, Y., Velegol, D., Mallouk, T. E. and Sen, A., Catalytic micropumps: Microscopic convective fluid flow and pattern formation. *J*. *Am*. *Chem*. *Soc*. (2005) 127, 17150-17151.

[21] Paxton, W. F., Baker, P. T., Kline, T. R., Wang, Y., Mallouk, T. E. and Sen, A., Catalytically induced electrokinetics for motors and micropumps. *J*. *Am*. *Chem*. *Soc*.

(2006) 128, 14881-14888.

[22] Ajdari, A., Pumping liquids using asymmetric electrode arrays. *Phys*. *Rev*. *E* (2000) 61, R45-R48.

[23] Brown, A. B. D., Smith, C. G. and Rennie, A. R., Pumping of water with ac electric fields applied to asymmetric pairs of microelectrodes. *Phys*. *Rev*. *E* (2000) 63, 016305.

[24] Debesset, S., Hayden, C. J., Dalton, C., Eijkel, J. C. T. and Manz, A., An AC electroosmotic micropump for circular chromatographic applications. *Lab Chip* (2004) 4, 396-400.

[25] Studer, V., Pépin, A., Chen, Y. and Ajdari, A., An integrated AC electrokinetic pump in a microfluidic loop for fast and tunable flow control. *Analyst* (2004) 129, 944-949.

[26] Bazant, M. Z. and Squires, T. M., Induced-charge electrokinetic phenomena: Theory and microfluidic applications. *Phys*. *Rev*. *Lett*. (2004) 92, 066101.

[27] Bazant, M. Z. and Ben, Y., Theoretical prediction of fast 3D AC electroosmotic pumps. *Lab Chip* (2006) 6, 1455-1461.

[28] Rodríguez, I. and Chandrasekhar, N., Experimental study and numerical estimation of current changes in electroosmotically pumped microfluidic devices. *Electrophoresis* (2005) 26, 1114-1121.

[29] Schwesinger, N., Frank, T. and Wurmus, H., A modular microfluid system with an integrated micromixer. *J*. *Micromech*. *Microeng*. (1996) 6, 99-102.

[30] Hong, C-C., Choi, J-W. and Ahn, C. H., A novel in-plane passive microfluidic mixer with modified Tesla structures. *Lab Chip* (2004) 4, 109-113.

[31] Liu, R. H., Stremler, M. A., Sharp, K. V., Olsen, M. G., Santiago, J. G., Adrian, R. J., Aref, H. and Beebe, D. J., Passive mixing in a three-dimensional serpentine microchannel. *J*. *Microelectromech*. *Syst*. (2000) 9, 190-197.

[32] Kim, D-S., Lee, S-H., Kwon, T-H. and Ahn, C. H., A serpentine laminating micromixer combining splitting/recombination and advection. *Lab Chip* (2005) 5, 739-747.

[33] Sudarsan, A. P. and Ugaz, V. M., Fluid mixing in planar spiral microchannels. *Lab Chip* (2006) 6, 74-82.

[34] Ryu, K. S., Shaikh, K., Goluch, E., Fan, Z. and Liu, C., Micro magnetic stir-bar mixer integrated with parylene microfluidic channels. *Lab Chip* (2004) 4, 608-613.

[35] Rife, J. C., Bell, M. I., Horwitz, J. S., Kabler, M. N., Auyeung, R. C. Y. and Kim, W. J., Miniature valveless ultrasonic pumps and mixers. *Sens*. *Actuators A* (2000) 86, 135-140.

[36] Paik, P., Pamula, V. K. and Fair, R. B., Electrowetting-based droplet mixers for microfluidic systems. *Lab Chip* (2003) 3, 253-259.

[37] Mugele, F., Baret, J. C. and Steinhauser, D., Microfluidic mixing through electrowetting-induced droplet oscillations. *Appl*. *Phys*. *Lett*. (2006) 88, 204106.

[38] Strook, A. D., Weck, M., Chiu, D. T., Huck, W. T. S., Kenis, P. J. A., Ismagilov, R. F. and Whitesides, G. M., Patterning electroosmotic flow with patterned surface charge. *Phys*. *Rev*. *Lett*. (2000) 84, 3314-3317.

[39] Erickson, D. and Li, D., Influence of surface heterogeneity on electrokinetically driven microfluidic mixing. *Langmuir* (2002) 18, 1883-1892.

[40] Chen, J-K. and Yang, R-J., Electroosmotic flow mixing in zigzag microchannels. *Electrophoresis* (2007) 28, 975-983.

[41] Sasaki, N., Kitamori, T. and Kim, H-B., AC electroosmotic micromixer for chemical processing in a microchannel. *Lab Chip* (2006) 6, 550-554.

[42] Oddy, M. H., Santiago, J. G. and Mikkelsen, J. C., Electrokinetic instability micromixing. *Anal*. *Chem*. (2001) 73, 5822-5832.

[43] Moctar, A. O. E., Aubry, N. and Batton, J., Electro-hydrodynamic micro-fluidic mixer. *Lab Chip* (2003) 3, 273-280.

[44] Chang, S. T., Paunov, V. N., Petsev, D. N. and Velev, O. D., Remotely powered self-propelling particles and micropumps based on miniature diodes. *Nat*. *Mater*. (2007) 6, 235-240.

[45] Streetman, B. G., *Solid State Electronic Devices*, Prentice Hall, New Jersey, 1990.

[46] Hunter, R. J., *Foundations of Colloid Science*, Oxford Univ. Press, New York, 2001.

[47] Duffy, D. C., McDonald, J. C., Schueller, O. J. A. and Whitesides, G. M., Rapid prototyping of microfluidic systems in poly(dimethylsiloxane). *Anal*. *Chem*. (1998) 70, 4974-4984.

[48] McDonald, J. C., Duffy, D. C., Anderson, J. R., Chiu, D. T., Wu, H., Schueller, O. J. A. and Whitesides, G. M., Fabrication of microfluidic systems in poly(dimethylsiloxane). *Electrophoresis* (2000) 21, 27-40.

[49] Dutta, P. and Beskok, A., Analytical solution of combined electroosmotic/pressure driven flows in two-dimensional straight channels: Finite Debye layer effects. *Anal. Chem*. (2001) 73, 1979-1986.

[50] Hunter, R. J., *Zeta Potential in Colloid Science: Principles and Applications*, Academic Press, London, 1981.

[51] Reppert, P. M. and Morgan, F. D., Frequency-dependent electroosmosis. *J. Colloid Interface Sci*. (2002) 254, 372-383.

[52] Bird, R. B., Stewart, W. E. and Lightfoot, E. N., *Transport Phenomena*, John Wiley & Sons, Inc., New York, 2002.

[53] Shah, R. K. and London, A. L., *Laminar Flow Forced Convection in Ducts*, Academic Press, London, 1979.

[54] Walker, G. M., *Encyclopedia of Medical Devices and Instruments*, Webster, J. G., Ed., Wiley, Hoboken, 2006.

[55] Velev, O. D. and Bhatt, K. H., On-chip micromanipulation and assembly of colloidal particles by electric fields. *Soft Matter*. (2006) 2, 738-750.

Chapter 5

Materials of Controlled Shape and Stiffness with Photocurable Microfluidic Endoskeleton*

* Partially based on Chang, Uçar, Swindlehurst, Bradley, Renk and Velev, 2008, submitted.

5.1. Introduction

Development of microfluidic systems has been a focus of intense research in the chemical and biological sciences due to their promising advantages, such as fast analysis times on small sample sizes, high resolution and sensitivity for detections, easy automation and integration with sample pre-treatment and detection systems in a single chip.[1-5] Microfluidics has already revolutionized some aspects of biosensing/assay,[6-10] chemical reactions,[4,11-13] and colloidal particle synthesis.[14-18] The potential of microfluidics in other areas of technology has only begun to be realized and investigated very recently. A few research groups have shown the use of microfluidic technology for optofluidic devices by large refractive index contrast of liquid/liquid or liquid/air cladding through the microchannel,[19-22] information coding/decoding and logic gate by the control of streams of droplets and fluorescent molecules,[23-25] fabrication of 3D metallic microstructures by filling liquid solder into the microchannel, called 'microsolidics',[26] and electronic paper based on electrowetting.[27] One of the most promising, yet largely unexplored, areas is the fabrication of materials with embedded microchannel networks, where the flow, pressure, temperature, color and other properties of the liquid inside the channels impart a certain function to the matrix material in which the network is embedded. Majumder *et al.* have shown that viscous liquid-filled microchannels in thin elastomeric polydimethylsiloxane (PDMS) layer rendered significant enhancement of adhesion, resulting from the crack-arresting properties of microchannels and the surface stresses caused by capillary force.[28,29] This simple microfluidic technique can create the reusable strong adhesive layers without sticky materials and complex surface patterns. Toohey *et al.* demonstrated the use of 3D microvascular networks for a self-healing system, which is inspired by the functionality of natural skin derived from its vesicular blood microfluidic networks.[30] This self-healing material is capable of multiple healing cycles by continuous delivery of healing agents through the 3D microvasscular network embedded in the substrate.

We report here new microfluidic materials in the form of flexible sheets that can be solidified on demand to acquire specific shapes. They are based on microfluidic channel networks in thin PDMS layer filled with photocurable polymers. The materials formed in this

way possess a few unique features, the most notable being the ability to adopt and retain a certain user-defined shape. When the microchannel networks are deformed and exposed by UV light, the photoresist inside the channels is solidified and acts as endoskeleton within the PDMS layer, acquiring the programmed shape. The bending and stretching moduli of the materials with solidified endoskeleton increase drastically and once the external force is removed, the "memorized" shapes are recovered. The permanent preservation of the shape of solidified microfluidic sheets could be used in making instant packages and supports on demand, creating "exoskeletons" for delicate package contents and multiple other applications.

5.2. Experimental Section

5.2.1. Preparation of Photocurable Microfluidic Materials

Channel masters were created by coating SU-8 2050 photoresist (MicroChem, Inc.) on a silicon wafer to a thickness from 150 μm to 450 μm using a spin-coater (Model P6700, Specialty Coating Systems, Inc.). The transparency photomasks containing channel designs with a 400 μm of channel width were brought into contact with the SU-8 photoresist followed by a UV exposure (Model B-100A, BLAK-RAY). After post-baking, the UV exposed wafers were treated in SU-8 developer solution (MicroChem, Inc.) and hard-baked. The remaining steps for fabricating the shape-controlled microchannel materials are shown in Figure 5.1. The PDMS precursor (Sylgard 184, Dow Corning) was cast on the channel masters and cured at 70 °C. After peeling off the PDMS layers, two holes were punched at each end of the channel using a blunt 16 gauge needle to inject the photo-curable polymers. Two PDMS layers with embedded channels were sealed to each other with orthogonal orientation of the channels using air-plasma treatment (Model PDC-32G, Harrick Plasma). Liquid SU-8 50 photoresist (MicroChem, Inc.) was injected into the microchannel on a hot-plate (55 °C) using a syringe. The holes punched in the replicas were closed with PDMS prepolymer and cured at 70 °C. The resulting microfluidic layers had a length of 36 mm, a width of 24 mm, and a height of 1.6 ~ 2.0 mm. The photocurable microfluidic materials were

deformed with a variety of shapes and exposed to UV light for 15 min to solidify the liquid SU-8 photoresist inside the microchannel networks.

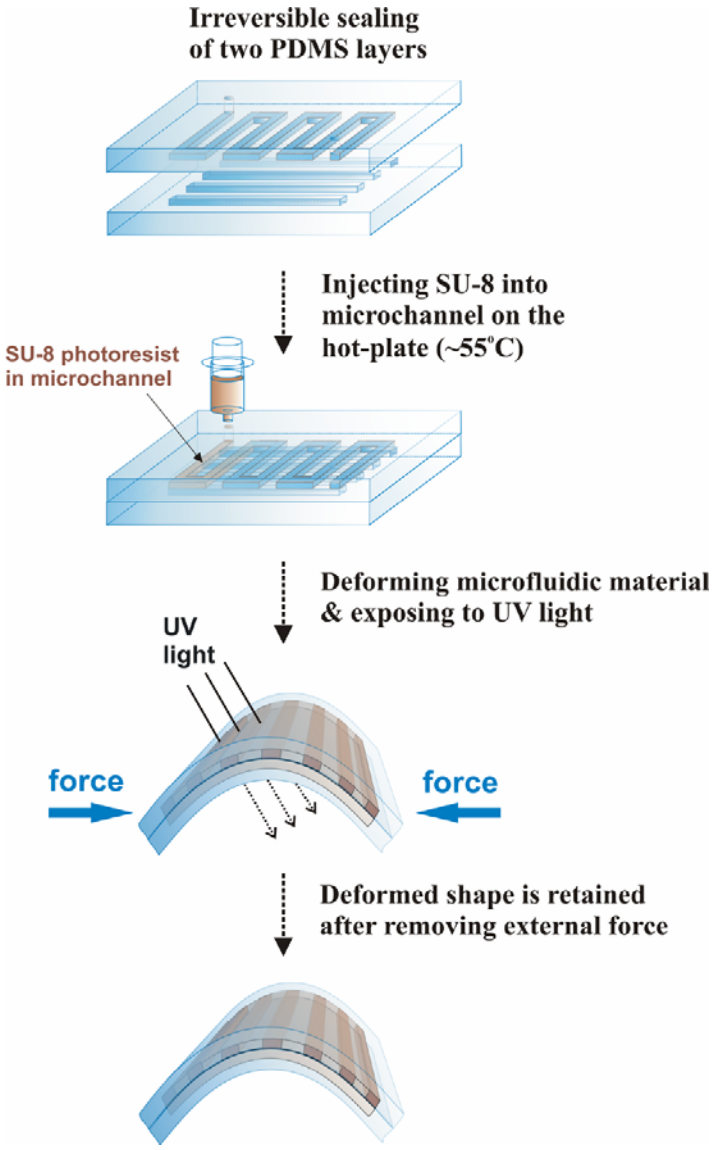

Figure 5.1. Fabrication of photocurable microfluidic endoskeleton structure by filling epoxy-based SU-8 photopolymer into microfluidic channel network. After UV exposure, SU-8 photoresist within deformed channel network is solidified and original deformation of photocurable microfluidic network is retained, even after external force is removed.

5.2.2. Measurement of Tensile and Bending Moduli

For a tensile test, the microfluidic materials were cured under the UV exposure for 15 min without the deformations. The tensile tests were performed using a MTS tensile tester (Model MTS 30G). The crosshead speed was 25 mm min^{-1}. Tinius Olsen Stiffness tester (Tinius Olsen, Inc.) was used for the measurement of a bending modulus. One end of the photocured microfluidic materials were placed at the sample holder. A controlled load was applied steadily at the other free end of the samples tested by a motor drive. The applied load and the resulting angle of bending were measured from circular scales in the tester.

5.3. Results and Discussion

5.3.1. Controlled Shapes on Demand

The procedure for fabrication of shape-controlled microchannel networks is shown schematically in Figure 5.1. The microfluidic channels inside PDMS were fabricated using soft lithography.[31,32] Two PDMS layers with embedded channels were irreversibly sealed to each other with orthogonal orientation by air-plasma treatment (Fig. 5.2). Liquid SU-8 (photocurable epoxy resin) was injected into the microchannel network using a syringe. The filling was done on a hot plate to lower viscosity and improve SU-8 wettability to PDMS.

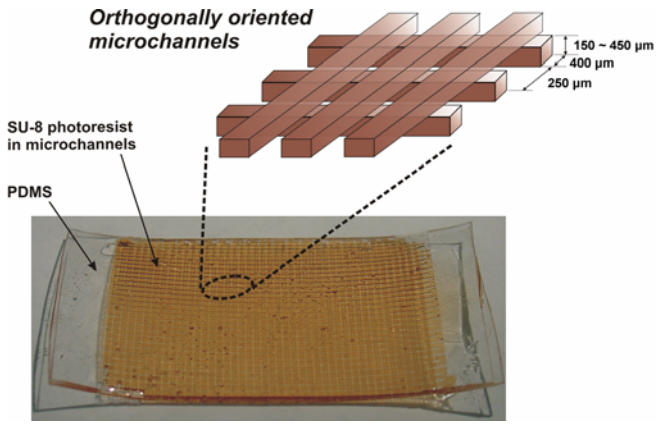

Figure 5.2. Orthogonally oriented microchannel structure embedded within PDMS matrix. The channel width and interchannel distance were ca. 400 µm and ca. 250 µm, respectively. The channel thickness was varied from 150 µm to 450 µm. The microfluidic network in PDMS had a length of 36 mm and a width of 24 mm. The channels in schematic are not to scale.

The elastomer sheets with microchannel networks filled with SU-8 prepolymer are transparent, soft and easily bent, similarly to the original silicon rubber (Fig. 5.3a). The material filled with liquid SU-8 could be deformed with a variety of shapes, e.g. wavy, spiral, saddle, pocket, and then solidified by exposing to UV light for 15 min. The transparent PDMS layer can transmit incident light in near UV region (350 ~ 400 nm), where SU-8 photopolymer is solidified. The resulting PDMS slabs after the UV exposure retained the defined deformation, yet remained still soft and rubber-like on the surface (Figs. 5.3b-d). This photo-cured microfluidic network in the PDMS can be stretched, bent or twisted manually with high recoverable strain.

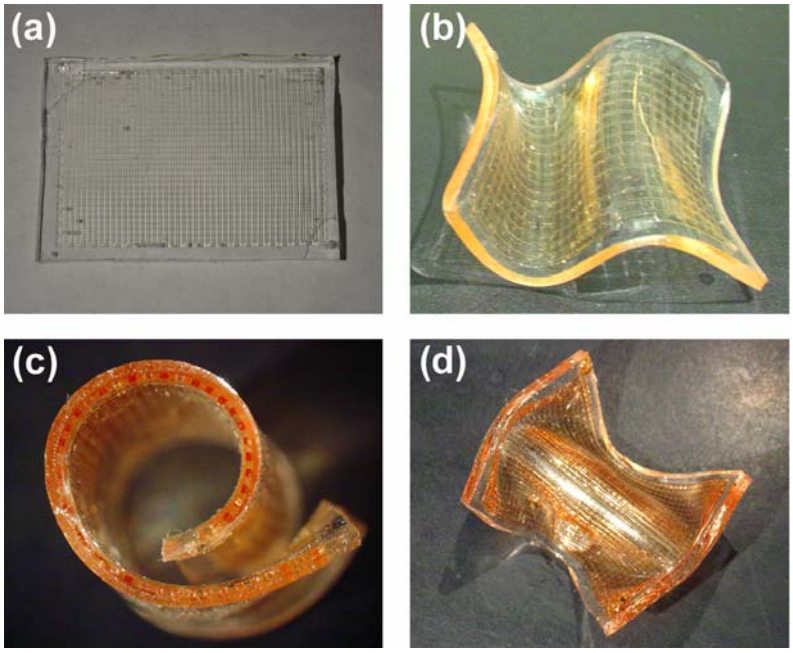

Figure 5.3. Photographs of photocurable microfluidic PDMS sheets with embedded microfluidic endoskeleton. (a) A microfluidic material filled with liquid SU-8 photopolymer before UV exposure. After deforming the shape and exposing it to UV light for 15 min, photocured microfluidic composites with solidified SU-8 photoresist can retain the defined shapes, such as (b) wavy, (c) spiral, and (d) saddle. The microfluidic materials were 36 mm long and 24 mm wide. The microchannels embedded in PDMS layers were 400 μm wide and 450 μm thick in (a); 800 μm wide and 165 μm thick in (b); 400 μm wide and 275 μm thick in (c); 400 μm wide and 450 μm thick in (d).

5.3.2. Improvement of Elastic and Bending Moduli

SU-8 photoresist has good mechanical properties, which enable this material to provide reliable replication and reinforcement for sophisticated microstructures.[34-36] Elastic modulus of SU-8 is 4400 MPa after complete cross-linking[34,37] and PDMS has 0.75 MPa of the elastic modulus.[34] Thus, solidification of the SU-8 prepolymer in the microchannel significantly increased the elastic modulus of the PDMS layer, which became much stiffer than the PDMS-only layers. The elastic moduli of the photocurable microfluidic materials with various volume fractions of SU-8 photoresist were measured from tension tests using a computer-controlled MTS mechanical testing system. Typical stress-strain curves for photocured microfluidic endoskeleton structures with various volume fraction of SU-8 photoresist are plotted in Figure 5.4a. Pronounced improvements of the tensile stress of the microfluidic elastomeric layers were observed after the solidification of SU-8 in the channel. Due to its structural similarity to woven composite materials, the tensile stress response of our microfluidic composite showed three phases in stress-strain curves before complete failure, which is typical characteristic of 3D woven composite materials.[38,39] The tensile stress at the initial region, called elastic phase, showed linear increase up to a strain of ca. 0.6 % and was followed by hardening phase, where a non-linear loading response occurred. Rupture of the solidified SU-8 photoresist in the microchannels parallel to the load direction between the orthogonal channel junctions led to the primary load drop. After the sudden, large load reduction, the photocured microfluidic composites experienced large strain displacements until the complete break at the orthogonal channel junctions. This large displacements were caused by stretching of the PDMS matrix around the failed SU-8 photoresist in the microchannel network. Although there is a variation of tensile strength and failure strain from the samples tested, those main characteristic of the stress-strain curve was consistent in the tensile test of the photocured microfluidic materials.

The elastic moduli of the photocured microfluidic composites were obtained from the slopes of initial elastic regime in the stress-strain curves and compared with the moduli of PDMS-only and non-cured materials (Fig. 5.4b). The microfluidic structures filled with liquid SU-8 had similar elastic modulus to the pure PDMS layer. However, the solidification

of SU-8 prepolymer in the microchannel network enhanced dramatically the elastic modulus of the microfluidic composite material, showing linear increment of the modulus with a volume fraction of SU-8 in the PDMS layers – about 40 times higher than that of the pure PDMS layer at about 20 % volume of SU-8 photoresist.

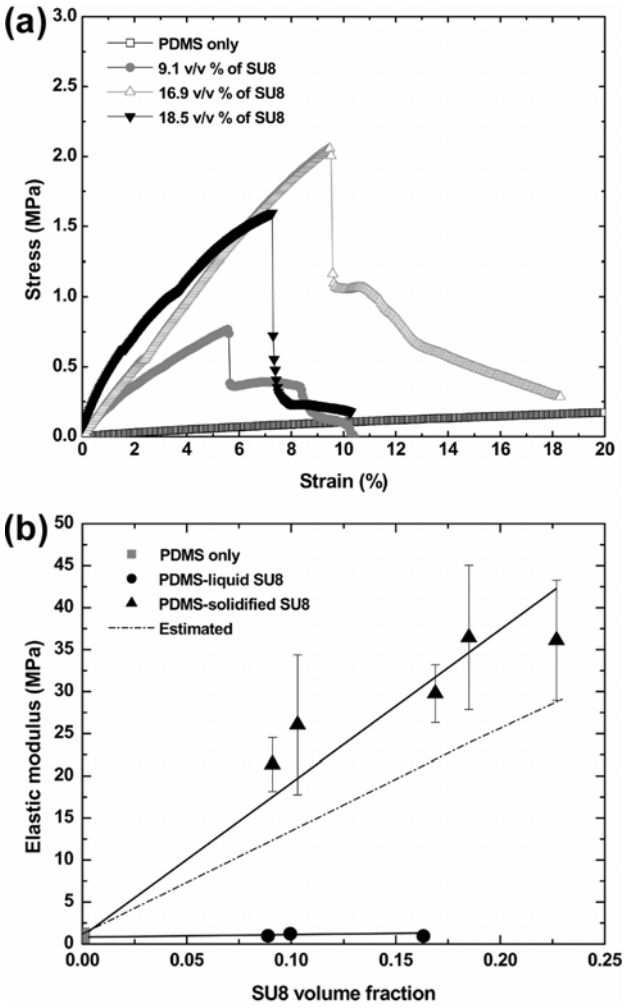

Figure 5.4. (a) Typical stress-strain curves from tensile tests for PDMS-only layer and photocured microfluidic endoskeleton structures containing different loading of SU-8 photoresist in microchannels. (b) Elastic modulus of PDMS-only layer and photocurable microfluidic networks before and after UV exposure as a function of volume fraction of SU-8 photoresist in PDMS matrix. The modulus of elasticity was obtained from initial linear region of stress-strain curves in (a). The solid lines were plotted by least square function. The dot-dash line was plotted by the estimated values with equation (5-3).

The photocurable microfluidic endoskeleton structures in this study can be considered as a unidirectional composite material, because the solidified SU-8 photoresist in the microchannels is uniform in cross-sectional area, parallel, and continuous throughout the PDMS matrix. For the unidirectional composite materials, the modulus of elasticity is predicted by rule of mixtures equations, expressed by elastic modulus and volume fraction of each component in the composite. The unidirectinal composite shows different tensile behaviors depending on the orientation of stiffer materials in a matrix to tensile loading direction. When the stiffer materials are aligned in parallel to the loading direction, the elastic modulus of composites is generalized by longitudinal tensile modulus (E_{CL}). For a load at the right angle to the stiffer materials, transverse tensile modulus (E_{CT}) stands for modulus of elasticity of the unidirectional composites,[33]

$$E_{CL} = \sum_{i=1}^{n} E_i V_i \tag{5-1}$$

$$E_{CT} = \frac{1}{\sum_{i=1}^{n} (V_i / E_i)} \tag{5-2}$$

where E_i and V_i are the elastic modulus and the volume fraction of component i in the composite, respectively. During the tensile loading, the elastic modulus (E_C) of the photocured microfluidic material is influenced by both longitudinal and transverse elastic moduli, due to the orthogonal microchannel structure in the PDMS matrix (Fig. 5.2). This can be estimated by[38,39]

$$E_C \approx f_S E_{CL} + (1 - f_S) E_{CT} \tag{5-3}$$

where f_S is the volume fraction of solidified SU-8 photoresist that is aligned to the loading direction. As the microchannels at top and bottom layers of PDMS in the photocurable microfluidic material are designed to have the same volume, the value of f_S is 0.5. The elastic moduli of solidified SU-8 photoresist without soft or post bakes and PDMS layer were measured as ca. 205 MPa and 1.2 MPa, respectively. After inserting these values in equations (5-1), (5-2) and (5-3), the elastic modulus of the photocured microfluidic material was calculated and plotted as a function of the volume fraction of SU-8 in Figure 5.4b. This estimate of the elastic modulus is in a reasonable agreement with the modulus measured in

the elastic regime, although the modulus estimated has slightly lower modulus than the experimental data. This small difference of the elastic modulus might come from the contribution of the solidified SU-8 photoresists at the junctions of orthogonally oriented microchannels to the elastic modulus in the experiments. Nevertheless, the estimation results demonstrate that the solidification of SU-8 photoresist within the microchannels drastically improves the stiffness of the elastomeric microfluidic materials.

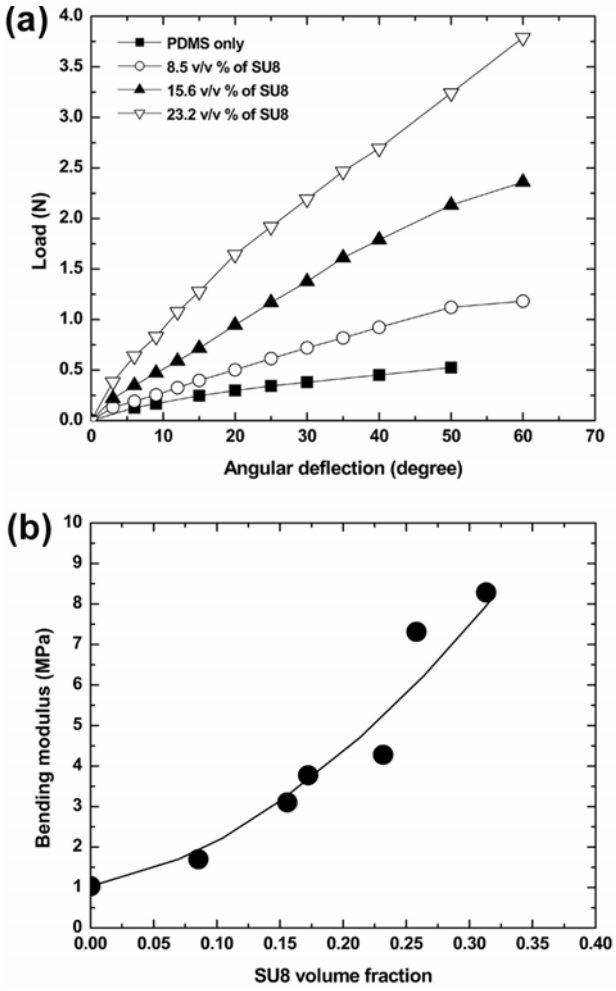

Figure 5.5. (a) Load-angular deflection curves in bending tests for PDMS-only layer and photocured microfluidic endoskeleton structures containing different amount of SU-8 photoresist in microchannels. (b) Bending modulus of PDMS-only layer and photocurable microfluidic networks after UV exposure as a function of volume fraction of SU-8 photoresist in PDMS matrix. The bending modulus was obtained from initial linear region of load-angular deflection curves in (a) using equation (5-4). The line in (b) is a guide to the eye.

The modulus of bending elasticity of the photocured microfluidic network was measured by Tinius-Olsen stiffness tester. Typical load-angular deflection curves of the photocured microfluidic materials with various volume fraction of SU-8 photoresist in the PDMS matrix are shown in Figure 5.5a. In order to produce the same angular deflection, higher force had to be applied to the microfluidic materials with larger amount of the solidified SU-8 photoresist. The bending modulus (E_B) of the photocurable microfluidic structure was calculated from the slope of the initial straight line of the moment-angular deflection curve (m) according to[40,41]

$$E_B = \frac{4 S m}{w d^3} \tag{5-4}$$

where S is span length measured from the center of rotation of pendulum weighing system to the contact edge of the bending plate, w and d are the width and depth of test sample, respectively. As similar to the tensile test, the photo-cured microfluidic endoskeleton structure had higher bending modulus with larger volume fraction of SU-8 photoresist in the PDMS layer, becoming stiffer and more recoverable (Fig. 5.5b). Bending strength of the photocured microfluidic materials was not measured because most did not break under the loading conditions in this measurement. The network of solidified SU-8 photoresist can impart strong rigidity to the elastomeric polymer matrix in order to retain the deformed shapes with high recoverable strain.

5.4. Conclusions

In summary, we demonstrated that the introduction of SU-8 photoresist in the microfluidic endoskeleton of normally flexible PDMS layers can provide high strain storage and recovery. The material inside the microchannel network can be replaced with other shape-memory polymers, which can retain shape and develop strain by applying external stimuli such as heat, electric or magnetic field. The mechanical properties of the photocurable microfluidic networks could be improved with truss or other 3D microchannel structures in a matrix of PDMS or by adding microfibers to the photopolymer filling in the microchannels. The

fabrication process of the shape-controlled microfluidic endoskeleton materials that we report here could be simple and scalable.

5.5. Acknowledgements

The authors acknowledge the support of this study from MeadWestvaco Cooperation. We thank Yong-Jae Choi and Dr. Tzy-Jiun Mark Luo for access to the plasma cleaner for microchannel fabrication. We are grateful to Arjun Krishnan, Dr. Tushar K. Ghosh, and Dr. Jan E. Pegram for acess to MTS tensile tester and Tinius-Olsen Stiffness tester. The authors thank Dr. Sejong Kim for helpful discussions.

5.6. References

[1] Squires, T. M. and Quake, S. R., Microfluidics: Fluid physics at the nanoliter scale. *Rev. Mod. Phys.* (2005) 77, 977-1026.

[2] Whitesides, G. M. and Stroock, A. D., Flexible methods for microfluidics. *Phys. Today* (2001) 54, 42-47.

[3] Whiteside, G. M., The origins and the future of microfluidics. *Nature* (2006) 442, 368-373.

[4] deMello, A. J., Control and detection of chemical reactions in microfluidic systems. *Nature* (2006) 442, 394-402.

[5] Chang, S. T., Beaumont, E., Petsev, D. N. and Velev, O. D., Remotely powered distributed microfluidic pumps and mixers based on miniature diodes. *Lab Chip* (2008) 8, 117-124.

[6] Sanders, G. H. W. and Manz, A., Chip-based microsystems for genomic and proteomic analysis. *Trends Anal. Chem.* (2000) 19, 364-378.

[7] Delamarche, E., Juncker, D. and Schmid, H., Microfluidics for processing surfaces and miniaturizing biological assays. *Adv. Mater.* (2005) 17, 2911-2933.

[8] El-Ali, J., Sorger, P. K. and Jensen, K. F., Cells on chips. *Nature* (2006) 442, 403-411.

[9] Shaikh, K. A., Ryu, K. S., Goluch, E. D., Nam, J-M., Liu, J., Thaxton, C. S., Chiesl, T. N., Barron, A. E., Lu, Y., Mirkin, C. A. and Liu, C., A modular microfluidic

architecture for integrated biochemical analysis. *Proc. Natl. Acad. Sci. USA* (2005) 102, 9745-9750.

[10] Ottesen, E. A., Hong, J. W., Quake, S. R. and Leadbetter, J. R., Microfluidic digital PCR enables multigene analysis of individual environmental bacteria. *Science* (2006) 314, 1464-1467.

[11] Song, H., Tice, J. D. and Ismagilov, R. F., A microfluidic system for controlling reaction networks in time. *Angew. Chem. Int. Ed.* (2003) 42, 768-772.

[12] Kobayashi, J., Mori, Y., Okamoto, K., Akiyama, R., Ueno, M., Kitamori, T. and Kobayashi, S., A microfluidic device for conducting gas-liquid-solid hydrogenation reactions. *Science* (2004) 304, 1305-1308.

[13] Murphy, E. R., Martinelli, J. R., Zaborenko, N., Buchwald, S. L. and Jensen, K. F., Accelerating reactions with microreactors at elevated temperatures and pressures: Profiling aminocarbonylation reactions. *Angew. Chem. Int. Ed.* (2007) 46, 1734-1737.

[14] Millman, J. R., Bhatt, K. H., Prevo, B. G. and Velev, O. D., Anisotropic particle synthesis in dielectrophoretically controlled microdroplet reactors. *Nat. Mater.* (2004) 4, 98-102.

[15] Dendukuri, D., Pregibon, D. C., Collins, J., Hatton, T. A. and Doyle, P. S., Continuous-flow lithography for high-throughput microparticle synthesis. *Nat. Mater.* (2006) 5, 365-369.

[16] Nie, Z., Li, W., Seo, M., Xu, S. and Kumacheva, E., Janus and ternary particles generated by microfluidic synthesis: Design, synthesis, and self-assembly. *J. Am. Chem. Soc.* (2006) 128, 9408-9412.

[17] Lee, D. and Weitz, D. A., Double emulsion-templated nanoparticle colloidosomes with selective permeability. *Adv. Mater.* (2008) 20, 3498-3503.

[18] Karnik, R., Gu, F., Basto, P., Cannizzaro, C., Dean, L., Kyei-Manu, W., Langer, R. and Farokhzad, O. C., Microfluidic platform for controlled synthesis of polymeric nanoparticles. *Nano Lett.* (2008) 8, 2906-2912.

[19] Wolfe, D. B., Conroy, R. S., Garstecki, P., Mayers, B. T., Fischbach, M. A., Paul, K. E., Prentiss, M. and Whitesides, G. M., Dynamic control of liquid-core/liquid-cladding optical waveguides. *Proc. Natl. Acad. Sci. USA* (2004) 101, 12434-12438.

[20] Vezenov, D. V., Mayers, B. T., Conroy, R. S., Whitesides, G. M., Snee, P. T., Chan,

Y., Nocera, D. G. and Bawendi, M. G., A low-threshold, high-efficiency microfluidic waveguide laser. *J. Am. Chem. Soc.* (2005) 127, 8952-8953.

[21] Psaltis, D., Quake, S. R. and Yang, C., Developing optofluidic technology through the fusion of microfluidics and optics. *Nature* (2006) 442, 381-386.

[22] Lim, J-M., Kim, S-H., Choi, J-H. and Yang, S-M., Fluorescent liquid-core/air-cladding waveguides towards integrated optofluidic light sources. *Lab Chip* (2008) 8, 1580-1585.

[23] Fuerstman, M. J., Garstecki, P. and Whitesides, G. M., Coding/decoding and reversibility of droplet trains in microfluidic networks. *Science* (2007) 315, 828-832.

[24] Prakash, M. and Gershenfeld, N., Microfluidic bubble logic. *Science* (2007) 315, 832-835.

[25] Kim, S., Lee, H. N., van Noort, D., Swamy, K. M. K., Kim, S. H., Soh, J. H., Lee, K-M., Nam, S-W., Yoon, J. and Park, S., Fluorescent molecular logic gates using microfluidic devices. *Angew. Chem. Int. Ed.* (2008) 47, 872-876.

[26] Siegel, A. C., Bruzewicz, D. A., Weibel, D. B. and Whitesides, G. M., Microsolidics: Fabrication of three-dimensional metallic microstructures in poly(dimethylsiloxane). *Adv. Mater.* (2007) 19, 727-733.

[27] Hayes, R. A. and Feenstra, B. J., Video-speed electronic paper based on electrowetting. *Nature* (2003) 425, 383-385.

[28] Verma, M. K. S., Majumder, A. and Ghatak, A., Embedded template-assisted fabrication of complex microchannels in PDMS and design of a microfluidic adhesive. *Langmuir* (2006) 22, 10291-10295.

[29] Majumder, A., Ghatak, A. and Sharma, A., Microfluidic adhesion induced by subsurface microstructures. *Science* **2007**, 318, 258-261.

[30] Toohey, K. S., Sottos, N. R., Lewis, J. A., Moore, J. S. and White, S. R., Self-healing materials with microvascular networks. *Nat. Mater.* (2007) 6, 581-585.

[31] Duffy, D. C., McDonald, J. C., Schueller, O. J. A. and Whitesides, G. M., Rapid prototyping of microfluidic systems in poly(dimethylsiloxane). *Anal. Chem*. (1998) 70, 4974-4984.

[32] McDonald, J. C., Duffy, D. C., Anderson, J. R., Chiu, D. T., Wu, H., Schueller, O. J. A. and Whitesides, G. M., Fabrication of microfluidic systems in

poly(dimethylsiloxane). *Electrophoresis* **2000**, 21, 27-40.

[33] Agarwal, B. D. and Broutman, L. J., *Analysis and performance of fiber composites*, John Wiley & Sons, New York, 1990, p 54-120.

[34] Govindaraju, A., Chakraborty, A. and Luo, C., Reinforcement of PDMS masters using SU-8 truss structures. *J. Micromech. Microeng.* (2005) 15, 1303-1309.

[35] Lorenz, H., Despont, M., Fahrni, N., LaBianca, N., Renaud, P. and Vettiger, P., SU-8: a low-cost negative resist for MEMS. *J. Micromech. Microeng.* (1997) 7, 121-124.

[36] Gao, H., Liu, Z., Zhang, G. and Xie, G., Precise replication of antireflective nanostructures from biotemplates. *Appl. Phys. Lett.* (2007) 90, 123115.

[37] Feng, R. and Farris, R. J., Influence of processing conditions on the thermal and mechanical properties of SU8 negative photoresist coatings. *J. Micromech. Microeng.* (2003) 13, 80-88.

[38] Cox, B. N., Dadkhah, M. S. and Morris, W. L., On the tensile failure of 3D woven composites. *Composites Part A* **1996**, 27A, 447-458.

[39] Callus, P. J., Mouritz, A. P., Bannister, M. K. and Leong, K. H., Tensile properties and failure mechanisms of 3D woven GRP composites. *Composites Part A* (1999) 30, 1277-1287.

[40] Manual of Tinius-Olsen Stiffness tester, Tinius Olsen, Inc.

[41] Brantley, W. A., Augat, W. S., Myers, C. L. and Winders, R. V., Bending deformation studies of orthodontic wires. *J. Dent. Res.* (1978) 57, 609-615.

Chapter 6

Polyelectrolyte Diodes: Nonlinear Current Response of a Junction between Aqueous Ionic Gels*

* Partially based on Cayre, Chang, and Velev, *J. Am. Chem. Soc.*, 2007, 129, 10801-10806.

6.1. Introduction

Silicon and other inorganic semiconductors are the predominant materials in electronic manufacturing today; however, the development of organic-based electronic components has been a focus of intensive research and development. Organic electronics are not likely to surpass soon the Si-based microcircuits in terms of density of element integration and switching speed, but they have other potential advantages over traditional silicon-based junctions.[1-4] Organic materials have vast potential for integration in low-cost microelectronic devices. Circuits and displays based on organic electronics may also be flexible, low-weight and environment-friendly. Last, but not least, some water-tolerant organic devices may be biocompatible, i.e., they may be used in circuits that directly reside on or are implanted inside animal and human tissue and could perform various sensing, interfacing and controlling functions for drug delivery, prosthetics and neural-electronic integration.

Large research effort and significant progress have been achieved in the area of electronics based on conductive polymers. Since their discovery,[5-7] conductive polymers have been used extensively to create organic p-n junctions in solid state devices analogous to silicon-based electronic p-n junctions.[8-16] Conductive polymer junctions are formed in transient[9,10] or fixed state using frozen-junction,[11,12] electrochemical disproportionation and trapping methods[14] or radical induced polymerization of ion-pair monomers as counterions.[15] The conductive polymers can be doped by using, e.g., ion implantation.[17] The unidirectional current response of these polymeric junctions can be based on redox reactions occurring either across a membrane[18] or at the interface with the electrodes.[19,20]

As an alternative to electronic current carriers, a few papers report the fabrication and properties of organic rectifying junctions where the current is carried by ions. For example, Bernards *et al.* have used two organic semiconductors with mobile anions and cations, to create an interface across which the ionic current flows unidirectionally.[21] The ions that carry the current can result from electrolyte dissociation in water.[22] The ionic conductance between chambers containing electrolytes in water can be controlled by "bipolar membranes" with cationic and anionic sides allowing directional ionic transport of the electrolyte solution in which they are immersed.[23,24] Alternatively, in the so-called "electrolyte diode",[25-27] a

uniform hydrogel or ion-permeable membrane separates two reservoirs containing acidic and basic solutions. In the forward voltage the ions cross the membrane moving toward the electrode of opposite sign. In the backward direction, only hydroxide and hydrogen ions enter the membrane where they combine to form water and dramatically decrease the local conductivity. The bipolar membranes and electrolyte diodes, however, are not practical as they include water-filled chambers. In addition, their operation may be dependent on the existence of gradients of electrolyte and/or pH, which may level out over time, at which point these devices will stop rectifying.

We demonstrate here the formation of a fixed rectifying junction between two aqueous gels containing oppositely charged polyelectrolytes. These diode prototypes operate on the (counter) ionic conductance in the gels. The anisotropic distribution of positive and negative mobile counterions within the device leads to nonlinear current conduction across the gel junction. Remarkably, these "soft" diodes operate on the basis of very simple and inexpensive water-borne doped gels and polyelectrolytes. The matrix of the gels is agarose, a gelling agent widely used in biotechnology and food industry. Two typical polyelectrolytes, Sodium Poly(Styrene Sulfonic Acid), PSS, and Poly(Diallyl-dimethylammonium Chloride), PDAC are used to dope the gels.

6.2. Experimental Section

6.2.1. Materials

Poly(Styrene Sulfonic Acid), Sodium Salt (MW 70 kDa) and Poly(Diallyl-dimethylammonium Chloride) (MW 400-500 kDa) were purchased from Polysciences, Inc. and Aldrich, respectively. Agarose (biochemistry research grade) was obtained from Acros Organics. Milli-Q water was obtained from Millipore RiOs 16 reverse osmosis water purification system (Bedford, MA). Platinum foil (99.9 %, 0.025 mm thick) used as electrodes was purchased from Alfa Aesar. Gold electrodes were prepared on pre-cleaned glass microscope slides by depositing 10 nm of chromium followed by 100 nm of gold in a metal evaporator (Model FPS2-41, Cooke Vacuum Products, CT).

6.2.2. Preparation and Characterization of Gel Diodes

PSS solutions (3.5 wt%, 7.0 wt%, 14.0 wt%) and PDAC solutions (2.5 wt%, 5.0 wt%, 10.0 wt%) were prepared separately with Milli-Q water under continuous stirring. Agarose (2.0 wt%) was added to two oppositely charged polyelectrolyte solutions and the mixtures were boiled on a hot plate under continuous stirring. For gelation of the solutions, the mixtures were cooled down to room temperature under gentle stirring to avoid bubble formation.

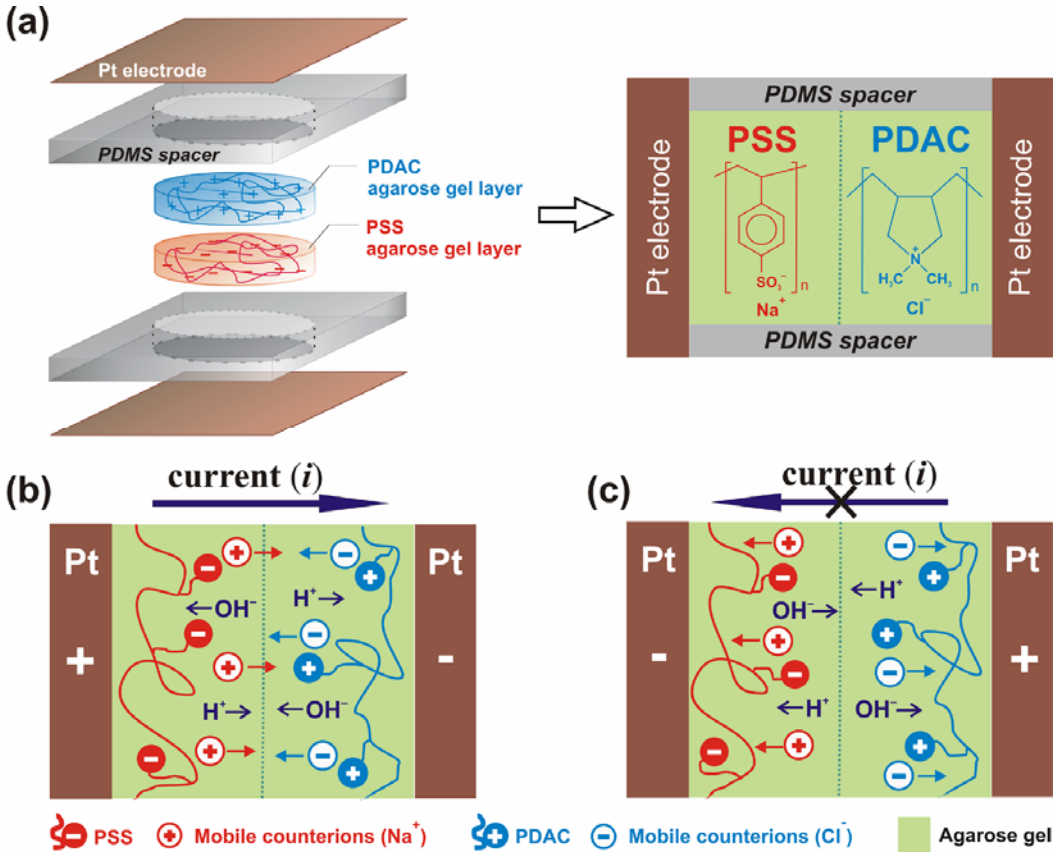

Figure 6.1. (a) Schematic of the gel diode device. Two slabs of aqueous agarose gels containing oppositely charged polyelectrolytes and corresponding counterions are sandwiched between platinum electrodes and sealed by PDMS spacers. (b) Schematic of the ion migration in the gel diode at forward bias and (c) at backward bias.

Cylindrical slabs of 5 mm diameter were cut from the agarose gels containing the polyelectrolytes and desalinated for varying periods of time in large vessels with Milli-Q water. Poly(dimethylsiloxane) (PDMS) spacers were prepared from Sylgard 184 (Dow

Corning) with 0.5, 0.9, 1.0 and 1.25 mm thickness and punched to make a 5 mm diameter hole. The PDMS spacers were placed on platinum or gold electrodes and cylindrical slabs of the gels were inserted into the hole of PDMS spacers. Both agarose gels confined on the metal electrodes (first gel containing PSS and second gel containing PDAC) were then brought in contact with each other, creating the gel interface, and clamped (Fig. 6.1).

The current-voltage characteristics of the device were measured with various sweep scan rates (50 mV/sec, 100 mV/sec, 250 mV/sec, 500 mV/sec) by using a computer-controlled sourcemeter (Keithley 2602, Keithley Instruments, Inc., OH) and probe station (Janis Research Co. Inc., MA) at room temperature. The temporal current responses of the gel diode under continuous application of constant voltage were measured by using a DC regulated power supply (Extech instruments, MA) and a digital multimeter (34405A, Agilent Technologies, CA). The transient response measurements were performed by using a function generator (33120A, Agilent Technologies, CA), computer-controlled digital oscilloscope (DSO3202A, Agilent Technologies, CA) and digital multimeter.

6.3. Results and Discussion

The diodes were formed by bringing in contact two gels containing high molecular weight polyelectrolytes of opposite charges (Fig. 6.1a). Initially, the gelled aqueous phases were desalinated in Milli-Q water to remove the excess (background) electrolyte ions in the system. The high molecular weight polyelectrolytes are trapped in the gel matrices of the device and can not migrate. Thus, the polyelectrolyte counterions as well as the hydroxide and hydrogen ions from dissociation of bulk water are the only charged species that can transport the current across the junction when an electric field is applied. In the forward direction (positive electrode in contact with PSS gel layer, negative electrode in contact with PDAC gel layer), the polyelectrolyte counterions move towards the opposite electrodes crossing the interface, thus conducting current (Fig. 6.1b). On the other hand, in the backward direction the counterions are attracted to the nearest electrode and do not cross the interface between the two gel layers, creating a depletion region around the junction (Fig.

6.1c). Only minor amounts of hydrogen and hydroxide ions present in the system migrate towards the gel interface and associate to form water near the junction.

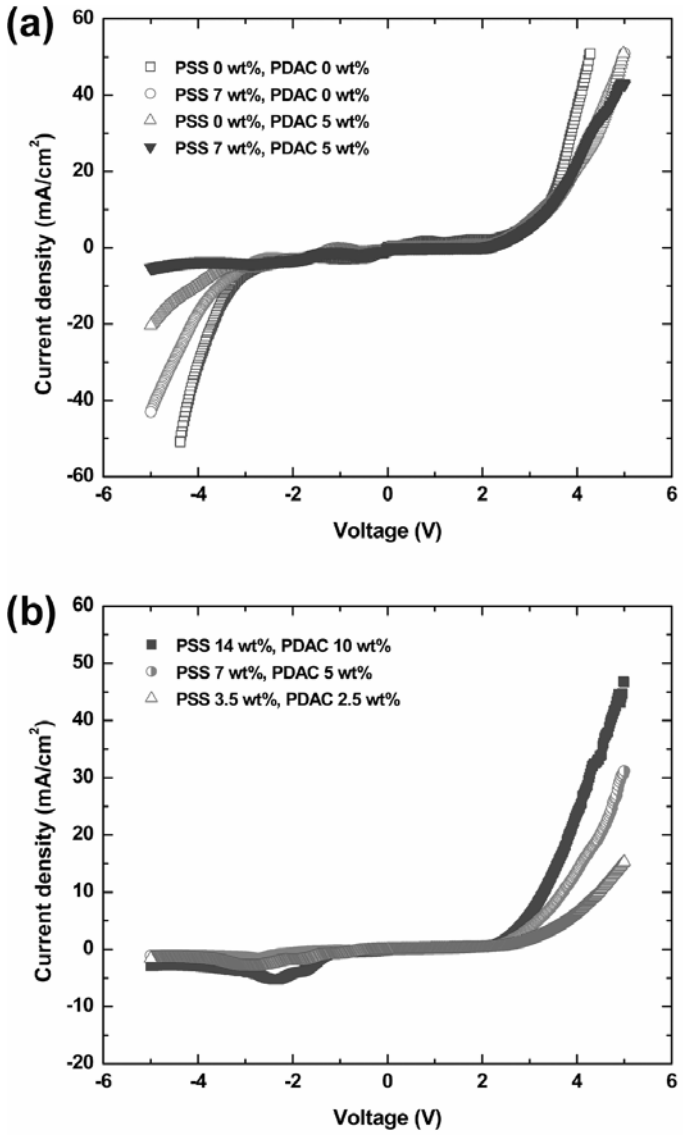

Figure 6.2. (a) Current density as a function of applied bias for junctions prepared from different gel combinations. Each gel layer was 1 mm thick and was desalinated for 2 hrs in DI water except for the pure agarose gel layer, which was used without desalination. The I-V curves demonstrate that only junctions prepared from two oppositely charged polyelectrolyte gels show significant current rectification. (b) Current density as a function of applied bias for junctions prepared from agarose gel layers containing different amounts of polyelectrolytes. Each gel layer was 1 mm thick. All gels were desalinated for 90 min in DI water. Sweep scan rate was 100 mV/sec.

We confirmed that the asymmetric interface between two oppositely charged gel polyelectrolytes was essential in forming a current rectifying junction by comparing the current response from our device to ones from two non-doped agarose gels or combinations of one charged gel containing polyelectrolyte and one pure non-doped gel. The current-voltage curve for two pure agarose gels was symmetric about zero bias and the rectification ratio (the ratio of current at +5 V to current at -5 V) was near unity (Fig. 6.2a). Additionally, no rectification was observed when only one of the gels contained either of the polyelectrolytes. The I-V curve of a device interfacing a gel layer containing PSS (7.0 wt%) with a pure agarose gel was symmetric about zero bias and the rectification ratio was unity. We recorded a slight rectification effect with the gel combination involving a pure agarose gel and another one containing PDAC (5.0 wt%), however, this is possibly due to the fact that the pure agarose gel is slightly anionic[28] and forms an asymmetric interface with the positively charged PDAC (Fig. 6.2a). Junctions prepared with oppositely charged polyelectrolyte in the two gels forming the interface, however, showed pronounced current rectification. As the concentrations of polyelectrolyte dopants within the gel phases were increased, the rectification of the device was enhanced as a result of a higher counterion concentration being available for conducting the current across the gel interface (Fig. 6.2b).

6.3.1. Effect of Gel Desalination

We monitored the current response from several devices prepared from gels desalinated for various times in order to study the role of counterionic current transport. The desalination procedures result in junctions containing decreasing amounts of background electrolyte. Indeed, as the desalinating time of the gels increased, the overall conductivity of the device decreased (Fig. 6.3a). However, the current rectification ratio was enhanced as the current in the backward direction was dramatically reduced compared to that in the forward direction (Fig. 6.3b). Clearly, the removal of extra background ions significantly improves the rectification of the devices, which demonstrates that the rectification effect is dependent on the oppositely charged counterions near the polyelectrolytes in the two gel layers and is suppressed by the presence of arbitrary electrolyte ions. Additionally, in unwashed gels

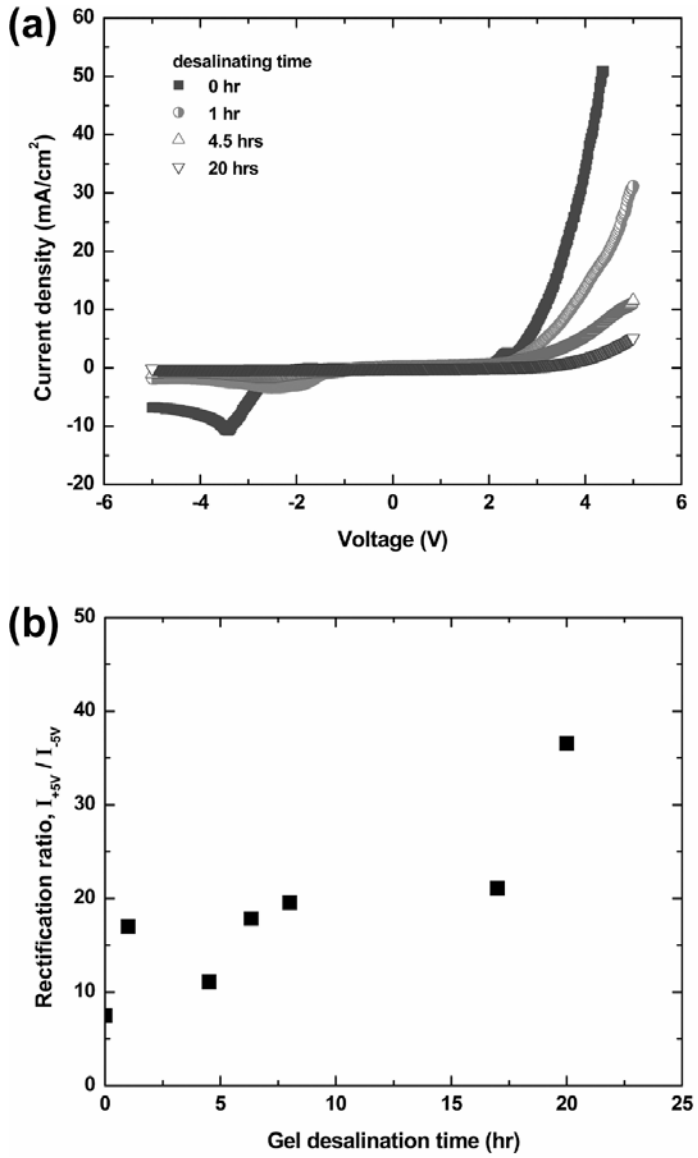

Figure 6.3. (a) Current density as a function of applied bias for a gel diode junction after different desalinating times. The two gel layers contained 7.0 wt% PSS and 5.0 wt% PDAC in 2.0 wt% agarose gel, respectively, and were 1 mm thick. Sweep scan rate was 100 mV/sec. (b) Current rectification ratio at +/-5 V under forward and backward biases as a function of the gel desalinating time. Although the overall conductivity of the gel diode decreases with increasing gel desalinating times, the current rectification ratio is significantly improved.

electrochemical reactions of the contaminant salts at the electrodes also led to a peak in backward current density (Fig. 6.3a). This characteristic peak was progressively removed after desalinating of the gel phases. Different electrode materials were tested in order to

minimize this effect and platinum was found to be the less reactive electrode material in this particular system. Importantly, varying the electrode metal type did not influence the capability of the devices for current rectification. Hence we believe that the rectification effect is primarily a result of the counterionic current and interactions in the gel system rather than electrochemical reactions occurring at the electrode-gel interface.

We measured current rectification ratios between forward and backward directions as large as ~ 40 and current densities up to 50 mA/cm^2 (potentially even higher densities could be achieved, however instrumental limitations prevented us to measure higher currents as apparent in Figure 6.3a). Our gel diodes showed higher current densities than those usually reached by ionic junctions (typically in the range of 0.1 to 10 mA/cm[24,27]), although this parameter has been measured at different voltages by different researchers. Thus, the gel diodes presented in this report can help bring the characteristics of organic diodes based on ionic current carriers closer to ones of devices built from conductive polymers. Indeed, the highest current density value of the gel diodes was comparable to some of the diode junctions made from polymeric films.[8,10,12,14,16]

6.3.2. Effect of Gel Thickness

Gel diodes of different thicknesses were fabricated to evaluate the effect of distance between the electrodes (spanned by the ionic current carriers) on the rectification and conductivity of the devices (Fig. 6.4). As expected, the conductivity of the diodes in the forward direction increased when the total device thickness decreased. This can be attributed to a smaller distance of migration towards the opposite electrode for the counterionic current carriers and a reduced resistance in thinner gel slabs. However, the conductivity in the backward direction was independent of the gel thickness. This result agrees with the development of a depletion region around the gel junction where conductivity drops to very low values due to migration of the counterions away from the interface towards the electrodes and the formation of water as hydrogen and hydroxide ions associate when meeting in the vicinity of the junction.

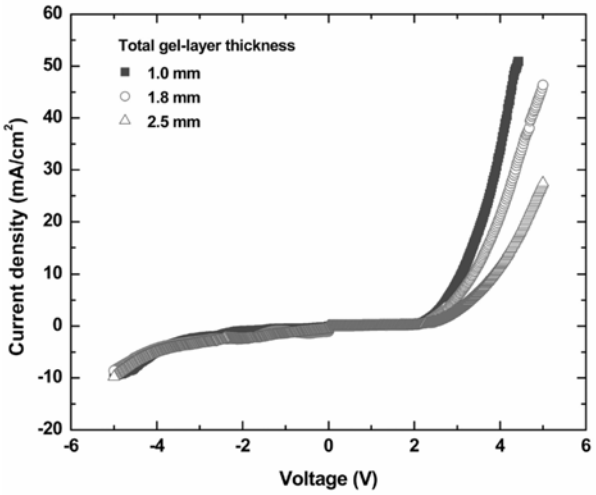

Figure 6.4. Current density as a function of applied bias for gel diodes of different thickness. The two gel layers contained 14.0 wt% PSS and 10.0 wt% PDAC in 2.0 wt% agarose gel and were desalinated for 2 hrs in DI water. Sweep scan rate was 100 mV/sec. The current increase in forward bias for thinner devices is a consequence of smaller distances of migration for the counterions resulting in higher electric field strength across the gel interface. The depletion region around the gel interface due to the formation of water and motion of the counterions toward the electrodes results in low currents independent on the device thickness for backward bias. Note that in the case of the thinner device the current densities measured reached 50 mA/cm^2 before the final +5V voltage; one can assume that higher current densities can therefore be achieved.

6.3.3. Effect of Sweep Scan Rate

This hypothesis is also supported by the data for the current responses from the same gel diode for various sweep scan rates presented in Figure 6.5. When scanning in forward bias, lower currents were recorded at +5V as the scan rate was increased, which shows that the system has not yet reached steady state, as expected for a junction based on ionic current. The final current densities at -5V (Fig.6.5) and the current responses for backward bias of the more desalinated gel layers were independent on the scan rate. This also points out that a depletion region is forming around the gel interface as the polyelectrolyte counterions do not act as current carriers in this direction. In addition, the current peak in the backward bias due to electrochemical reaction was gradually suppressed as the sweep rate was increased. This is possibly due to a suppressed diffusion of reactive ions towards the electrode surfaces at high

sweep scan rate. Furthermore, the current response of gel diodes showed hysteresis resulting from the low ionic mobility (Fig. 6.6).

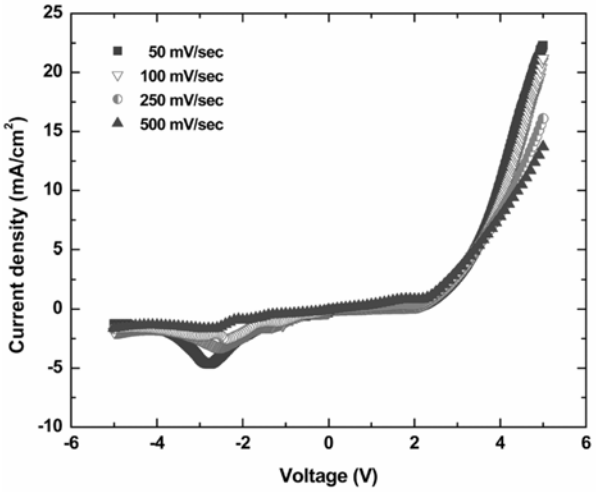

Figure 6.5. Current density measured at different sweep scan rates as a function of applied bias for a diode junction composed of two gel layers containing 7.0 wt% PSS and 5.0 wt% PDAC in 2.0 wt% agarose gel. Each gel layer was 1 mm thick and was desalinated for 2 hrs in DI water.

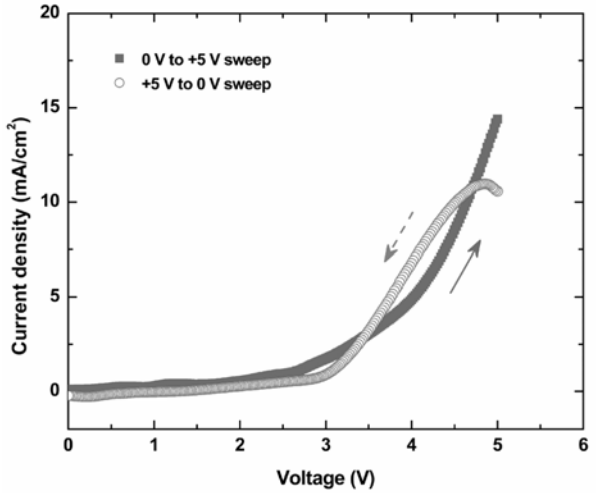

Figure 6.6. Current density as a function of applied bias for a diode junction during a forward scan (0 to +5V) and a backward scan (+5 to 0V) at a sweep scan rate of 100 mV/sec. The two layers contained 7.0 wt% PSS and 5.0 wt% PDAC in 2.0 wt% agarose gel. Each gel layer was 1 mm thick and desalinated for 4 hrs in DI water. The current response of the gel diodes shows some degree of hysteresis probably resulting from the ionic mobility.

6.3.4. Long-Term Current Response at Constant Bias

In all measurements presented above, a part of the current response of the gel diodes is transient, and thus depends on the sweep rate. In order to investigate how long our devices require to reach steady-state, we performed measurements of the long-term current response as a function of time at constant forward (+5V) and backward (-5V) bias. The current

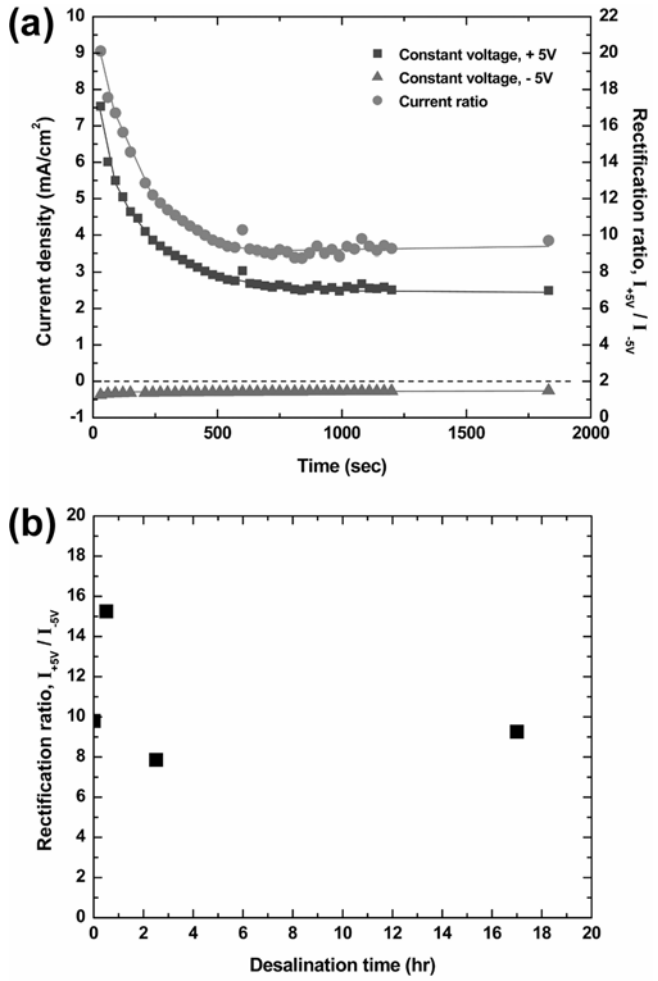

Figure 6.7. (a) Time dependence plot of current density and current rectification ratio from a typical gel diode at constant forward (+5V) and backward (-5V) bias. Under continuous application of constant voltage across the junction, the currents in both directions stabilized rapidly and then remained constant. (b) Current rectification ratio at 30 min after applying constant voltages of +/- 5V with different desalination times. For both plots, the gel diode was constituted of two gel layers containing 7.0 wt% PSS and 5.0 wt% PDAC in 2.0 wt% agarose gel. Each gel layer was 1 mm thick and desalinated for 17 hrs.

response was found to decrease rapidly in the first 500 s for both biases and then stabilize at a nearly constant value in less than one hour. Once constant current values were reached in both directions, the current ratio for a bias of +/-5V stabilized at a value around 10, hence conserving the rectification effect of the gel diode (Fig. 6.7). These experimental data demonstrate that the gel diodes can operate in DC mode for long periods and that the rectification effect is not gradient-driven and largely results from a stationary effect directly due to the charge anisotropy within the system. We also proved that the devices have long term-stability by monitoring their current response for several days with DC sweep scanning (Fig. 6.8). The current density and current rectification ratio at +/- 5 V between forward and backward direction were found to be stable for more than a week as long as the gels were prevented from drying.

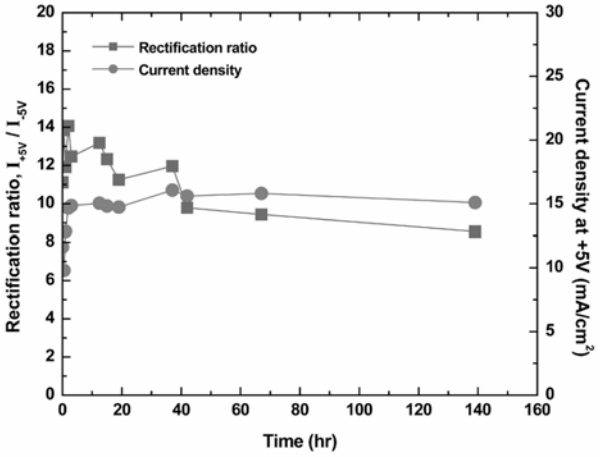

Figure 6.8. Time dependence of current rectification ratio and current density for a typical diode composed of two layers containing 7.0 wt% PSS and 5.0 wt% PDAC in 2.0 wt% agarose gel. Each gel layer was 1 mm thick and was desalinated for 5 hrs in DI water. The currents through the system were measured with DC sweep scanning. The diodes showed stable current response and stable rectification ratio for more than a week.

6.3.5. Current Response under Alternating Electric Field

The transient and steady-state current responses of the gel diodes were also investigated with an alternating electric field applied across the gel interface. The corresponding current response of the gel diodes was recorded in real time. The gel diode displayed good

rectification of the input AC voltage for frequencies under 1 Hz (Fig. 6.9). For each voltage cycle, the data curves display a small stationary current during the periods of voltage in backward bias and a large decreasing current in forward bias. The pronounced relaxation after change from backward to forward bias possibly is a result of a transient, diffusion controlled, response to the suddenly switched voltage. Nevertheless, even after the current response leveled off in the forward bias of one cycle, the devices exhibited a strong rectification effect. In the same manner as the effect recorded for a DC sweep, the rectification ratio rapidly decreased from an initial high value to a stationary one which was then found to be stable for many cycles (at least 30). The dynamic long-term performance of the gel diodes will require additional studies but the data presented here appear very encouraging for potential application of such devices in electronic circuits.

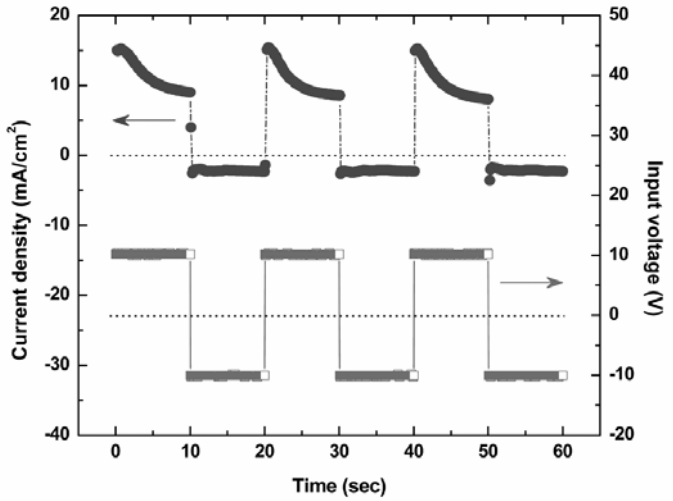

Figure 6.9. Current response of a gel diode under AC field of 50 mHz. The oscillogram of the voltage applied is plotted on the bottom. Two gel layers contained 7.0 wt% PSS and 5.0 wt% PDAC in 2.0 wt% agarose gel. Each gel layer is 1 mm thick and desalinated for 19 hrs in DI water.

The exact physical mechanisms of operation of the gel diodes are still not characterized in detail in terms of ionic transport and reactions at the junction and at the electrodes. It is likely that electrolysis of water without visible release of gas is involved in the steady state current transfer at the electrodes. It is important, however, that we have

proved that the asymmetric conductance does not seem to arise from gradients in the ionic concentration. Even though this is the mode of operation of the previously reported electrolyte diodes,[25,27] it can be argued that a true rectifying junction would not become depleted upon continuous application of constant voltage across the junction under both forward and backward bias. The existence of a large stationary part of the current and the long-term stability point out that this may be the case with the gel devices reported here.

6.4. Conclusions

We demonstrated that current-rectifying diode junctions can be fabricated by interfacing aqueous gels doped with oppositely charged polyelectrolytes. The remarkable feature of these rectifying junctions is that they operate on the basis of water-borne ions. These devices combine the ionic current rectification of electrolyte diodes and the stability and ease of fabrication of polymer electronics. Electronic components based on organic materials are of interest because they possess a number of potential advantages over traditional silicone-based junctions. Even though our devices were first-generation prototypes without any optimization, the gel diodes had comparable or higher current density and rectification ratios than other organic-based electronic counterparts. The process of their preparation is simple, environment-friendly and scalable. These devices are potentially good candidates for facile integration in biomimetic electronic devices and circuits. The gel and other components that constitute them are flexible and inexpensive. As the gel diodes are based on aqueous media, they could be used in bioelectronic devices. These principles could be extended to gel transistors and other equivalent electronic elements.

6.5. Acknowledgements

This research was performed with Dr. Olivier Cayre as a Postdoctoral member in our group. We are grateful to Jeong-Seok Na and Prof. Gregory Parsons for access to the probe station for I-V measurements and Prof. Peter Fedkiw for stimulating discussions regarding this study. This work was supported by NSF-NIRT and Camille Dreyfus Teacher-Scholar grants.

6.6. References

[1] Voss, D., Cheap and cheerful circuits. *Nature* (2000) *407*, 442-444.

[2] Forrest, S., Burrows, P. and Thompson, M., The dawn of organic electronics. *IEEE Spectrum* (2000) *37*, 29-34.

[3] Shaw, J. M. and Seidler, P. F., Organic electronics. Introduction. *IBM J. Res. Dev.* (2001) *45*, 3-9.

[4] Kelley, T. W., Baude, P. F., Gerlach, C., Ender, D. E., Muyres, D., Haase, M. A., Vogel, D. E. and Theiss, S. D., Recent progress in organic electronics: Materials, devices, and processes. *Chem. Mater.* (2004) *16*, 4413-4422.

[5] McNeill, R., Weiss, D. E., Wardlaw J. H. and Siudak, R., Electronic conduction in polymers. I. Chemical structure of polypyrrole. *Aust. J. Chem.* (1963) *16*, 1056-1075.

[6] McGuiness, J., Corry, P. and Proctor P., Amorphous semiconductor switching in melanins. *Science* (1974) *183*, 853-855.

[7] Shirakawa, H., Louis, E. J., MacDiarmid, A. G., Chiang, C. K. and Heeger A. J., Synthesis of electrically conducting organic polymers: halogen derivatives of polyacetylene, $(CH)_x$. *J. Chem. Soc., Chem. Commun.* (1977) *16*, 578-580.

[8] Burroughes, J. H., Jones, C. A. and Friend, R. H., New semiconductor device physics in polymer diodes and transistors. *Nature* (1988) *335*, 137-141.

[9] Pei, Q., Yu, G., Zhang, C., Yang, Y. and Heeger, A. J., Polymer light-emitting electrochemical cells. *Science* (1995) *269*, 1086-1088.

[10] Pei, Q., Yang, Y., Yu, G., Zhang, C. and Heeger, A. J., Polymer light-emitting electrochemical cells: In situ formation of a light-emitting p-n junction. *J. Am. Chem. Soc.* (1996) *118*, 3922-3929.

[11] Yu, G., Cao, Y., Andersson, M., Gao, J. and Heeger, A. J., Polymer light-emitting electrochemical cells with frozen p-i-n junction at room temperature. *Adv. Mater.* (1998) *10*, 385-388.

[12] Yang, C., Sun, Q., Qiao, J. and Li, Y., Ionic liquid doped polymer light-emitting electrochemical cells. *J. Phys. Chem. B* (2003) *107*, 12981-12988.

[13] Chen, M., Nilsson, D., Kugler, T., Berggren, M. and Remonen, T., Electric current rectification by an all-organic electrochemical device. *Appl. Phys. Lett.* (2002) *81*,

2011-2013.

[14] Cheng, C. H. W. and Lonergan M. C., A conjugated polymer pn junction. *J. Am. Chem. Soc.* (2004) *126*, 10536-10537.

[15] Leger, J. M., Rodovsky, D. B. and Bartholomew, G. P., Self-assembled, chemically fixed homojunctions in semiconducting polymers. *Adv. Mater.* (2006) *18*, 3130-3134.

[16] Shao, Y., Bazan, G. C. and Heeger, A. J., Long-lifetime polymer light-emitting electrochemical cells. *Adv. Mater.* (2007) *19*, 365-370.

[17] Wada, T., Takeno, A., Iwaki, M., Sasabe, H. and Kobayashi, Y., Fabrication of a stable p–n junction in a polyacetylene film by ion implantation. *J. Chem. Soc., Chem. Commun.* (1985) *17*, 1194-1195.

[18] Buck, R. P., Surridge, N. A. and Murray, R. W., Liquid/solid polyelectrolyte diodes and semiconductor analogs. *J, Electrochem. Soc.* (1992) *139*, 136-144.

[19] Pickup, P. G., Kunter, W., Leidner, C. R. and Murray, R. W., Redox conduction in single and bilayer films of redox polymer. *J. Am. Chem. Soc.* (1984) *106*, 1991-1998.

[20] Leventis, N., Schloh, M. O., Natan, M. J., Hickman, J. J. and Wrighton, M. S., Characterization of a "solid-state" microelectrochemical diode employing a poly(vinyl alcohol)/phosphoric acid solid-state electrolyte: rectification at Junctions between tungsten trioxide (WO3) and polyaniline. *Chem. Mater.* (1990) *2*, 568-576.

[21] Bernards, D.A., Flores-Torres, S., Abruna, H.D. and Malliaras G.G., Observation of electroluminescence and photovoltaic response in ionic junctions. *Science* (2006) *313*, 1416-1419.

[22] Lovrecek, B., Despic, A. and Bockris, J. O'M., Electrolytic junctions with rectifying properties. *J. Phys. Chem.* (1959) *63*, 750-751.

[23] Bassignana, I. C. and Reiss, H., Ion transport and water dissociation in bipolar ion exchange membranes. *J. Membr. Sci.* (1983) *15*, 27-41.

[24] Ramírez, P., Rapp, H. J., Reichle, S., Strathmann, H. and Mafé, S., Current-voltage curves of bipolar membranes. *J. Appl. Phys.* (1992) *72*, 259-264.

[25] Hegedus, L., Kirschner, N., Wittmann, M., Simon, P., Noszticzius, Z., Amemiya, T., Ohmori, T. and Yamaguchi, T., Nonlinear effects of electrolyte diodes and transistors in a polymer gel medium. *Chaos* (1999) *9*, 283-297.

[26] Lindner, J., Snita, D. and Marek, M., Modelling of ionic systems with a narrow acid-base boundary, *Phys. Chem. Chem. Phys.* (2002) *4*, 1348-1354.

[27] Ivan, K., Wittmann, M., Simon, P. L., Noszticzius, Z. and Vollmer J., Electrolyte diodes and hydrogels: Determination of concentration and pK value of fixed acidic groups in a weakly charged hydrogel. *Phys. Rev. E* (2004) *70*, 061402.

[28] Guo. Y., Li, X. and Fang, Y., The effects of electroendosmosis in agarose electrophoresis. *Electrophoresis* (1998) *19*, 1311-1313.

Chapter 7

Summary

7.1 Summary

The main theme of my dissertation is the development of new lab-on-a-chip systems and innovative applications of microfluidic phenomena. Microfluidic techniques were used not only for manipulating materials within the confined microfluids but also rendering a certain function to the matrix materials with embedded microchannel structures.

In the first project, we characterized unique phenomena of colloidal particle transport and separation inside single microdroplets of water floating on the surface of dense fluorinated oil. The experiments were performed on droplet-based microfluidic chips, where single droplets were captured and transported by alternating electric fields applied to arrays of electrodes below the oil. The particles suspended in the droplets were collected in their top region during the evaporation process. Experimental results and numerical simulations showed that this microseparation occurred as a result of a series of processes driven by mass and heat transfer. These remarkable phenomena could be used for on-chip "droplet engineering" processes, where the microdroplets are served as sites for microreactors, the assembly of complex asymmetric supraparticles, and novel microfluidic systems for microbioassays.

The second project that was carried out demonstrated how an additional level of complexity can be engineered to turn various types of miniature semiconductor diodes into prototypes of self-propelling micromachines, micropumps and micromixers. The diodes suspended in water propelled themselves electroosmotically when a uniform alternating electric field was applied across the container. These "smart particles" suggest rudimentary solutions to problems facing self-propelling microdevices, including harvesting power from external sources, internally controlled movement, and potential for a range of additional functions. The autonomously moving microdiodes can emit light or respond to light and could be controlled by internal logic. Diodes immobilized on the walls of microfluidic channels provided new principles of microfluidic pumping and mixing driven by electroosmotic flows developed in the vicinity of the diode surfaces. The flow velocity of liquid pumped by the diodes facing the same direction linearly increased with the magnitude of the applied voltage, but did not depend on the frequency of the field. This could eliminate

intrinsic problem with fluid flows in areas of non-uniform field that occur in conventional AC electrohydrodynamics pumps. The transverse flow driven by localized electroosmotic flux between diodes oriented oppositely on the microchannel was used in microfluidic mixers. Theoretical analysis and numerical calculations of the microfluidic pumping and mixing by the diodes were in excellent agreement with the experimental data. The combined application of AC and DC fields in such devices allowed decoupling of the velocity of the particles and liquid and could be used for precise on-chip separations. These techniques could be used in novel dynamically reconfigurable microfluidic-electronic chips.

In the next stage, we demonstrated a new class of materials with programmable shapes. The novelty feature of this material was that microfluidic channel network was used for improving the mechanical properties of the large area polymer materials. Polydimethylsiloxane (PDMS) sheets with embedded microchannel network containing photocurable polymers were shaped on demand and exposed by UV light. The solidified photoresist inside the microchannel significantly enhanced mechanical properties, such as elastic modulus, of the microfluidic composite materials. The introduction of SU-8 photopolymer into the microchannels allowed retaining and recovering the user-defined shapes without losing the softness and flexibility of the PDMS layer. The materials and the process of preparation of these microfluidic materials are simple, inexpensive and scalable. The technique can be used in advanced elastomeric materials and smart packaging for protecting delicate contents and easy scratchable surfaces.

Complementary to the case where we used semiconductor elements act as functional colloidal particles, colloidal materials also could be used for fabricating nonlinear electronic components. Our research showed that a fixed junction between two aqueous gels containing oppositely charged polyelectrolytes could rectify electric current. The agarose-based gels were doped with sodium poly(styrene sulfonic acid) and poly(diallyl dimethylammonium chloride). Anisotropy in the mobile counterionic charges in the gels led to the unidirectional current response across the gel junction. The current from the gel diodes depended on the concentration of polyelectrolyte, the background ionic concentration, and the distance traveled by the ions. The current-voltage curves from the devices demonstrated a

combination of transient and stationary rectification effects. The current densities achieved were comparable to or higher than those obtained with previously reported organic semiconductor diodes. The materials and processes of preparation of these devices are inexpensive and scalable. This simple technique can be extended to fabricate polyelectrolyte bipolar junction transistors, *e.g.* by placing one type of charged gel between agarose gels containing oppositely charged polyelectrolyte. Such soft devices based on aqueous gel phases could be used in numerous applications requiring flexible and biocompatible electronic components.